1-2007

Study of structure development during Melt Spinning of isotactic Polypropylene fibers using Raman Spectroscopy and Wide Angle X-ray Diffraction Simultaneously

Dushyanth Pandana
Clemson University, dpandan@clemson.edu

STUDY OF STRUCTURE DEVELOPMENT DURING MELT SPINNING OF ISOTACTIC POLYPROPYLENE FIBERS USING RAMAN SPECTROSCOPY AND WIDE ANGLE X-RAY DIFFRACTION SIMULTANEOUSLY

A Thesis
Presented to
the Graduate School of
Clemson University

In Partial Fulfillment
of the Requirements for the Degree
Master of Science
Materials Science and Engineering

---

by
Dushyanth V. Pandana
May 2007

Accepted by:
Dr. Gary C. Lickfield, Committee Chair
Dr. Lawrence W. Grimes
Dr. Philip J. Brown

ABSTRACT

Isotactic polypropylene (iPP) is a commercially important semicrystalline polymer. It is widely used in the manufacturing of fibers, with a variety of applications. Specific end-use applications require specific properties, which are dependent on the polymer morphology produced during processing. Therefore, final properties of a material are dependent on the processing parameters.

iPP fibers are produced mainly by melt spinning, and the important processing parameters in the melt spinning process include the extrusion temperatures, the throughput and shear rates, rate of cooling, and the feed and draw roll take-up velocities. Studying the structure development of iPP fibers during their formation gives valuable information on fiber microstructure or morphology, i.e., the degree of crystallinity and molecular orientation of the crystalline material. An understanding of how the morphology develops along the spinline, and the effect of processing parameters on the morphology is crucial in optimizing the melt spinning process.

The objective of this work was to study the development of structure in the fiber as the polymer was transformed from a molten amorphous state to a semi-crystalline material, and to investigate the effects of throughput rate and take-up velocity on the structure development along the spinline. Raman Spectroscopy and Wide Angle X-ray Diffraction (WAXD) were used simultaneously to characterize the morphology of iPP along the spinline during melt spinning. DSC and birefringence measurements were also collected for the as-spun fibers.

Two throughput rates (0.67 and 0.89 g/min/hole) and two take-up velocities (400 & 800 m/min) were used. The polymer processing temperature was 220 ^{0}C and the extruder pressure was set to 500 psi. Raman (polarized and unpolarized) and WAXD data were simultaneously collected at six different positions along the spinline (60, 50, 40, 35, 30 and 25 cm from the spinneret).

DEDICATION

To my beloved parents and my brother

ACKNOWLEDGEMENTS

The author would like to express gratitude to those people who helped him during the course of the research.

Dr. Gary Lickfield, the committee chairman, for all his assistance, patient guidance and encouragement in every aspect of the research.

Other members of the committee, Dr. Philip Brown and Dr. Larry Grimes, for their cooperative efforts, valuable suggestions, and time.

Dr. Kate Stevens, Dr. Paulo Lopes, Dr. Amod Ogale, Kim Ivey, and Robbie Nicholson for their assistance in data collection and analysis.

My family and friends for their inspiration and encouragement.

Srinivasa Varkol, Sandeep Sant, Kristen Calabrese, Adrian Trif, Giri Gururajan, Dr. Amit Naskar, and Dr. Haifeng Shan for technical assistance.

Center for Advanced Engineering Fibers and Films (CAEFF), School of Material Science and Engineering, and National Science Foundation (NSF) for the financial support of the research effort.

TABLE OF CONTENTS

Table of Contents (Continued)

Page

LIST OF TABLES

List of Tables (Continued)

LIST OF FIGURES

List of Figures (Continued)

List of Figures (Continued)

Figure Page

List of Figures (Continued)

Figure Page

List of Figures (Continued)

Figure Page

List of Figures (Continued)

Figure Page

CHAPTER 1

INTRODUCTION

Although synthetic fibers have existed only since the 1930s, they make up the majority of fibers used today [1]. One of the most widely used of these fibers is isotactic polypropylene (iPP) fibers. iPP fibers exhibit a wide range of properties, making them suitable for a variety of applications. These properties, which are dependent on the structure of the polymer and processing parameters, can be tailored for specific end use applications by controlling the manufacturing conditions. Therefore, studying the structure development of iPP fibers during their formation provides valuable information on the effect of various processing conditions on fiber microstructure or morphology.

One of the commonly used methods for producing iPP fibers is melt spinning, an important manufacturing process since its commercialization for production of nylon 66 fibers in 1940 [2]. iPP is especially suitable for melt spinning because of its good spinnability, which is the capability of a material of being spun. However, the development of structure during melt spinning of iPP is complicated because of the influences of both the rheological factors (stretching of the melt) and the non-isothermal effects resulting from the heat transfer from the running filament to the surrounding environment. An understanding of how the structure develops along the spinline and the effect of processing conditions on the development of the crystallinity and orientation are crucial in optimizing the melt spinning process. To address this need, the research reported here investigated the morphology of iPP fibers using Raman spectroscopy and

wide angle x-ray diffraction (WAXD) simultaneously during melt spinning. The rest of this chapter reviews the melt spinning process; the conformations and crystal structures in polypropylene (PP); the morphology of polymers; the principle and theory behind Raman spectroscopy, WAXD, differential scanning calorimetry (DSC), and birefringence; and previous research in this field.

1.1 Melt spinning

A typical melt spinning setup consists of an extruder, a positive displacement pump, a spin head, a spinneret or die, a quench tower, a feed roll, draw rolls, and a winder. A schematic of the melt spinning process is shown in Figure 1.1. The function of the extruder is to heat and mix the polymer to produce a homogeneous melt, and also to pump it through the spinneret at a constant rate. The extruder has a motor driven screw of desired length/diameter ratio inside the barrel, which helps in mixing and pumping of the melt. There are typically three zones in an extruder corresponding to the geometry of the screw: the feed zone, the compression zone, and the metering zone. Each of these zones is heated to different temperatures depending upon the polymer being extruded.

The first step in melt spinning is to feed polymer chips through the hopper into the extruder feed zone. Depending on the polymer extruded, the chips may be dried or used without prior drying. A slow nitrogen purge is frequently used to prevent the polymer from oxidization. As the polymer is pushed along the extruder barrel by the screw, it is heated by a combination of conducted heat and mechanical shear heat derived from the mixing and kneading action of the screw. Once the polymer melt exits the

metering zone, the positive displacement pump then delivers the molten polymer at a set flow rate to the spin head.

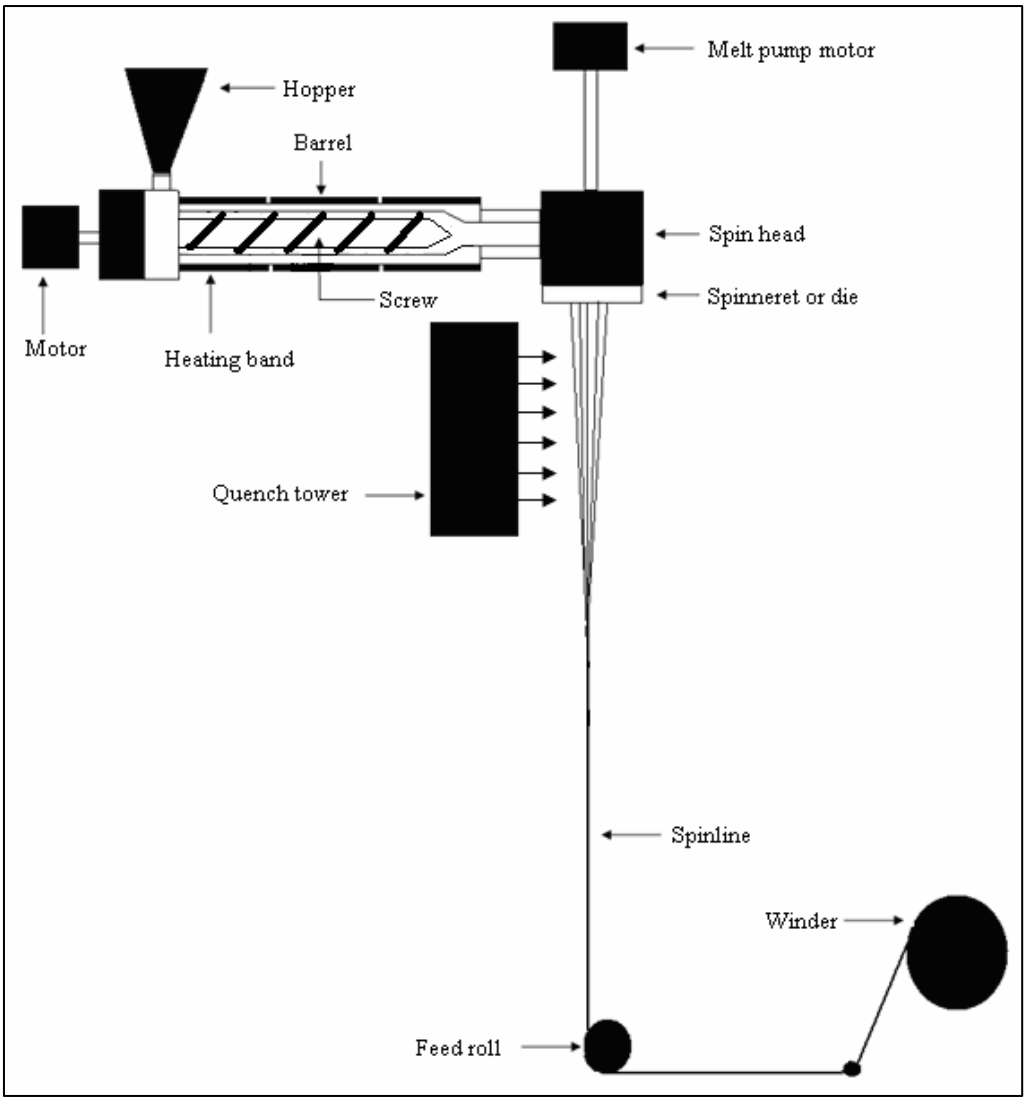

Figure 1.1 Schematic of melt spinning process

The spin head consists of filters and channels that supply molten polymer to the spinneret, through which the molten polymer is extruded. As soon as the polymer melt exits the spinneret, a quench tower or a spin chimney controls the cooling or quenching

of the molten filaments. The cooled or quenched fibers are then pulled down to a smaller cross-sectional area by a feed roll, which is set to a desired velocity. A set of draw rolls is used before or after the spinning process depending on the final property requirements of the fiber. Drawing of fibers orients the molecular chains in the fibers to a high degree in the machine direction. Spun fibers are wound up on a bobbin attached to the winder.

The final properties of the fiber, such as percent crystallinity, molecular orientation, diameter, etc., depend on various processing parameters. The key processing parameters for melt spinning are the temperature at which the polymer is extruded, the cooling conditions along the spinline, mass throughput per spinneret hole, length of the spinline, take-up velocity, and size and the shape of spinneret holes. Of all these parameters, two parameters are typically characterized by researchers, throughput rate and the take-up velocity. The effect of these two parameters on different fiber properties has been the subject of interest in many previous works [21,24,26,46].

1.2 Structure of polypropylene

Understanding the structure of the polymer being processed is important to gain an in-depth knowledge of polymer structure property relationships. Polypropylene (PP) is obtained as a result of polymerization of propylene ($CH_3 - CH = CH_2$) and is one of the widely used thermoplastic polymers among the polyolefins [4]. PP is preferred in various applications because of its low density, high crystallinity, high stiffness and hardness, resulting in a high strength-to-weight ratio end product [3]. The main applications of PP range from carpet industry, domestic textiles, and clothing to industrial textiles.

The factors which control the stereo arrangement in PP are, the degree of branching (linear or branched), regiospecificity (head-to-tail, or head-to-head or tail-to-tail), and stereospecificity (right or left hand) [4]. PP is a typical polymer whose properties are affected by stereoregularity. PP can be produced with different tacticities, such as isotactic, syndiotactic, and atactic. The different tacticities in PP are shown in Figure 1.2.

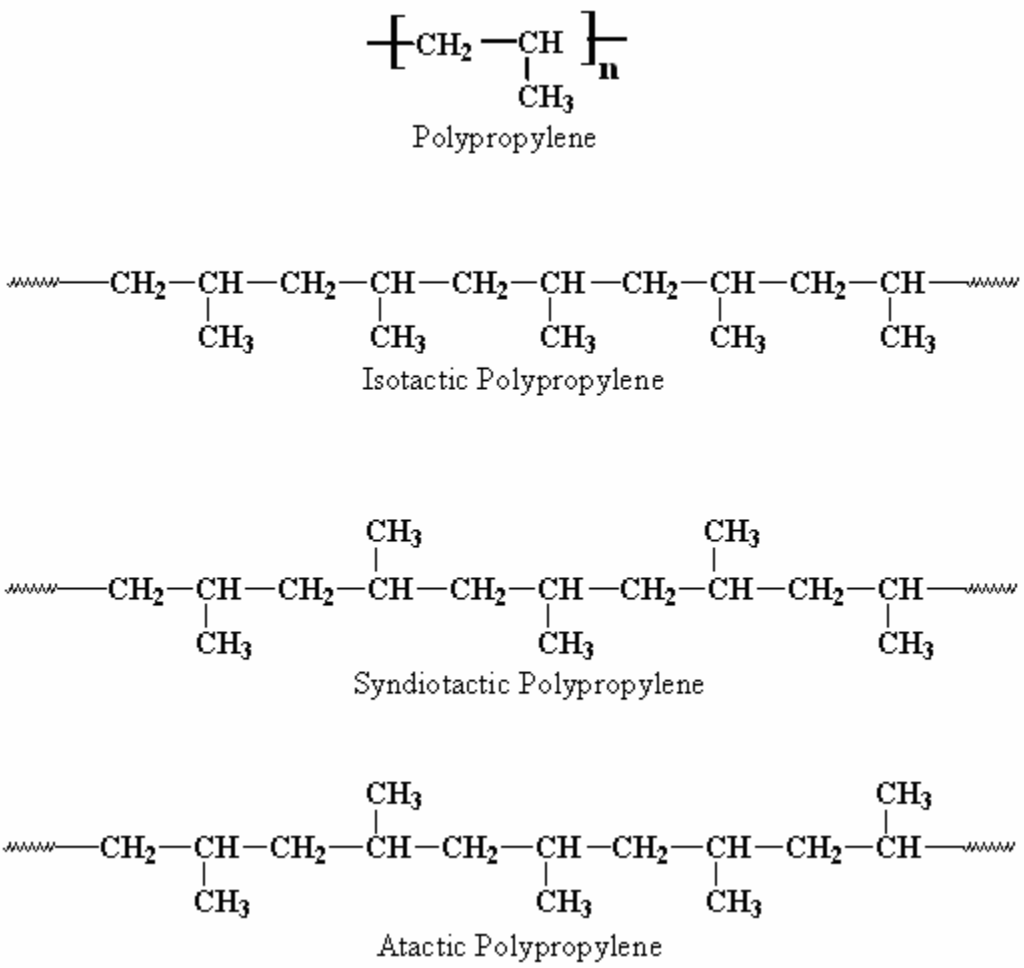

Figure 1.2 Tacticities in polypropylene

In iPP, the pendent methyl groups are present on the same side of the backbone; they are alternating in syndiotactic polypropylene (sPP), and random in atactic polypropylene (aPP). iPP is one of the most widely used forms of PP and is prepared with various modifications of Ziegler-Natta coordination catalysts, producing polymers with various degrees of stereoregular order. The final isotacticity can be up to 98% [5].

In Figure 1.3 [41], an illustration of an extended chain vinyl polymer molecule in a polyethylene (PE) type planar zig-zag is shown, where the atoms numbered 1, 2, 3, etc. are substituted atoms. Due to steric hindrance, the chain adopts a different conformation [41]. iPP does not attain an all 'trans' conformation as in PE, because of steric overlap caused by the substituent methyl (CH_3) groups, as shown in Figure 1.4 [41]. The presence of bulky $-CH_3$ groups increase the chain cross-sectional area and reduce the possibility of highly extended chain conformations. Therefore, for solid iPP, the most energetically favored conformation is trans-gauche (tg), and this is also the main conformational form of iPP in solution [3].

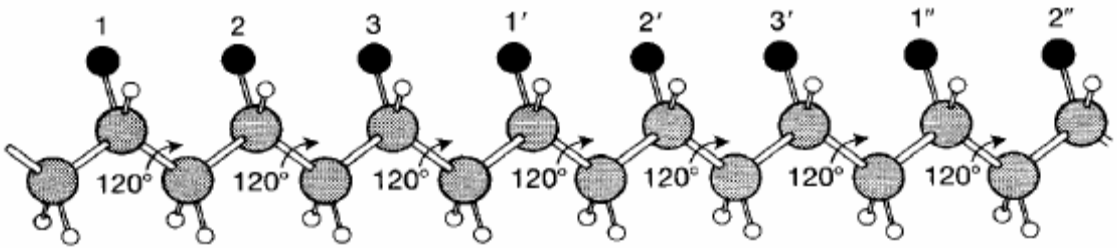

Figure 1.3 Illustration of a vinyl polymer molecule

As a result of 'tg' conformation, in all the crystalline modifications, the molecules twist into a helix to form a 3_1 helix, with pendent methyl groups pointing outwards, and involve three repeats to achieve a full turn on the helix as shown in Figure 1.5 [41]. The

methyl groups $CH_{3,1}$, $CH_{3,1'}$ and $CH_{3,1''}$ lie in a line and similarly $CH_{3,2}$, $CH_{3,2'}$ and $CH_{3,2''}$ and $CH_{3,3}$ and $CH_{3,3'}$. Four possible conformations of helices can be distinguished relative to their reference axis as shown in Figure 1.6 [42], right handed and left handed, where each can be oriented up or down.

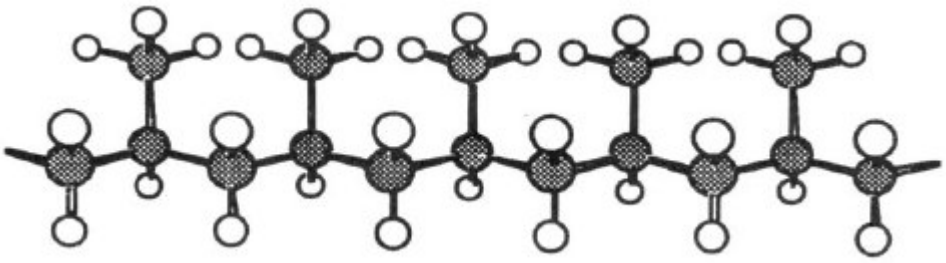

Figure 1.4 Isotactic polypropylene in trans-trans conformation exhibiting steric overlap due to pendant methyl groups

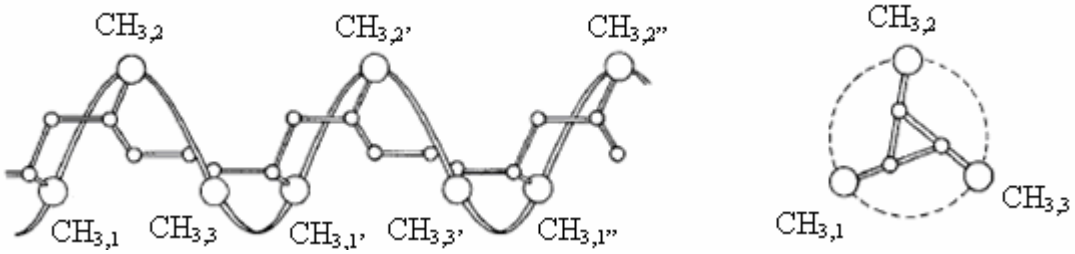

Figure 1.5 'tg' conformation in iPP forming a 3_1 helix

iPP is generally regarded as a semi-crystalline polymer. Wide angle x-ray scattering patterns for iPP show characteristics of both crystalline and amorphous phases. In the crystalline phase individual crystallites are present which are formed from molecular chains folded back on one another and connected to the amorphous phase by tie molecules [3]. iPP is known to exhibit polymorphism, and x-ray diffraction studies

have helped identify four different crystal forms of iPP: viz., α, β, γ, and mesomorphic. All of these crystal forms have the same tg conformational structure, but they differ with respect to mutual chain orientation in the unit cell.

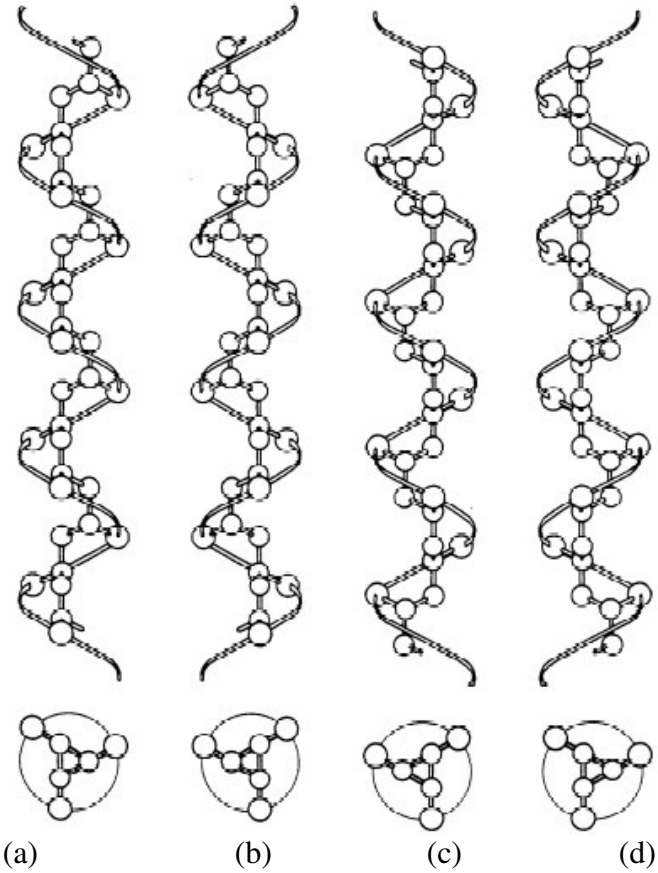

Figure 1.6 3_1 helix conformations in isotactic polypropylene, (a) Left handed down, (b) Right handed down, (c) Left handed up, and (d) Right handed up

The α-form is monoclinic, and is the most common and stable crystal form of iPP. A unit cell of α-form iPP is shown in Figure 1.7. It contains twelve monomer units, and there are four chains passing through the unit cell, each of which has a 3_1 helical conformation [5]. The polymer chain axis or the helix axis is parallel to the c-axis of the

unit cell, and the polymer chains are arranged in alternate layers of right hand (R) and left hand (L) helices along the b-axis of the unit cell as shown in Figure 1.8 [49].

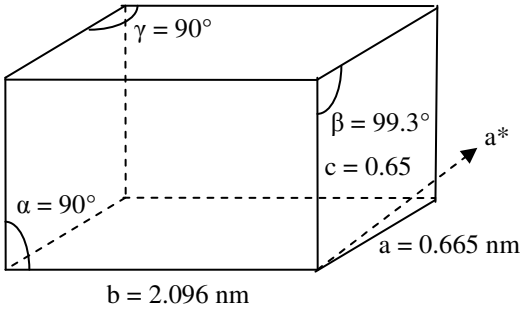

Figure 1.7 Unit cell of α-form isotactic polypropylene crystal

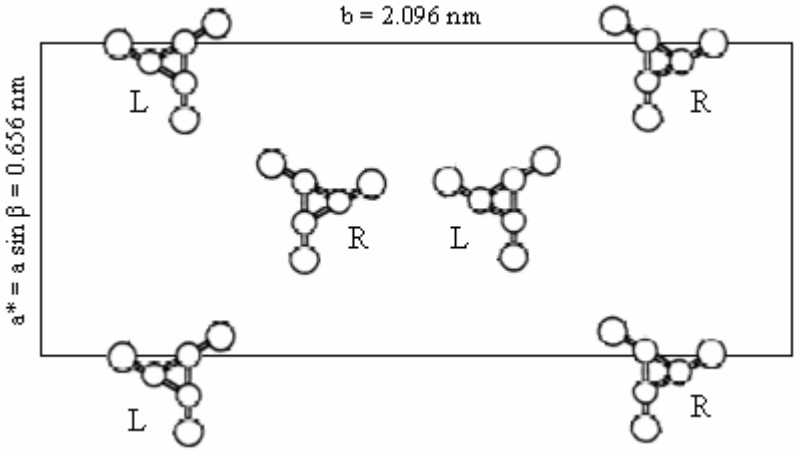

Figure 1.8 Arrangement of helices in a unit cell of α-form isotactic polypropylene crystal

The β-form and γ-forms result only under special conditions, and not often during normal crystallization [43]. The β-form is trigonal and is obtained during crystallization in a temperature gradient from a sheared melt, or in the presence of β nucleating agents such as quinacridone pigment. The γ-form is orthorhombic and is obtained in PP copolymers by slow cooling of low-molecular-weight fractions of polypropylene, or by

crystallization under high pressure [43]. Only recently this phase has been recognized as a crystal phase with a "frustrated" chain packing within the unit cell [42]. A triclinic 'smectic' or mesomorphic form is also observed in iPP, which is known to form when the polymer melt is subjected to quenching by cold water. This form converts to the monoclinic form when heated above 60° C. The parameters of α, β, and γ-forms of iPP are given in Table 1.1 [26].

Table 1.1 Unit cell parameters of isotactic polypropylene crystal forms

Form	α	β	γ
Crystal Structure	Monoclinic	Trigonal	Orthorhombic
a (nm)	0.665	1.101	0.854
b (nm)	2.096	1.101	0.993
c (nm)	0.65	0.65	4.241
α (°)	90	90	90
β (°)	99.3	90	90
γ (°)	90	120	90

1.3 Morphology – Crystallinity and orientation in polymers

The degree of crystallization and orientation are the two most important morphological features of polymers as they influence many of a polymer's properties. Almost all polymeric materials fall into one of the three classes with respect to crystallinity: polymers which cannot crystallize because of lack of a regular chain structure (ex. atactic polystyrene or aPP), polymers which can crystallize but have not, either because of rapid cooling from the melt or because of other factors such as a very slow rate of crystallization (ex. polycarbonate), and polymers which can crystallize and have, which are called as semi-crystalline polymers.

A whole range of order may exist in a semi-crystalline polymer, ranging from a three-dimensionally ordered crystal to two-dimensional periodicity or orientation of chain segments to complete randomness of molecular chains (amorphous) [5]. This complex morphology is the most important factor in determining the strength and modulus of semi-crystalline polymeric materials. The crystalline phase has long chain molecules organized in a three-dimensional periodicity, which may or may not be oriented. The non-crystalline phase can be amorphous (no long range order) or oriented and not crystalline. The crystalline phase is embedded in the amorphous phase, with many chains joining the two phases to provide strength. These joining segments of chains are called "tie chains" [5].

Polymers, unlike small molecules, can have a wide range of crystallinities, from 0% to ~90%. Although liquid-crystalline polymers can have high crystallinity, the crystallinity of other polymers rarely exceeds 60% due to the high molecular weight of polymer chains. The chains are highly entangled and cannot disentangle fast enough during crystallization to fully crystallize before the chains are locked into place by two or more growing crystals. The long chain nature and composition of polymers prevents them from being 100% crystalline [1]. There is always some portion that is non-crystalline, and it has been proved that it is impossible to mechanically separate crystalline phase from the non-crystalline phase.

A polymer can be thought of as a molecular string. If the string is straightened and aligned, it corresponds to a highly oriented chain. If it is randomly coiled, it corresponds to an unoriented amorphous chain. Between these limits are the partially straightened and partially aligned strings which correspond to an anisotropic chain. The

tensile modulus depends on the fraction of chain segments that are oriented and the degree of orientation along the stress direction. If we have several strings, all of which are straight and aligned in the same direction, it will be difficult to increase the distance between their ends. On the other hand, if each string is randomly coiled, it will be easy to stretch the string in a single direction. The tensile modulus depends strongly on the relative extent of orientation of the polymer chain segments and also on the fraction of crystalline region.

Polymers with high crystallinity and high orientation tend to be strong with a high modulus, whereas non-crystalline polymers with low orientation tend to have long elongations to break and a low modulus. As it is well known that the strength, elongation at break and the modulus are such important mechanical properties in polymers, considerable effort goes in developing improved methods for determining the degree of crystallinity and the orientation in polymers.

There are several methods of estimating the degree of crystallinity and molecular orientation in as-spun polymer fibers. The degree of crystallinity can be estimated using WAXD, DSC, density measurements, isotropic index of refraction, infrared spectroscopy (IR), nuclear magnetic resonance (NMR) measurements, and Raman spectroscopy. The average orientation can be measured using techniques, such as birefringence, x-ray scattering, sonic modulus, IR dichroic ratios, and polarized Raman spectroscopy. Each of these methods measures a specific characteristic of a polymer, has advantages and disadvantages, and is based on a model. Few of these methods are applicable for on-line measurements, i.e., characterization during the melt spinning of fibers, with Raman spectroscopy and WAXD being the most useful ones.

1.4 Raman spectroscopy

1.4.1 Introduction

Raman spectroscopy is one of the three principal methods by which the molecular vibrations may be studied. Raman spectroscopy works on the principle of 'Raman scattering' of monochromatic light, usually from a laser in the visible, near infrared (IR), or near ultraviolet range.

When light having a frequency different from any absorption band is incident on a material, a majority of light will simply be transmitted, reflected, or refracted. In such cases the wavelength of the light is unaffected. A small amount of light will also be scattered as a result of interactions with the polarizability tensor of the material. Most of the scattering is due to an elastic interaction and will have the same wavelength as the incident beam. This type of scattering is called the Raleigh scattering. For every 10^8 photons scattered, approximately one photon is inelastically scattered, wherein the scattered light has a different wavelength than the incident light. This inelastic scattering is called the Raman scattering and the process is termed the Raman effect. The amount of Raleigh scattering is always greater than Raman scattering, as shown in Figure 1.9 [6].

Raman scattering can occur with a change in vibrational, rotational or electronic energy of a molecule. Together with IR absorption, Raman scattering is used to obtain information about the structure and properties of molecules from their vibrational transitions

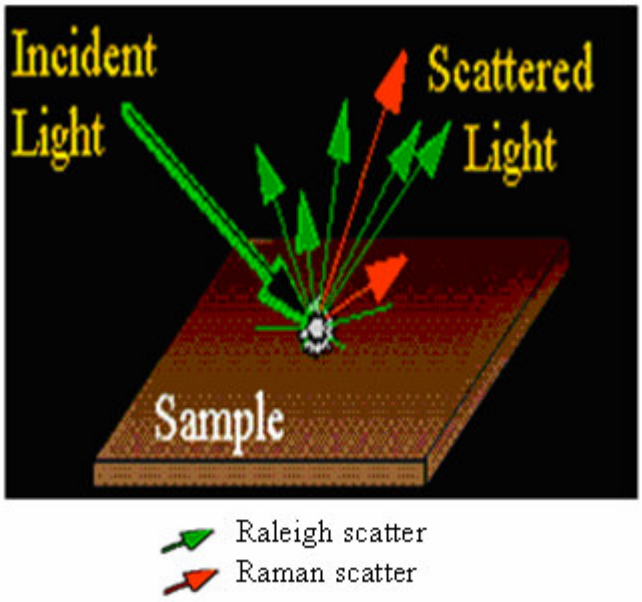

Figure 1.9 Types of light scattering

1.4.2 Theory of Raman scattering

The Raman effect is a result of interaction of a photon incident on a molecule with the electric dipole of the molecule. It is a form of electronic spectroscopy, although the spectrum contains vibrational frequencies.

Incident light is scattered at wavelengths that are shifted by degrees that correspond to the energies of vibrations within the molecules. The difference between the incident photon and the Raman scattered photon is equal to the energy of a vibration of the scattering molecule. The Raman scattered light can have both higher and lower energies than the incident light depending upon the type of transition as shown Figure 1.10 [7].

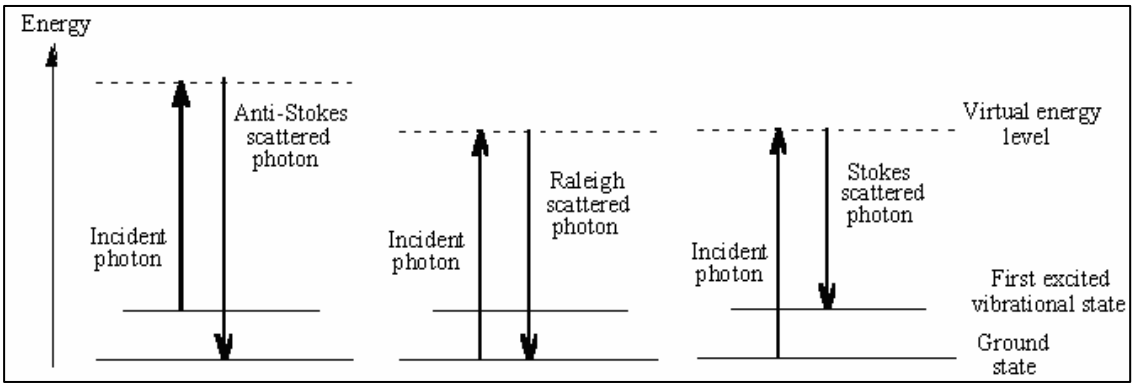

Figure 1.10 Types of transitions (a) Stokes, (b) Raleigh, and (c) Anti-Stokes

Based on the energy of the scattered radiation, Raman scattering is divided into Stokes and anti-Stokes scattering. When the energy of the scattered radiation is less than the incident radiation it is known as Stokes scattering and when the energy of the scattered radiation is greater than the incident radiation it is known as anti-Stokes scattering. The energy increase or decrease from the excitation is related to the vibrational energy spacing in the ground electronic state of the molecule and therefore the wavenumber of the Stokes and anti-Stokes lines are a direct measure of the vibrational energies of the molecule.

Numerically, the energy difference between the initial and final vibrational levels, $\bar{\nu}$, or Raman shift in wave numbers (cm^{-1}) is calculated through equation (1.1), where $\lambda_{incident}$ and $\lambda_{scattered}$ are the wavelengths in cm of the incident and Raman scattered photons, respectively. The vibrational energy is ultimately dissipated as heat, and this dissipated heat does not cause a measurable temperature rise in the material because of the low intensity of Raman scattering. A plot of intensity of scattered light or the Raman count versus difference in wavenumber is a Raman spectrum as shown in Figure 1.11 [8].

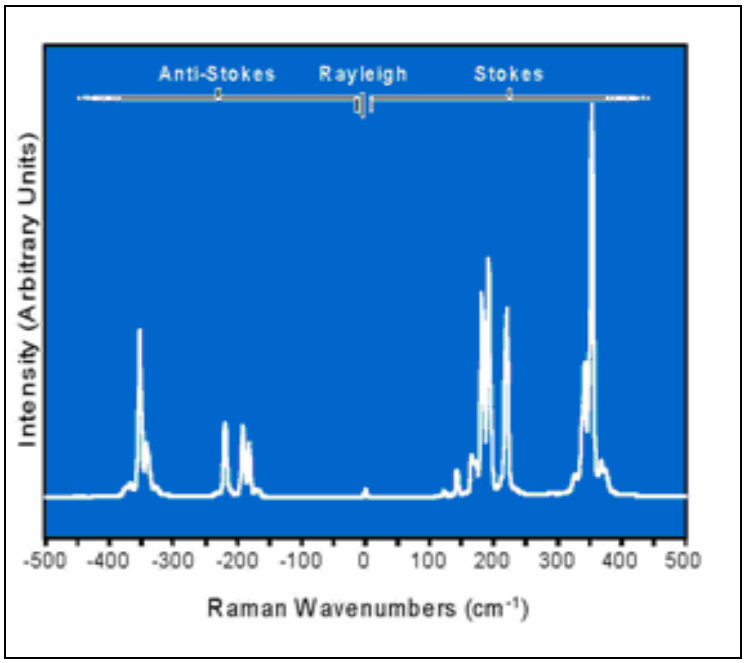

Figure 1.11 Raman spectrum showing Stokes and anti-Stokes lines

$$\bar{\nu} = \frac{1}{\lambda_{\text{incident}}} - \frac{1}{\lambda_{\text{scattered}}} \qquad (1.1)$$

The Stokes and anti-Stokes spectra contain the same frequency information. At room temperature the thermal population of vibrational excited states is low, although not zero. Therefore, the initial state is the ground state, and the scattered photon will have lower energy (longer wavelength) than the exciting photon. This Stokes shifted scatter is what is usually observed in Raman spectroscopy. The anti-Stokes shifted Raman spectrum is always weaker than the Stokes shifted spectrum.

1.4.3 Raman selection rules

A simple classical electromagnetic field description of Raman spectroscopy can be used to explain many of the important features of Raman band intensities [7]. The dipole moment, P, induced in a molecule by an external electric field, E, is proportional to the field as shown in equation (1.2). The proportionality constant α is the polarizability of the molecule. The polarizability measures the ease with which the electron cloud around the molecule can be distorted [7].

$$P = \alpha E \tag{1.2}$$

Raman scattering occurs because a molecular vibration can change the polarizability. The change is described by the polarizability derivative, $\frac{\delta\alpha}{\delta Q}$, where Q is the normal coordinate of vibration. The selection rule for a Raman-active vibration, that there be a change in polarizability during the vibration, is given by equation (1.3).

$$\frac{\delta\alpha}{\delta Q} \neq 0 \tag{1.3}$$

The Raman selection rule is analogous to the more familiar selection rule for an IR-active vibration, which states that there must be a net change in the permanent dipole moment during the vibration. From group theory it is straightforward to show that if a molecule has a center of symmetry, vibrations which are Raman-active will be silent in the IR, and vice versa. Typical strong Raman scatterers are moieties with distributed

electron clouds, such as carbon-carbon double bonds. The pi-electron cloud of the double bond is easily distorted in an external electric field. Bending or stretching the bond changes the distribution of electron density substantially and causes a large change in induced dipole moment.

In polymers, analysis of structure using Raman spectroscopy is based on the high sensitivity of the Raman effect for certain non-polar chemical groups. These groups are primarily the nearly homonuclear single and multiple C-C bonds. For polymers with C-C backbones, the Raman spectra are dominated by strong lines arising from the C-C skeletal modes. These skeletal modes are sensitive to the conformation because they are highly coupled, and any change in the conformation will vary the coupling and shift the frequencies accordingly [50].

1.4.4 Raman spectroscopy of fibers

Similar to IR spectroscopy, Raman spectroscopy has been used to characterize organic fibers since the 1960's [1]. Initially, this technique was primarily used to determine the type of polymer, the type and amount of comonomers, and the types and amounts of pigments, dyes, or other additives. Used in forensic science, archaeology, and quality control, this technique is identical to the process involved in the identification of solids and liquids, with minor modifications required for fibrous materials.

More recently, research has investigated the effect of different polymer morphologies on the Raman spectra, including crystalline form, the fraction of crystalline material and the orientation of the polymer chains relative to a unique axis within the fiber. Several bands in these spectra were observed to be sensitive to changes in the

conformation, configuration, and packing density of the polymer. For example, it has been observed that some Raman bands in a polymer appear only due to the presence of the crystalline content in the polymer. Furthermore, some of the bands in the Raman spectra have been observed to shift as tension or compression was applied to the material [1]. The potential of Raman spectroscopy in the study of polymer fiber morphology has been enhanced by the advances in Raman spectrometers, detectors, laser sources, and optical sampling systems.

1.4.4.1 Raman spectroscopy of iPP fibers

Raman spectroscopy has been widely used for studying regularity and local structures in polymers including polyethyleneterephthalate (PET), polyethylene (PE), polystyrene, polyetheretherketone (PEEK), and polytetrafluoroethylene (PTFE). The vibrational spectrum of iPP has been the subject of many reports [10-12,32-35], and the band assignments in the IR and Raman spectra are relatively well established. A portion of the Raman spectrum of iPP is shown in Figure 1.12 [9], and the vibrational assignments for the bands are given in Table 1.2 [9].

Table 1.2 Vibrational assignments for iPP

Raman shift, ω (cm-1)	**Vibrational assignment**
808	r(CH_2), ν(C-C)
841	r(CH_2)
972	r(CH_3), ν(C-C)
998	r(CH_3)
1151	ν(C-C), δ(CH)
1168	ν(C-C), r(CH_3), w(C-C)
1220	t(CH_2), w(CH), ν(C-C)

δ = bending, r = rocking, ν = stretching, t = twisting, w = wagging

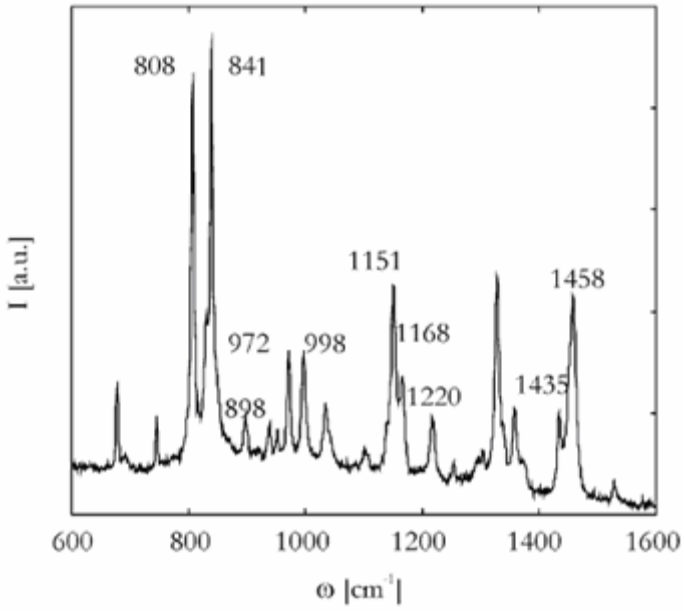

Figure 1.12 A portion of typical Raman spectrum for solid iPP

The spectrum of iPP melt, as shown in Figure 1.13 [9], contains some well known group frequencies (involving CH_2 and CH_3 groups), while other bands are due to coupled modes. By applying various theoretical and experimental methods, the distribution of conformations can be deduced from these bands [44]. Several additional bands appear in the spectrum of iPP in solid state, especially in the 800-1100 cm^{-1} range. These bands are attributed to the 3_1 helix, which is the regular conformation in all iPP polymorphs, as well as in the mesomorphic phase. Two commonly used helix bands, at 841 and 998 cm^{-1}, only appear for helix segments with at least ~14 and ~11 repeat units, respectively [44]. The bands at 898, 940, and 998 cm^{-1} are sensitive to the crystallinity [15]. The band at 1172 cm^{-1} has been used as a measure of isotacticity. The bands at 1300 cm^{-1} have been regarded as characteristic of the helical structure [15].

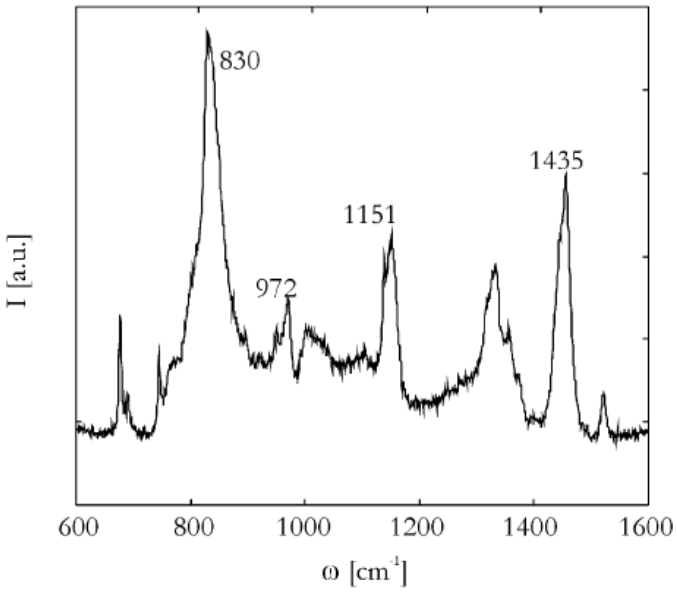

Figure 1.13 A portion of typical Raman spectrum for molten iPP

The band at 972 cm^{-1} is attributed to shorter helix segments, and is also observed with iPP melts, although at reduced intensity and a small frequency shift. For solid samples, it is sometimes resolved into two peaks, attributed to amorphous and crystalline domains. With atactic PP, this peak is usually only a shoulder as in iPP melt. This band was considered to be characteristic of the chemical structure of the head-to-tail sequence of PP units [15].

Fraser et al. [10] have conducted experiments to observe the effect of crystallinity and tacticity on the Raman spectrum of PP. Samples of PP ranging from atactic to almost purely isotactic were used in this study to obtain information on the effect of structural type on the Raman spectrum of PP. The results showed that the bands at 808 and 841cm^{-1} are broad in the samples of low crystallinity and the intensity of band at 808 cm^{-1} increased with crystallinity. The vibrations at 808 and 841 cm^{-1} were found predominantly due to methylene (CH_2) rocking in the 3_1 helix. Tadokoro et al. [11] also

have assigned both vibrations to CH_2 rocking and have interpreted their observed wavenumber difference to the strong coupling with the skeletal stretching of the 808 cm^{-1} band.

Fraser et al. [10] also reported that a doublet was observed at 1151 cm^{-1} and 1168 cm^{-1}, which was also sensitive to crystallinity. The band at 808 cm^{-1} was due to the crystalline moieties, whereas the band at 841 cm^{-1} was due to non-crystalline and/or due to low molecular weight content in the material. This group also stated that as one approaches and exceeds the melting point of iPP the regular structure of the chains becomes so short that the CH_2 rocking mode reverts to a band characteristic of the CH_2 group in a randomly oriented hydrocarbon system. The spectrum obtained for molten iPP was similar to that of aPP. It was observed that the Raman spectrum of PP obtained by moderately slow cooling from the melt was very similar to that of molten PP, where as spectrum recorded for quenched melts indicated high crystallinity. This observation is in not in line with similar works conducted later [9,13].

Zerbi et al. [12] concluded from IR data that molten iPP retains some form of crystalline structure that might act as a seed for further crystallization upon cooling. The vibrations at 808 and 841 cm^{-1} have been the interest of several investigations in the past.

Nielsen et al. [9] were the first to develop a method to calculate percent crystallinity in iPP using Raman spectroscopy in 2001. In their study, percent crystallinity was calculated using the ratios of three bands; 808 cm^{-1}, 830 cm^{-1}, and 841 cm^{-1}. The vibrational assignments of the bands observed in this study were in agreement with that of Fraser et al. [10]. Neilsen et al. [9] observed that a broad band at 830 cm^{-1} in the melt split into 808 and 841 cm^{-1} upon solidification, resulting in a three phase structure. They

explained in their work that the band at 808 cm^{-1} was due to helical chains in crystal region, 830 cm^{-1} was due to the atactic chains which were in a non-helical conformation, and 841 cm^{-1} was due to the disruptions in the helix.

A general relationship between the scattering intensities is shown in equation 1.4, where I_{ref} is the reference intensity, C_a, C_b, and C_c are the calibration constants, with the subscripts a, b, and c representing the amorphous, defect, and the crystal phase respectively. It was found that the intensity sum of bands at 808, 830, and 841 was independent of chain conformation or crystallinity. By using this intensity sum as reference, and with $C_a = C_b = C_c$, the fraction of crystalline phase, χ^c, was determined by equation 1.5, where I is the intensity of the band. Crystallinities for iPP off-line samples with different thermal history were estimated using this equation. Results were compared to DSC and a good correlation was found as shown in Figure 1.14 [9]. In this figure, χ^a and χ^b are the fractions of amorphous and defect phase respectively. A decrease in percent crystallinity and a simultaneous increase in the number of chains in a non-helical conformation were observed with increasing cooling rate.

$$C_a (I_{808} / I_{ref}) + C_b (I_{841} / I_{ref}) + C_c (I_{830} / I_{ref}) = 1 \qquad (1.4)$$

$$\chi^c = I_{808} / (I_{808} + I_{830} + I_{841}) \qquad (1.5)$$

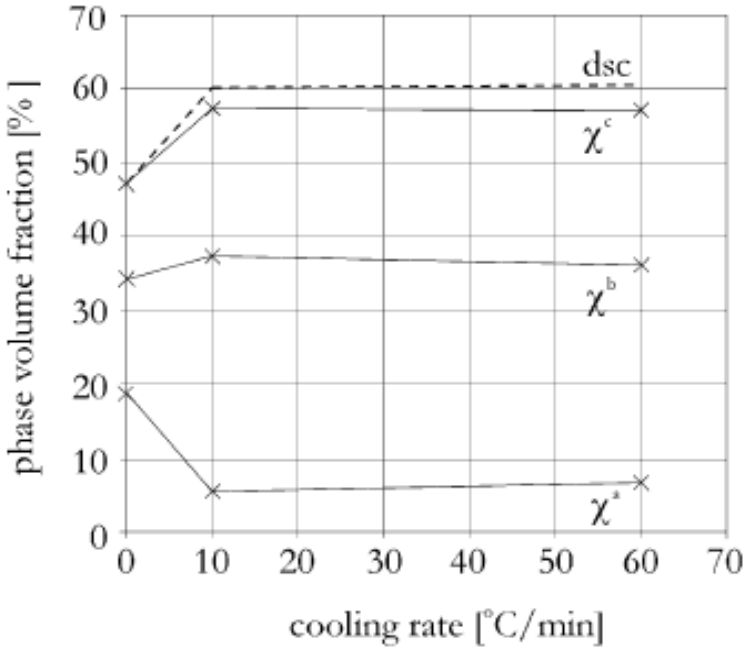

Figure 1.14 Influence of annealing time on percent crystallinity by Nielsen et al.

Recently Minogianni et al. [13] found that one more band at 854 cm^{-1} also contributed to the crystallinity calculations in iPP. They reported that all non-crystalline domains in iPP resulted in a primary peak at 841 cm^{-1} and two other minor peaks at 830 and 854 cm^{-1}. The fraction of crystalline phase, χ^c, was determined using equation 1.6, which is a modified form of equation 1.5. Crystallinities for iPP off-line samples with different thermal history were estimated using this equation. Results were compared to DSC and a good correlation was found as shown in Figure 1.15 [13].

$$\chi^c = I_{808} / (I_{808} + I_{830} + I_{841} + I_{854}) \qquad (1.6)$$

.

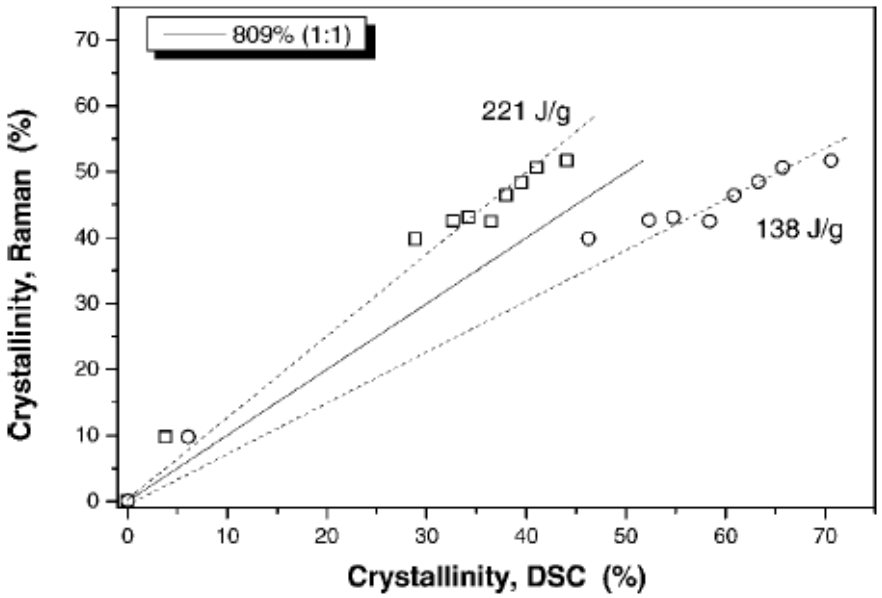

Figure 1.15 Comparison between percent crystallinity by Raman and DSC using the highest and lowest theoretical values for the heat of fusion of iPP found in the literature by Minogianni et al.

Paradkar et al. [14] were the first to conduct on-line polarized Raman spectroscopic studies to estimate molecular orientation in iPP fibers. iPP fiber samples with six different draw ratios were used for characterization during melt spinning. This group used solid samples in their work and did not study the evolution of molecular orientation from the melt during melt spinning. Raman spectra were collected in XX direction (along the fiber direction) of the spinline. The ratio of the Raman bands at 841 and 808 cm^{-1} was used to estimate molecular orientation in iPP fibers. Results were compared to birefringence measurements and a good agreement was observed, as shown in Figure 1.16 [14]. They concluded that Raman spectroscopy could be used to monitor the development of polymer morphology (crystallinity and orientation) as a function of processing parameters along the entire length of the spinline.

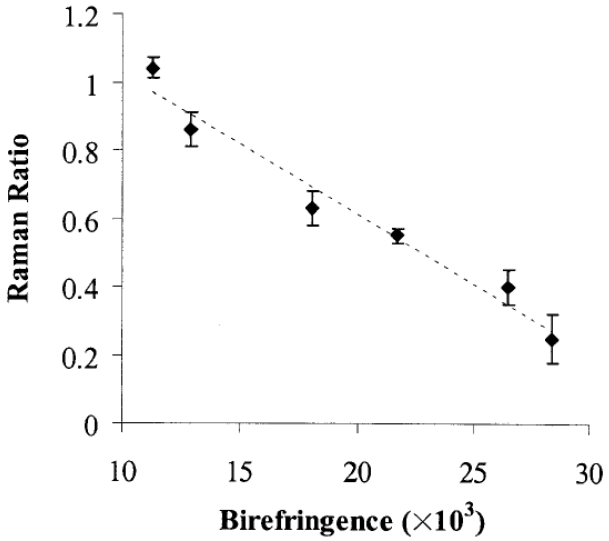

Figure 1.16 Plot of birefringence vs Raman intensity ratio by Paradkar et al.

Ran et al. [15] conducted simultaneous WAXD and Raman spectroscopic studies on the drawing of iPP fibers. Pre-spun iPP fibers were drawn using a stretching apparatus and an additional custom-built vertical translational stage. The combined methods yielded complementary information on the structural evolution in both crystalline and amorphous phases within the fibers. WAXD results indicated that the α-form crystals were converted into mesophase upon stretching at room temperature. Raman spectra showed that characteristic bands from the crystal phase became weaker or disappeared during the transition from α-form to mesophase form; however the overall orientation of the fiber increased during drawing, as indicated by the Raman intensity ratio of 808/841 cm^{-1}.

1.5 Wide angle x-ray diffraction (WAXD)

WAXD is one of the earliest techniques used to study the structure of polymers. The usefulness of WAXD in the study of polymer structure lies in its ability to

distinguish ordered from disordered states. Amorphous materials, such as liquids and glasses produce x-ray patterns of a diffuse nature consisting of one or more halos; on the other hand, crystalline materials exhibit patterns of numerous sharp circles or spots. This ability to reveal the degree of ordering in polymers makes WAXD well suited for structure development studies in polymers. WAXD can give information about crystal structure, the crystallinity and the morphology of samples which may be either uniaxially oriented fibers, bulk specimens or films. The crystallinity of unoriented samples can be readily determined using standard procedures with reference to the pattern of the amorphous polymer. In oriented samples, appropriate averaging procedures are necessary to obtain reliable crystallinity values [16].

WAXD generally requires a source of monochromated radiation, which for convenience is usually Cu-Kα [16], giving optimum compromise between resolution and scattered intensity. Two types of scattering are observed, coherent, or unmodified, and incoherent, or modified [17]. The bulk of the energy of scattering goes into coherent scattering, which can be utilized for structural studies as it occurs without change of wavelength, and without loss of phase relationship between the incident and the scattered rays.

X-rays are generated when high energy electrons impinge on a metal target such as copper, iron, and molybdenum. When x-rays of a given wavelength impinge on the atoms, the incident x-rays are scattered by the atoms and the electrons in the atoms become secondary emitters of x-rays. These secondary waves generated by the individual atoms would be in phase only when their path lengths differed by some whole number of the wavelength [17]. This would result in a constructive interference and diffraction of

the scattered x-rays. Only selected orientations of the crystal with respect to the incident x-ray beam will yield diffracted rays, and constructive interference in one direction.

A relation between the x-ray wavelength λ, the interplanar spacing d, and one half the angle of deviation of the diffracted rays from the incident x-rays θ, was derived, which was similar to Bragg's law as shown in equation 1.7. By means of simple geometrical construction shown in Figure 1.17 [41] the validation of this equation can be demonstrated on the assumption that x-rays are "reflected" by a set of crystallographic planes in the same way as light rays are reflected by a mirror.

$$n \lambda = 2 d \sin \theta \qquad (1.7)$$

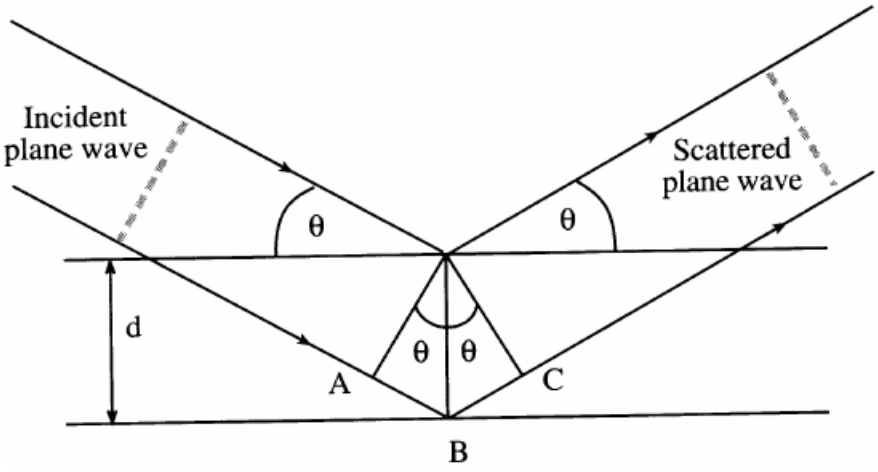

Figure 1.17 The Bragg description of diffraction in terms of reflection of a plane wave

The figure shows x-rays of wavelength λ impinging at an angle θ on two adjacent planes of a set (hkl) separated by an interplanar distance d, and the reflection is of first order (n = 1) from the given planes. At particular larger values of θ, n will equal 2, 3, 4, etc., giving rise to reflections of second, third, fourth, and higher orders from the same set

of planes. For all values of θ that do not satisfy Bragg's law the reflected (diffracted) rays will be out of phase with each other and no actual reflected x-rays will be observed [17].

1.5.1 WAXD of iPP fibers

The diffraction pattern of iPP can be separated into sharp (crystalline) and diffuse (amorphous) components as shown in Figure 1.18 [26]. The arcs correspond to different crystallographic planes and are formed as a result of diffraction from these planes. Underlying these arcs is the amorphous halo, which is due to the scattering from amorphous regions. The diffraction peaks can be determined by the corresponding integrated intensity profile of the WAXD pattern.

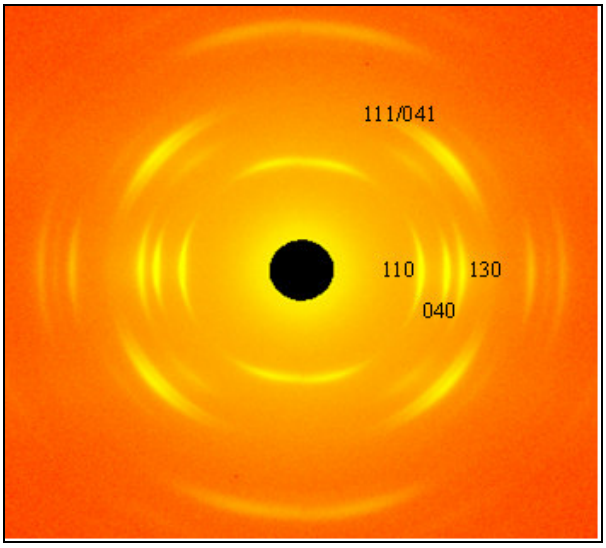

Figure 1.18 Typical WAXD pattern for α-form iPP

Each diffraction peak is assigned to a different crystallographic plane, which is helpful in identifying the crystalline forms in the material. For example, in iPP, the integrated intensity profile for α-form is different compared to the integrated intensity

profile for β-form or γ-form as shown in Figure 1.19 [42]. The mesomorphic form exhibits two broad peaks instead of the well known four sharp peaks of the α-form.

The α-form is the most common crystalline form present in iPP. The integrated intensity profile of the α-form has four diffraction peaks as shown in Figure 1.19, which are due to the planes (110), (040), (130), and a combination of (111) and (041). The intercepts for all the planes are given in Table 1.3. Crystallinity in iPP fibers can be estimated using these integrated intensity profiles by determining the areas under the diffraction peaks and dividing them by the total area (including the area of the amorphous halo). Calculation of crystallinity using this method will be demonstrated in the Results and Discussion section (Chapter 3).

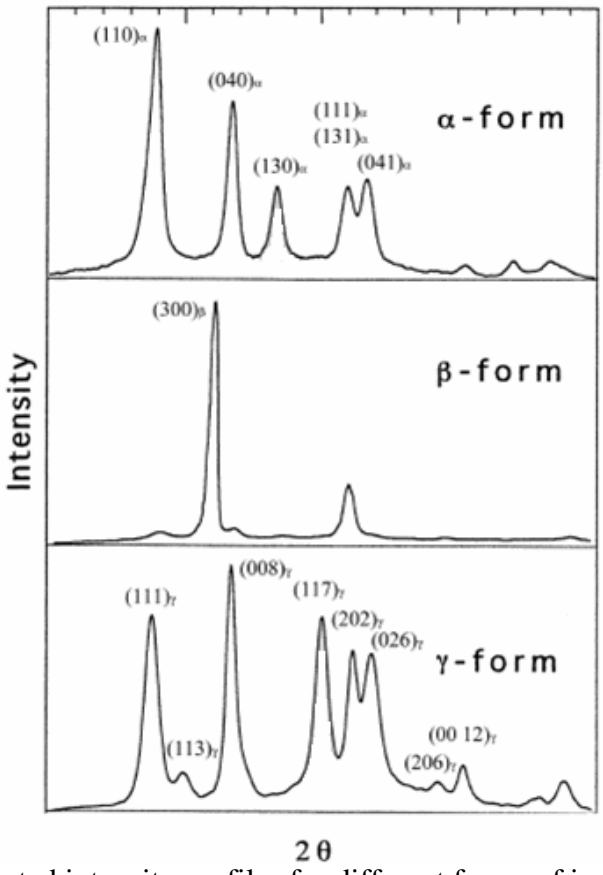

Figure 1.19 Integrated intensity profiles for different forms of isotactic polypropylene

Table 1.3 Intercepts for crystallographic planes of α-form isotactic polypropylene

Plane	Miller Indices	Reciprocals	Cleared of Fractions	Intercepts
110	(110)	1/1, 1/1, 1/0	1, 1, ∞	1a, 1b, ∞c
040	(040)	1/0, 1/4, 1/0	∞, 4, ∞	∞a, 4b, ∞c
130	(130)	1/1, 1/3, 1/0	3, 1, ∞	3a, 1b, ∞c
111/041	(111)/(041)	1/1, 1/1, 1/1 1/0, 1/4, 1/1	1, 1, 1 ∞, 1, 4	1a, 1b, 1c ∞a, 1b, 4c

Orientation in fibers can also be determined using WAXD. The orientation of crystallographic planes (110) and (040) with respect to the fiber axis is typically determined. Then the Herman orientation factor, f_z, is calculated using a set of equations which will be explained in detail in the Experimental section (Chapter 2).

Although it has been accepted since the pioneering work of Carothers and Hill [18] in 1932 that the structure and properties of melt spun fibers depend on the spinning conditions used in their manufacturing, there still exists a dearth of information in open literature on this subject. Until the work of Keller [19] in the mid 1950's, there were no published studies on the structures of melt spun fibers. The most notable early work is that of Ziabicki and Kedzeirska in the late 1950's and early 1960's [27-31]. These authors used x-ray patterns and birefringence as a measure of molecular orientation and followed its variability with spinning conditions. These studies emphasized crystallographically complex polymers [23]. They concluded that molecular orientation increased with spinline tension (taken as the difference between the take-up and extrusion velocities) and decreased with increase in filament diameter.

Sheehan and Cole were the first to study the melt spinning of iPP [20]. They showed that monoclinic iPP is produced under normal air quenching conditions, whereas

quenching in cold water produced a paracrystalline smectic structure. While a number of works which contained studies of the structure of melt spun fibers appeared in succeeding years, it was not until the publications of Katayama, Amano and Nakamura [21] that a clear picture of structure development began to emerge.

On-line WAXD measurements of crystallization in the spinline were first reported by Chappel et al. [22] of British Nylon Spinners, followed by Katayama et al. [21]. Katayama et al. [21] collected x-ray data along with temperature, birefringence, and diameter profiles during melt spinning of PE, PP, and polybutene-1. This work appears to be the first to have demonstrated that crystallization kinetics may be greatly enhanced during melt spinning, as compared to quiescent conditions, due to the molecular orientation caused by stretching and cooling of the melt. A special model spinning apparatus was employed in this work, where the extruder was moved up and down the spinline for data collection along the spinline, and a polarizing microscope with Berek compensator was used for birefringence measurements.

Nadella et al. [23] studied the effect of Hermans orientation factor, amorphous orientation factor, and birefringence on the mechanical properties of melt spun iPP. They observed that there was no significant difference between the correlations provided by these various parameters within the range of variables studied.

The next notable work is that of Kolb et al. [25]. This group collected small and wide angle x-ray scattering data simultaneously during low speed spinning of PP. The throughput rate was kept constant for different take-up velocities and extrusion temperatures. At a spinning temperature of 210 °C, the onset of crystallization was observed at 45 cm from the spinneret for all take-up velocities. The evolution of

crystallinity was the same for all take-up velocities. They concluded that the molten amorphous phase was completely unoriented and highly oriented crystals grew out of an anisotropic amorphous matrix. The orientation of these crystallites was found to remain constant during crystallization.

1.6 Differential scanning calorimetry (DSC)

The assessment of a polymer's percent crystallinity can be most easily performed using DSC which measures the difference in heat flow rate between a sample and inert reference as a function of time and temperature. The heat flow can be of two types, endothermic and exothermic. Endothermic heat flows into the sample as a result of either heat capacity (heating) or some endothermic process (glass transition, melting, evaporation, etc), and exothermic heat flows out of the sample as a result of either heat capacity (cooling) or some exothermic process (crystallization, cure, oxidation, etc.). A typical DSC thermogram is shown in Figure 1.20 [45].

The enthalpy of fusion, ΔH_m (J/g), and cold crystallization, ΔH_c (J/g) are determined by integrating the areas under the peaks of melting and crystallization respectively. Depending upon a given sample's thermal history, a cold crystallization exothermic peak may or may not be observed during the DSC experiment. The percent crystallinity is then determined using the equation 1.8. In this equation, the heats of melting and cold crystallization are in units of J/g. The term ΔH_m^0 is a reference value and represents the heat of melting for a pure 100% crystalline polymer.

$$\% \text{ Crystallinity} = 100 * (\Delta H_m - \Delta H_c) / \Delta H_m^0 \qquad (1.8)$$

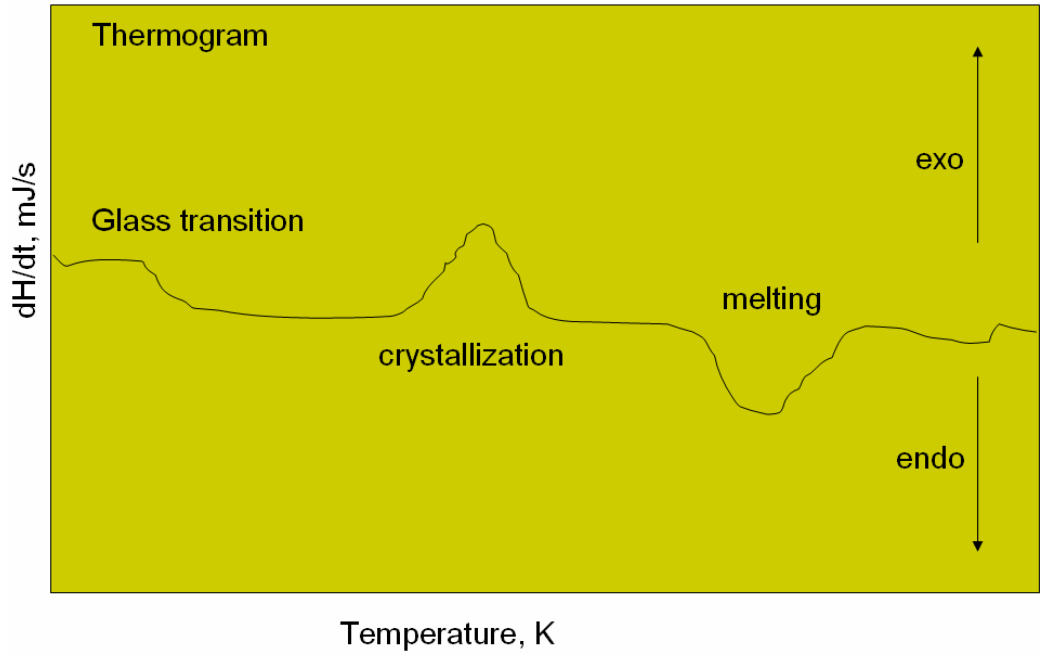

Figure 1.20 Typical sketch of a DSC thermogram for a polymer

1.7 Birefringence

Birefringence is a measure of the overall molecular orientation in a material, as it covers both amorphous and crystalline regions [49]. It is formally defined as the double refraction of light in a transparent, molecularly ordered material, which is manifested by the existence of orientation-dependent differences in refractive index [51]. Birefringence can be measured using a polarized light microscope for materials which are anisotropic (having two or more refractive indices) and which transmit light. When light rays pass through an anisotropic substance such as a fiber, the light is refracted in two different directions as shown in Figure 1.21 [51]. The phase difference between the two refracted light rays is known as retardation, and birefringence can be calculated once the retardation is determined.

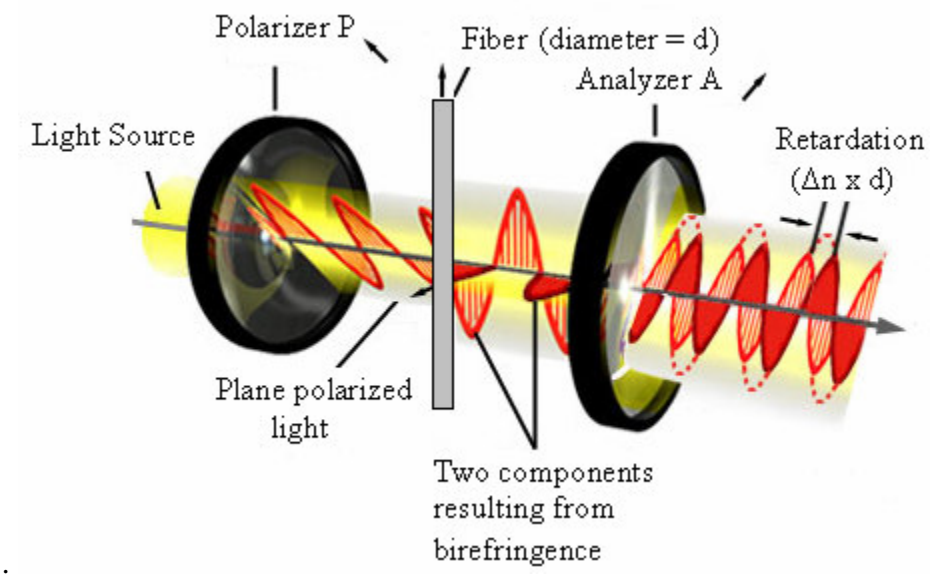

Figure 1.21 Refraction of light passing through a fiber resulting in birefringence

In polymer fibers the differences are most distinct in the longitudinal and transverse directions with respect to the fiber axis. The birefringence of a fiber primarily depends on the base polymer and the amount of drawing the fiber has undergone. The greater the degree of orientation, the higher the birefringence. The birefringence of the fiber can be determined by measuring retardation (compensation methods) or by measuring the different refractive indices. The compensation methods give an average birefringence value for the whole fiber cross-section.

The data on birefringence of a polymer fiber might differ according to what method has been employed to measure same [49]. In compensation methods, the interference bands (if monochromatic light is used) or interference colors (if multichromatic light is used) are observed and then compensated by various compensators. When passing through the fiber, the linear polarized light is divided into two components oscillating in the planes perpendicular to one another. These rays

propagate at different velocities and due to this certain wavelength are eliminated, attenuated or amplified. As a result interference colors or band are formed. The order or color of interference bands is determined and the corresponding retardation value is looked up in the interference color chart. When tilting compensators are used, the tilting angle is determined and the corresponding retardation value is looked up in the chart provided by the compensator manufacturer. Once retardation is determined, birefringence (Δn) is calculated using equation 1.9.

$$\Delta n = \text{Retardation (nm)} / \text{Fiber diameter or thickness (nm)} \qquad (1.9)$$

The most accurate way to measure fiber birefringence is to determine both refractive indices using a Mach Zehnder Interference microscope, which is also explained in Chapter 2 (Experimental). In this method the birefringence is given by equation 1.10,

$$\Delta n = n_{//} - n_{\perp} \qquad (1.10)$$

where Δn is the birefringence, $n_{//}$ is the refractive index of the fiber in the longitudinal direction and $n_{\perp}$ is the refractive index of the fiber in the transverse direction with respect to the fiber axis.

1.8 Objectives

The work reported here was conducted as a Center for Advanced Engineering Fibers and Films (CAEFF) project. The main objective of CAEFF is to develop

mathematical models that can predict the final properties of fibers and films, as confirmed by the experimental results. Using these validated mathematical models a manufacturer can tailor raw material selection and/or process condition to obtain products with desired end-use properties.

In relation to this study, graduate students at CAEFF previously conducted on-line experimental works to validate simulation models. For example, Paradkar et al. [14] conducted on-line polarized Raman spectroscopic studies during the melt spinning of iPP fibers, while S. S. Cherukupalli [47] studied the real-time development of microsctructure, velocity, diameter, and temperature along the axial distance of the blown film line for LLDPE under various processing conditions. In addition, S. Varkol [46] collected velocity, diameter, and temperature data along the spinline during the melt spinning of iPP under different processing conditions, investigating their effect on mechanical properties of iPP fibers. P. E. Lopes [26] investigated the effect of processing conditions on the structure development of iPP during melt spinning using simultaneous WAXD and small angle x-ray scattering (SAXS). On-line velocity, diameter, and temperature measurements were also collected in this work.

As a continuation of this prior work conducted at CAEFF, the objectives of the current research are:

1. To study the real-time development of structure along the spinline during the melt spinning of iPP, as the fibers transform from a molten state to a solid state.
2. To collect data along the spinline during melt spinning using Raman spectroscopy polarized Raman spectroscopy, and WAXD simultaneously.

3. To study the effect of throughput rate and take-up velocity on the structure development of iPP fibers.
4. To compare and contrast Raman spectroscopy results with x-ray results.
5. To supply data for the designing and testing of mathematical simulation models developed in CAEFF.

CHAPTER 2

EXPERIMENTAL

In this chapter a detailed description of materials, instrumentation, and processing conditions used in the study will be presented, followed by data collection and analysis. Raman spectroscopy and wide angle x-ray diffraction (WAXD) data were collected at exactly the same positions along the spinline during melt spinning of isotactic polypropylene (iPP) fibers. Melt spun fibers were collected on a bobbin and were characterized off-line using Raman spectroscopy, WAXD, differential scanning calorimetry (DSC), and birefringence measurements.

2.1 Materials used

The polymers used in this study were Pro-fax PH 835 (PP 35) and Pro-fax PDC 1267 (PP18) iPP chips supplied by Basell Inc., Canada. PP 35 had a melt flow index of 35 (g/10 min at 230°C) and a polydispersity index of 2.69 [46], and PP 18 had a melt flow index of 17.5 and a polydispersity index of 3.55 [36]. Cyclohexane (Fisher Scientific) was used for laser wavelength calibration in Raman spectroscopic studies, and refractive index oils (Cargille Laboratories, 1.494) were used for birefringence studies.

2.2 Extruder

The extruder used in this study was a motor driven single screw extruder manufactured by Alex James, Inc, as shown in Figure 2.1, which was designed to deliver

molten polymer at constant pressure to the melt pump. A schematic of the melt spinning setup used in this study is shown in Figure 2.2. The extruder screw had a length of 15" and a diameter of 5/8" giving an L/D ratio of 24:1. The extruder barrel had three heating zones corresponding to the feeding, compression and metering zones of the screw and the temperature of these zones were controlled manually. The melt pump used had a capacity of pumping 0.297 cc of material per revolution, and the rpm of the melt pump was used to control the flow rate. The temperature of the mixer and spin head, the extruder pressure, and the rpm of the melt pump were also controlled manually.

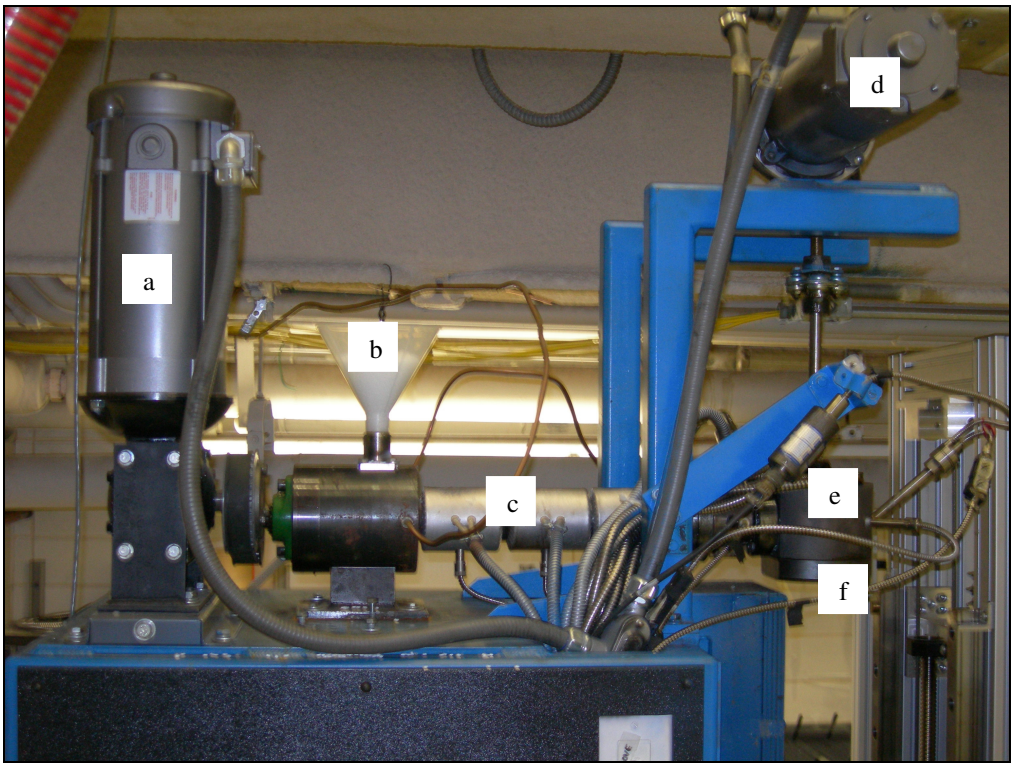

Figure 2.1 Single screw extruder: (a) Motor for extruder screw, (b) Hopper, (c) Barrel, (d) Motor for melt pump, (e) Melt pump and spin head, (f) Spinneret and spinneret holder

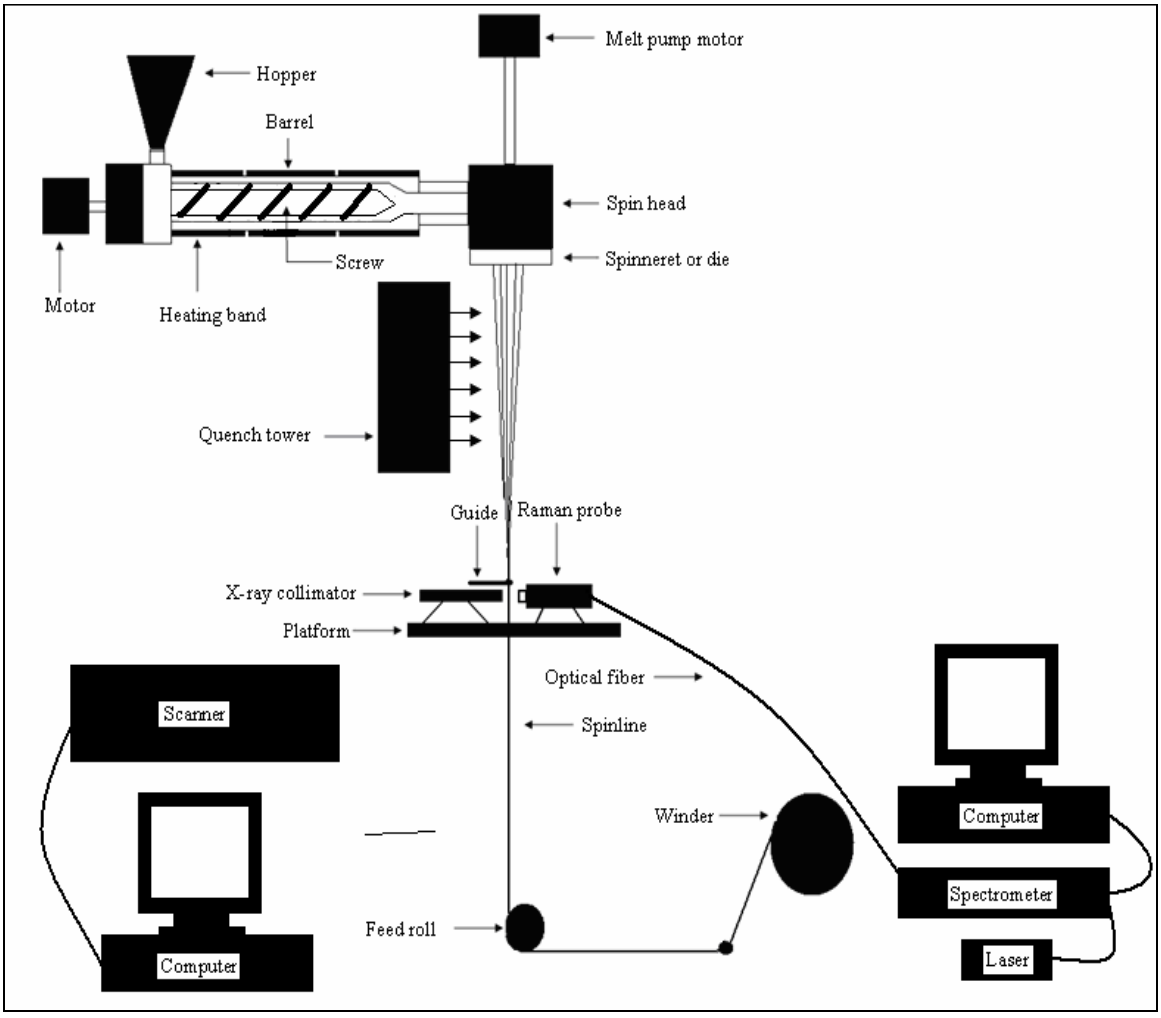

Figure 2.2 Schematic of melt spinning setup

Two different spinnerets were used. Both were six hole spinnerets with a L/D ratio of 3:1 and an entrance angle of 30°, as shown in Figure 2.3 (a). The only difference between these spinnerets was the positioning of the holes. One spinneret had symmetrical positioning of the holes ('O' spinneret), as shown in Figure 2.3. All six holes were positioned symmetrically about the center of the spinneret. The other spinneret had a non-symmetrical positioning of the holes ('W' spinneret), as shown in Figure 2.4. The 'W' spinneret was used only in the preliminary work, which will be presented in Results and

Discussion section (Chapter 3). A quench tower assisted in cooling of extruded fibers with a linear air velocity of 1m/s at ambient temperature. A *Speedaire* aspirator was used to collect the extruded fibers, place them through the guide, around the feed roll, and to the winder, i.e. to thread-up the machine.

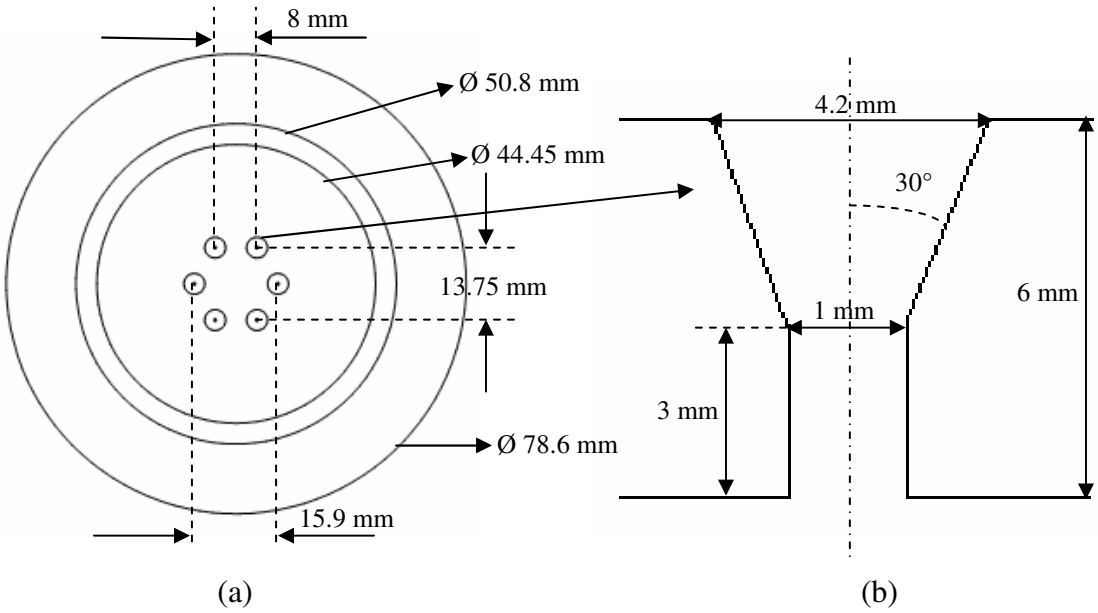

Figure 2.3 (a) Six hole spinneret and its dimensions, (b) Dimensions of a single hole

The extruded fibers were wrapped once around the 4" diameter feed roll to maintain constant take-up velocity, and then finally wound onto packages (6" outer diameter and 5.5" inner diameter) using a *Leesona* constant tension winder. The surface speed of the winder was set approximately 5% faster than the feed roll to maintain tension while collecting the fibers. A tachometer from *Extech Instruments* was used to set the surface speed of the winder.

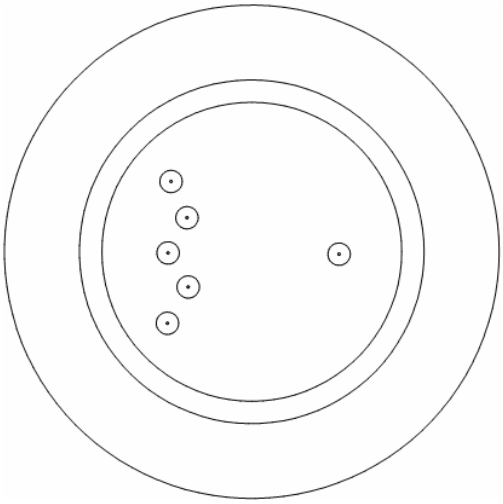

Figure 2.4 Six hole non-symmetrical spinneret ('W' spinneret)

A Teflon coated 'pig-tail' guide was used to position the spinline for Raman and x-ray measurements. The main processing variables used in this work were take-up velocity and throughput rate. Two take-up velocities (400 and 800 m/min) and two throughput rates (0.67 and 0.89 g/min/hole) were used based on previous works conducted [26, 46]. The four drawdown ratios calculated for the four different spinning conditions are given in Table 2.1. All other processing parameters were kept constant. The processing temperatures and pressure used are given in Table 2.2.

Table 2.1 Spinning conditions and drawdown ratios

Take-up velocity (m/min)	**Throughput rate (g/min/hole)**	**Drawdown Ratio (DDR)**
400	0.89	264
	0.67	353
800	0.89	529
	0.67	705

Table 2.2 Extruder temperatures and pressure

Barrel zone 1	150°C
Barrel zone 2	180°C
Barrel zone 3	210°C
Mixer	210°C
Spin head	220°C
Extruder pressure	500 psi

2.3 CAEFF on-line data collection setup

The x-ray system used in this study was designed by Rigaku-MSC, Houston, TX, for CAEFF. To facilitate spinline access at different distances from the exit of the spinneret during melt spinning, the x-ray generator, collimator, and detectors were mounted on a platform which was attached to an elevator. The platform could vertically travel a distance of 62 cm, allowing data collection from 8 to 70 cm from the exit of the spinneret, as shown in Figure 2.2. A Sanyo Denki stepper motor was used to control the vertical motion of the platform. The minimum possible step size was 1 mm. The motor was computer controlled, using the interface software *'Spectre'*.

2.4 Wide angle x-ray diffraction (WAXD)

2.4.1 Instrumentation

The x-ray system was designed for on-line characterization of polymer fibers both by WAXD and small angle x-ray scattering (SAXS) simultaneously. In this research only WAXD data was collected and analyzed. Details on the operation of CAEFF x-ray system is given elsewhere [26].

The main components of this x-ray system were the x-ray generator, detectors, motion controls, and the image plate handling robot. The x-ray generator was a Micromax 2 from Osmic, Inc., which used a Microsource x-ray tube from Bede Scientific Ltd., coupled with a two-dimensional multilayer optics system, Microfocus Confocal Max-Flux Optic (μCMF) [26]. The microstructure x-ray tube uses a micro-focused electron beam impinging on a copper target to produce x-ray radiation beam. The x-ray beam was then focused and monochromatised by the μCMF, to provide a Cu $K\alpha_1$ x-ray beam having a wavelength of 0.15406 nm and a 0.5 mm diameter at the sample position (at approximately 70 cm from the x-ray source). Once the x-ray beam exited the source it passed through an external shutter and then through a 173 mm long pinhole collimator. The path between the x-ray source and the exit of the collimator was flushed with Helium to enhance the beam intensity.

The detectors used in this system were Fujifilm BAS-IP MS2325 image plates (IPs), custom cut into 23 x 20 cm to fit the holders [26]. The IP was secured in the holder using vacuum. The detector was protected from other radiation by a black screen mounted in a frame in front of the IP holder. The detector allowed the detection of the diffraction pattern from 3.5^0 to 40^0 (2θ) in vertical direction, 3.5^0 to 14^0 (2θ) on the right side and 3.5^0 to 60^0 (2θ) on the left side in the horizontal direction [26]. The transfer of IP from one station to other was performed by Mitsubishi RV-E2 robot with a CR-E116 robot controller.

2.4.2 Sample positioning

A Teflon coated 'Pig-tail' guide, as shown in Figure 2.11 was used to position the fibers in the spinline in order to facilitate on-line data collection. This guide served to consolidate the fibers into a bundle and reduce vibration in the spinline. The guide was positioned such that no undue tension was placed on the spinline. The spinline was centered approximately 1.5 cm from the collimator. The position of the spinline in front of the collimator was monitored using two *Sony* video cameras, one on top of the collimator and the other at 90° to the collimator. While viewing the spinline on the two monitors, the fibers were positioned in the x-ray beam path using the guide. The distance of the spinline from the wide angle detector was 10 cm.

A sample mounting block was used to position the fiber bundle in order to facilitate off-line data collection. The as-spun fiber bundle was mounted on the sample holder as shown in Figure 2.5. The fiber bundle was positioned in front of the collimator in the same way as for on-line measurements.

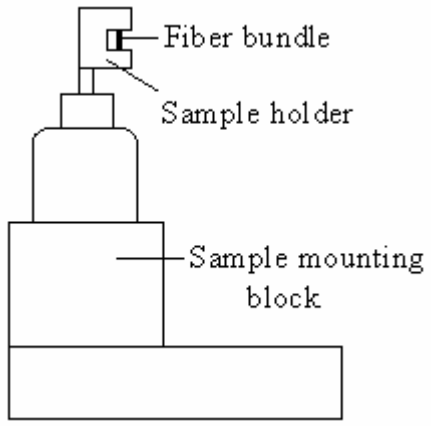

Figure 2.5 WAXD off-line sample mounting block

2.4.3 Data collection and analysis

The x-ray generator was set to 45 kV and 0.67 mA. A 0.5 mm collimator with 0.5 mm rear aperture was used for all x-ray data collection. The exposure time was 20 minutes, the same amount of time used in the previous work [26]. Background and off-line images were also collected using the same exposure time. At least two separate fiber bundles were analyzed for each spinning condition for off-line measurements.

WAXD image processing and data analysis were performed using *Polar* software, version 2.7.0, from STAR – Stonybrook technology and applied research [26]. Percent crystallinity and orientation parameters were determined using the WAXD images collected. *GRAMS/32* software was also used to calculate percent crystallinity from the *Polar* integration profiles.

The IPs were scanned at a resolution of 200 μm per pixel using a *Fujifilm BAS 1800 II* scanner. Initially the images were in *Fuji* format when scanned. The center of the pattern in each image was determined first using x-y profiles for all the collected images. Then the images were calibrated for a given x-ray wavelength, sample to detector distance and detector pixel size. Once calibrated the images were saved in *Polar* format. This was followed by background subtraction, where the WAXD background image was subtracted from the sample image. Figure 2.5 (a) and (b) show an example of unprocessed and background subtracted WAXD images. The multiplier factor was adjusted to obtain an integration intensity close to zero, which was determined by the integration profile. After background subtraction the center of the resulting image was erased within 40 pixels of radius by using the "Zero selected area" option. This eliminated the high intensity areas as a result of difference in alignment of IP hole or the

beam spot shadow between the sample and the background images [26]. The resulting images were again saved in *Polar* format.

2.4.3.1 Percent crystallinity calculations

The integrated intensity profiles obtained after subtracting and center clearing the WAXD images was saved as a *spc* file. This file was then opened using *GRAMS/32* and using a mixed Lorentzian-Gaussian fit the area under the halo profile and the four peaks corresponding to (110), (040), (130) and an overlapping of (111/041) were determined. The degree of crystallinity was calculated using the ratio of areas under the peaks mentioned above, which will be discussed in detail in the Results and Discussion section (Chapter 3).

2.4.3.2 Orientation calculations

Once the images were background subtracted and the centers erased, they were *Fraser* corrected to convert the image pixel from detector position to scattering vector *s* [26]. An example of *Fraser* corrected WAXD image is shown in Figure 2.6 (c).

The data from the second and third quadrant of the *Fraser* corrected image was then curve fit in the range of 40 to 440 pixels. After curve fitting, two images were generated using *Polar*. The *Halo image* was due to the isotropic component corresponding to the minimum intensities calculated during curve fitting and the *Corrected image* was due to the anisotropic component corresponding to the remaining intensities [26] as shown in Figure 2.7.

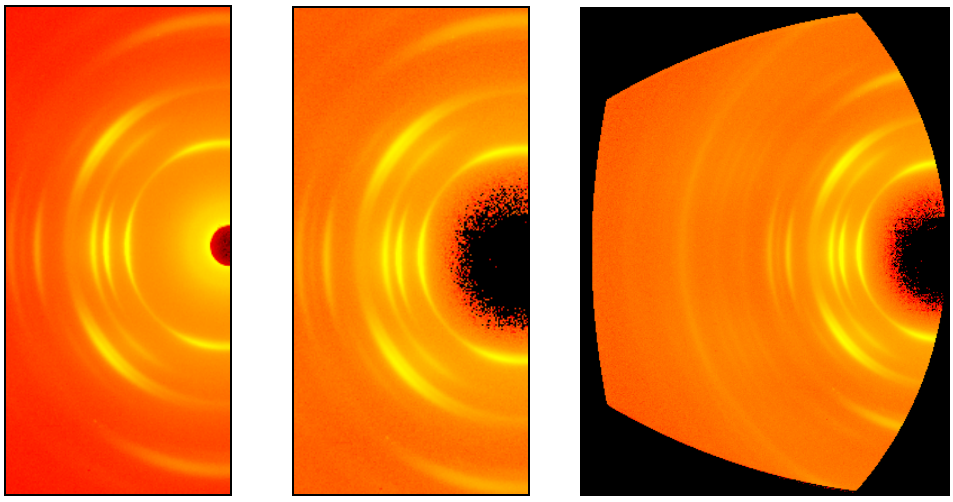

(a) (b) (c)

Figure 2.6 WAXD images obtained before and after processing using *Polar* for as-spun iPP fiber, (a) Unprocessed image, (b) Background subtracted and center cleared image, (c) *Fraser* corrected image.

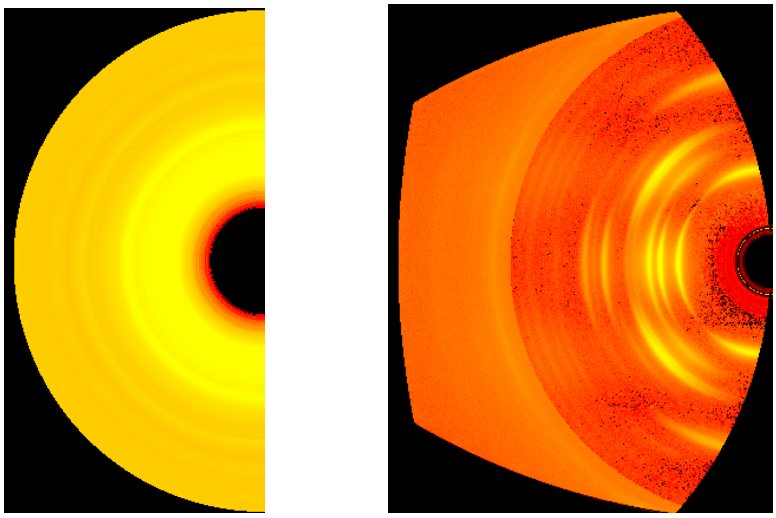

(a) (b)

Figure 2.7 WAXD image processing by *Polar* of an image obtained for as-spun iPP fiber, (a) Halo image and (b) Corrected image

After curve fitting, the orientation parameters were determined for 110 ($f_{110,x}$) and 040 ($f_{040,x}$) peaks, which correspond to 110 and 040 crystallographic planes. Then the angle between the c-axis (chain axis) and crystallographic planes 110 ($\cos^2 \Phi_{110,x}$) and 040 ($\cos^2 \Phi_{040,x}$) was calculated using equation 2.1. Using equation 2.2 the angle between the c-axis and fiber axis ($\cos^2 \Phi_{c,x}$) was calculated. The c-axis orientation of the monoclinic α-form, i.e. the Hermans orientation factor ($f_{c,x}$), was calculated using equation 2.1 [17,38,39]. Hermans orientation functions range from unity for perfect parallel orientation to zero for random orientation and to -0.5 for perpendicular orientation.

$$f_{c,x} = (3 < \cos^2 \Phi_{c,x} > - 1) / 2 \qquad (2.1)$$

where,

$$< \cos^2 \Phi_{c,x} > = 1 - 1.099 < \cos^2 \Phi_{110,x} > - 0.901 < \cos^2 \Phi_{040,x} > \qquad (2.2)$$

2.5 Raman spectroscopy

2.5.1 Instrumentation

The Raman systems used in this work were a *Renishaw system 100 (RA 100)* Raman spectrometer coupled to a remote Renishaw fiber optic probe, and a *Renishaw system 1000 (RM 1000)* microscope attached to a video camera. The *RM 1000* was used only in preliminary work. Both systems used a 500 mW diode laser, operating at 785 nm.

The *RA 100* system had a fiber optic probe connected to the diode laser and the spectrometer through optical fibers, which facilitated on-line measurement. A schematic representation of the Renishaw Raman probe is shown in Figure 2.8 [37]. The laser was

delivered by an optical fiber (50 µm core diameter, labeled excitation optical fiber in Figure 2.8) to the sample. The laser from the excitation optical fiber was collimated using a fiber launch lens, and then passed through a line filter to remove the Raman spectrum of the probe materials and any spurious lines emitted by the laser.

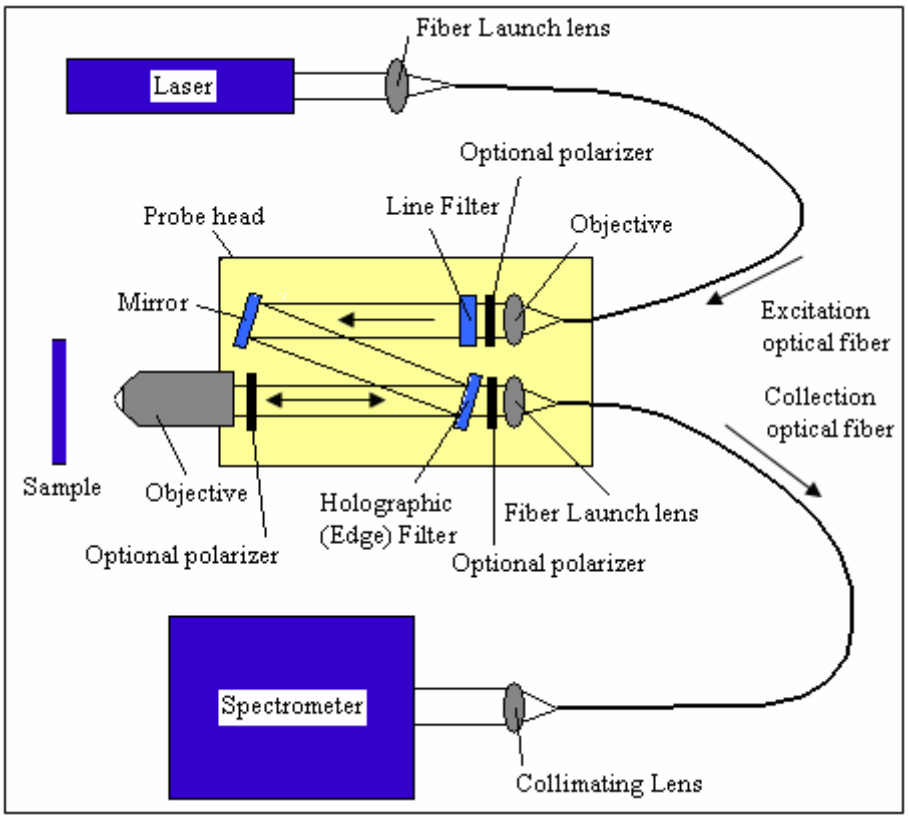

Figure 2.8 Schematic representation of a Renishaw Raman fiber optic probe

The probe head was equipped with an Olympus LM PlanFI 20X objective, which had a numerical aperture of 0.4 and an ultra long working distance (ULWD) of 1.2 cm. The objective performed the dual function of focusing the laser beam onto the sample, and collecting and collimating the backscattered light (scattered back 180°). The focused laser spot size was approximately 1.25 microns, which was calculated using the equation

2.3 [37], where d is the spot size of the laser, λ is the wavelength of the laser and NA is the numerical aperture of the probe objective.

$$d = \frac{0.61 * \lambda}{NA} \tag{2.3}$$

A holographic edge filter was used to separate the Raman backscatter from the counterpropagating laser light, and to block any Raleigh scattered light [48]. The Raman scattered light was collected and returned to a single slit, single grating stigmatic spectrograph through a collimating lens, for wavelength separation. This was done by a second optical fiber (62.5 μm core diameter, labeled collection optical fiber in Figure 2.8). For detection a two-dimensional, thermoelectrically cooled, deep depletion charge coupled device (CCD) camera was used.

Two types of Raman probes were used, one with a polarizer (polarized) and the other without a polarizer (non-polarized). The polarized Raman probe delivered laser radiation which was polarized in X direction and the backscattered radiation was also polarized in X direction. A schematic of the scattering geometry is shown in Figure 2.9 [48]. In this figure the scattering geometry is defined in laboratory coordinates where the incident laser propagates in the negative Z direction with polarization in X or Y direction. The scattered light travels in positive Z direction. An analyzing polarizer can be oriented to select only light polarized in the X direction or only in the Y direction (i.e., polarized either parallel or perpendicular to the incident light polarization).

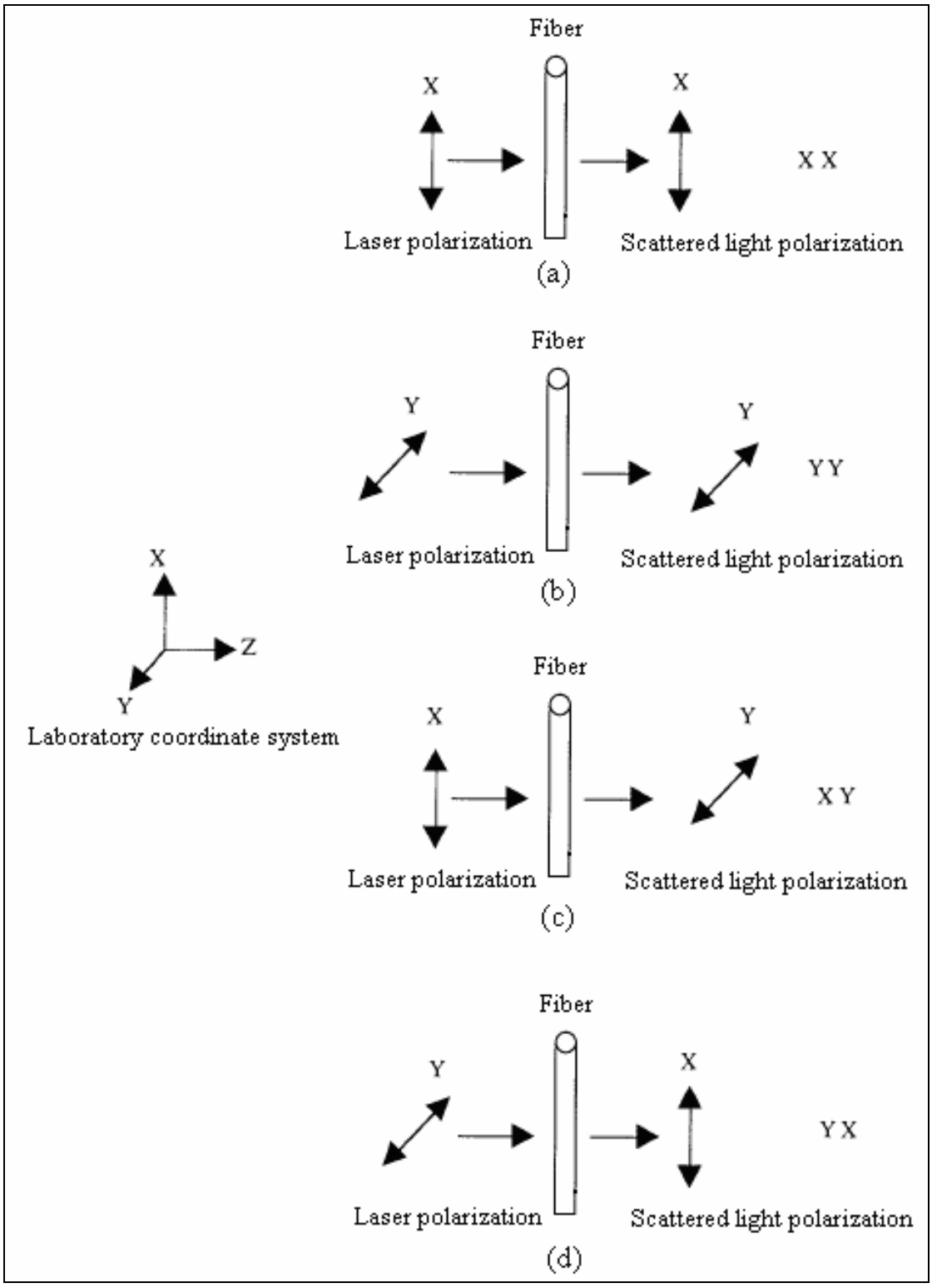

Figure 2.9 Scattering geometry in laboratory coordinates, (a) XX, (b) YY, (c) XY, and (d) YX

At maximum laser power, the polarized Raman probe delivered approximately 3 mW of laser radiation to the fiber sample, and the non-polarized Raman probe delivered approximately 8 mW of laser radiation to the fiber sample.

The *RM 1000* was attached to a *Sony* video camera for sample focusing. The sample stage was a XYZ stage from *Prior Scientific*. An electronic stepper motor was used to control X-Y positioning via a joystick controller. Z positioning was performed manually, using the adjusting knob. Two objectives from Olympus, 5X and 50X, were used on this system. This system also worked on the backscattering principle. The laser source propagated in the negative X direction and was polarized in Z direction. An additional polarizer was used to polarize the scattered radiation in the Z direction.

2.5.2 Calibration, focusing, and data collection

The spectrometers used in Raman spectroscopy need laser calibration, since different laser sources can be used for excitation. For the *RA 100*, calibration of the wavelength axis was performed both internally and externally to generate accurate Raman-shift spectra. In case of internal calibration, the spectrograph wavelength axis was calibrated using the *Renishaw* "WiRE v 1.3β" software and a neon light calibration source. External calibration was performed using a known Raman standard material (Cyclohexane) [1], to calibrate the wavelength axis. A 40 ml vial containing Cyclohexane (Fisher Scientific) and the non-polarized Raman probe were placed on the platform as shown in Figure 2.10. The distance between the probe and the vial was approximately 1-1.5 cm. The laser from the Raman probe was focused onto the vial and the Raman spectrum of Cyclohexane was collected, with a collection time of 10 seconds. The

spectrum collected was acquired in "static" mode, single scanned with 1200 lines/mm grating centered at 800 cm^{-1}. The spectral range employed was 500-1100 cm^{-1} with a spectral resolution of approximately 6 cm^{-1}/3 pixels. The 801 cm^{-1} band of cyclohexane was used for calibration.

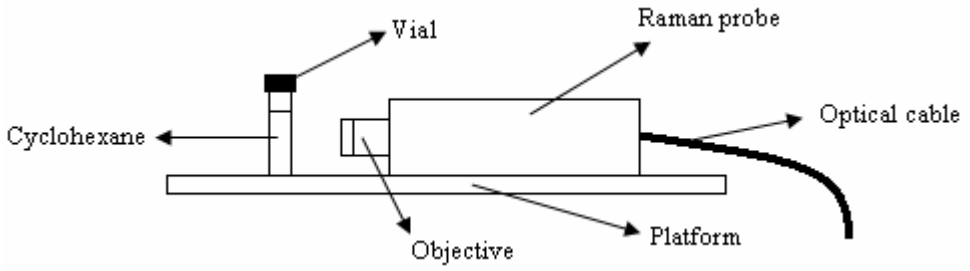

Figure 2.10 Setup for calibration using cyclohexane

For the *RM 1000*, silicon was used as the Raman standard material. A silicon calibration chip from *Renishaw Inc*. was placed on the sample platform. The video screen was enabled using *Renishaw* "WiRE v 1.3β" software. The microscope was focused using the 5X objective and the bright light source until a bright octagon appeared on the video screen. The objective was then changed to 50 X and the focus was adjusted until a bright octagon appeared again on the video screen. The source was switched from bright light to laser, and Raman spectrum was collected, using a collection time of 10 seconds. The spectrum collected was acquired in "static" mode, single scanned with 1800 lines/mm grating centered at 520 cm^{-1}. The spectral range employed was 200-800 cm^{-1} with a spectral resolution of approximately 2 cm^{-1}/3 pixels. The 520 cm^{-1} band of silicon was used for calibration.

For on-line data collection of fibers in the spinline, a Teflon coated 'Pig-tail' guide was used, as shown in Figure 2.11 (b), to consolidate the fibers into a bundle and to reduce vibration in the spinline. The guide was positioned such that no undue tension was placed on spinline. The Raman probe was fixed onto a metal block and the metal block was placed on the platform. The height of the metal block was designed such that the laser spot from the Raman probe and the x-ray beam from the collimator focused on the same spot along the spinline.

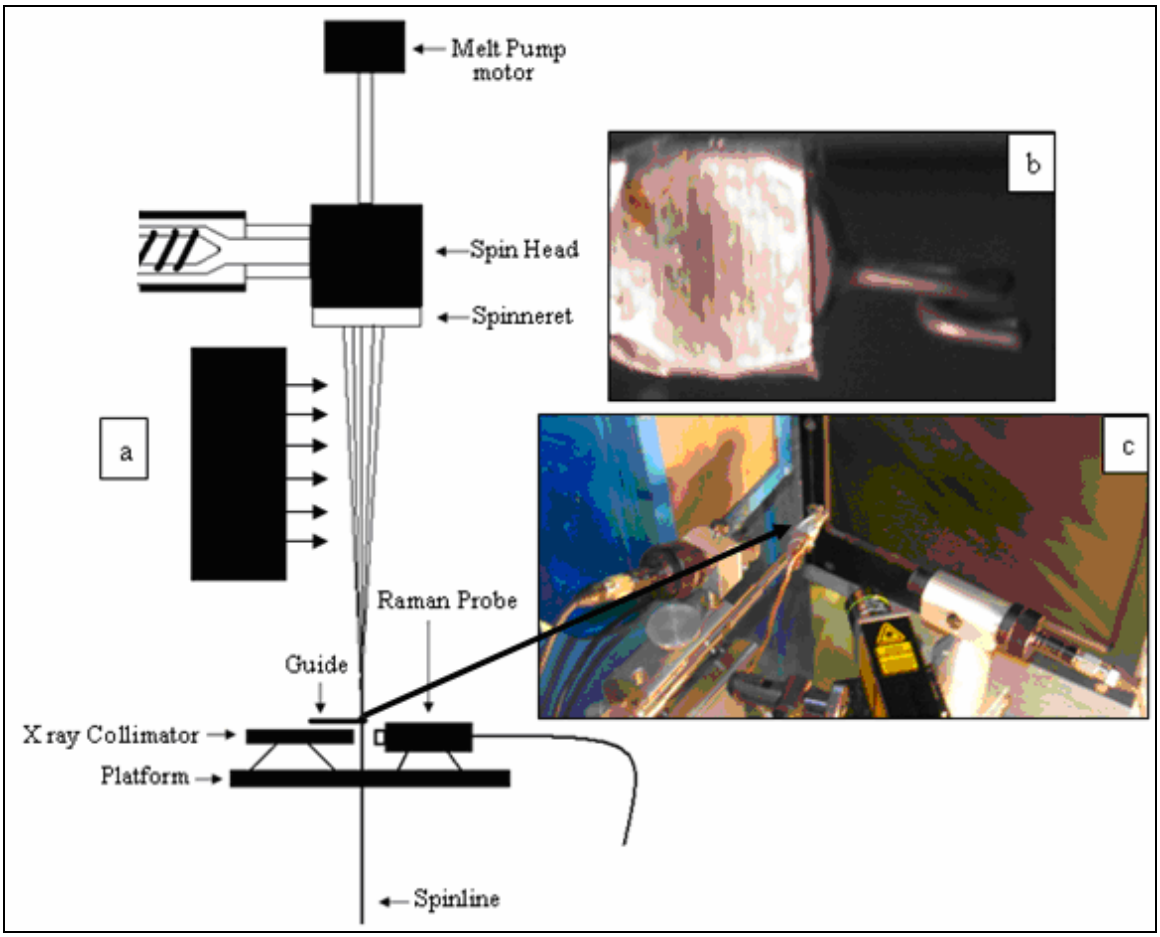

Figure 2.11 On-line sample positioning, (a) Schematic of on-line setup, (b) 'Pig-tail' guide, (c) On-line setup for data collection

Focusing of the laser onto the spinline was accomplished as follows. A piece of white paper was held on the opposite side of the spinline from the Raman probe. The Raman probe was placed approximately 1.2 cm from the spinline. The shadow cast from the spinline was observed on the piece of white paper background. As the probe was moved closer to the spinline, the shadow produced was found to become larger and then blurred, followed by the shadow becoming clearer and more distinct again and finally becoming smaller. The sharpest and most intense Raman spectra were obtained when the shadow was blurred. The data collection time was 120 seconds and at least five individual spectra were collected for one sample at each position along the spinline. The spectra collected were acquired in "static" mode, single scanned with 1200 lines/mm grating centered at 800 cm^{-1}. The spectral range employed was 500-1100 cm^{-1} with a spectral resolution of approximately 6 cm^{-1}/3 pixels.

The *RA 100* and *RM 1000* were both used for off-line data collection. An aluminum block was used to mount the as-spun fiber samples vertically in X direction for off-line measurements using the RA 100, as shown in Figure 2.12(b). Focusing and data collection was performed in a similar fashion as described earlier for the on-line fiber samples. For off-line measurements using the *RM 1000*, the as-spun fiber sample was mounted on an aluminum block, as shown in Figure 2.12 (a), and the block was placed on the sample platform so that the fiber sample was in Z direction. Focusing was done in the similar fashion as for the silicon calibration sample.

The spectra collected were acquired in "static" mode, single scanned with 1800 lines/mm grating centered at 800 cm^{-1}. The spectral range employed was 500-1100 cm^{-1} with a spectral resolution of approximately 2 cm^{-1}/3 pixels. The data collection time was

60 seconds for all off-line samples. A minimum of five separate fiber samples were selected and the Raman spectra were collected at three different positions along each fiber.

In all cases, data acquisition was performed using *Renishaw* "WiRE v 1.3β" software.

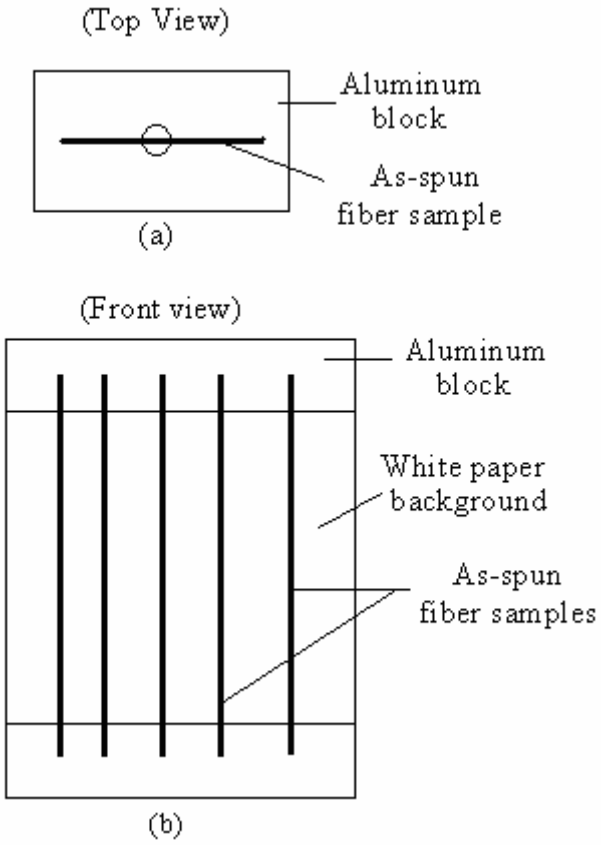

Figure 2.12 Off-line sample mounting for (a) *RM 1000* and (b) *RA 100*

2.5.3 Data analysis

All Raman spectra collected were processed using *GRAMS/32* (*Galactic Inc*, Salem, NH). All raw Raman spectra were smoothed using a binomial smoothing function, with a 3% degree of smoothing (*GRAMS/32* allows a degree of smoothing from

0-99%). A linear baseline was defined by selecting multiple points along each spectrum and the baseline was subtracted from each spectrum. Each spectrum was then curve fit using a mixed Gaussian-Lorentzian function (*GRAMS/32*). Two different curve fits were used in this study, a three-peak fit and a four-peak fit. The peaks were fit multiple times to ensure reproducibility of the fit. Once fit, the areas under the peaks of interest were recorded.

2.6 Differential scanning calorimetry (DSC) instrumentation

The DSC instrument used in this study was a *TA Q 1000* (*TA Instruments*). The sample mass used in all the experiments was between 3 and 3.5 mg. The off-line iPP fiber sample was placed in an aluminum pan (*TA Instruments*, T-060605, 900786.901) with a lid (*TA Instruments*, T-060531, 900779.901) and a *TA Instruments* sample press was used to press the sample inside the pan. This pan was equilibrated at 20 °C and then heated to 200 °C at a rate of 10 °C/min. Helium was purged at a rate of 20 mL/min for all the experiments, and at least three fiber samples were measured for each spinning condition.

Thermograms obtained from the experiments were analyzed using the *TA Universal Analysis 2000* software. The enthalpy of melting was determined by the analysis of thermograms and the percent crystallinity was calculated using the equation 2.4,

$$\% \text{ Crystallinity} = 100\% * (\Delta H_m - \Delta H_c) / \Delta H_m^0 \qquad (2.4)$$

where ΔH_m (J/g) is the enthalpy of fusion and ΔH_c (J/g) is the enthalpy of cold crystallization. The enthalpy of fusion for a pure 100% crystalline iPP, ΔH_m^0, was taken as 209 J/g [52] and the enthalpy of cold crystallization, ΔH_c was zero for all experiments.

2.7 Birefringence instrumentation

Birefringence was measured using two different techniques. The Mach Zehnder interference microscope was used to directly measure refractive indices of the fiber in the parallel (longitudinal) and perpendicular (transverse) directions, yielding retardation in terms of displacement. The transmitted light polarizing microscope, with a Berek compensator, was used to measure the optical path difference for light waves passing through the fiber, yielding retardation in terms of phase angle shift.

2.7.1 Mach Zehnder interference microscope

The Mach Zehnder interference microscope used in this study was *Aus Jena Jenapol U Interphako* supplied by the Martin Microscope Company, Easley, SC. The refractive indices of a polymer fiber in longitudinal ($n_{//}$) and transverse ($n_{\perp}$) direction with respect to the fiber axis are different because of the fiber's anisotropic nature. Direct measurement of these refractive indices provides a measure of birefringence in the polymer fiber.

The Mach Zehnder interference microscope consists of a white light source, two beam splitters, and two mirrors. The basic configuration of this microscope is shown in Figure 2.13 [40]. In this figure B represents a beam splitter and M represents a mirror. White light from the source first passes through the polarizer, and then is incident on B1.

The beam splitters used here are half silvered mirrors, which reflect half the light incident on them and refract the other half through them. The reflected light from B1 is reflected once again by M2, and finally refracted by the B2 before reaching the detector. The refracted light from the B1 is reflected twice, by M1 and B2, in that order, before reaching the detector.

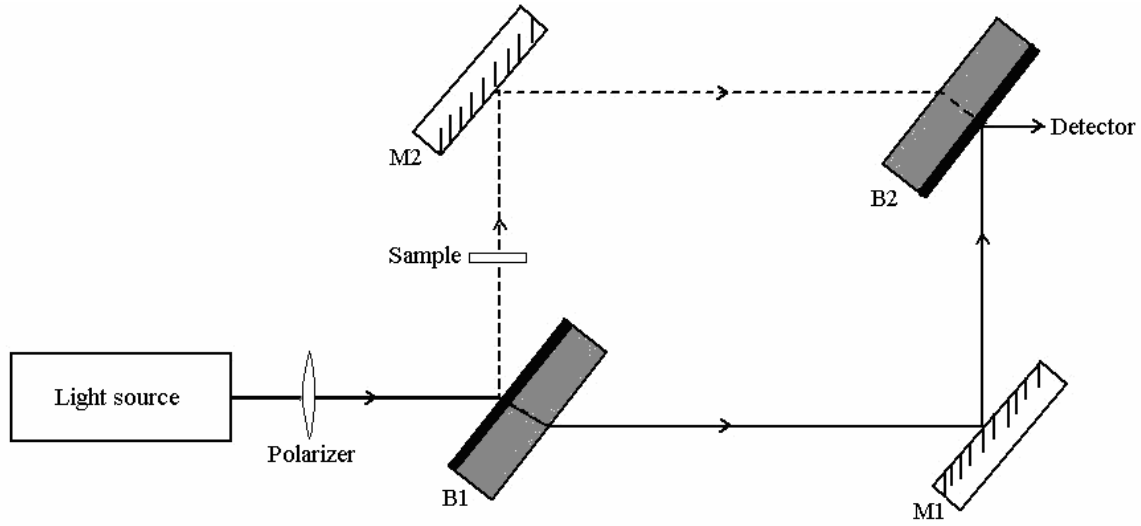

Figure 2.13 Basic configuration of Mach Zehnder interference microscope

In both paths the light is reflected twice and refracted once before reaching the detector, and hence both light waves are in phase. When a glass slide with standard refractive index oil is placed between B1 and M2 a phase shift occurs between the two light waves and this results in interference. The fiber whose birefringence was to be measured was placed on a 72 x 25 x 1 mm glass slide (VWR International, Cat No. 16004-422). A drop of refractive oil was placed on the fiber and then covered with an 18 mm sq. cover glass (Corning Labware and Equipment). The light source was polarized in the fiber direction for measuring longitudinal refractive index ($n_{//}$) of the fiber and in the

perpendicular direction to the fiber axis for measuring transverse ($n_{\perp}$) refractive index of the fiber. A schematic representation of a typical fringe pattern obtained is shown in Figure 2.14. The path of the dark fringe is deviated or displaced by the fiber.

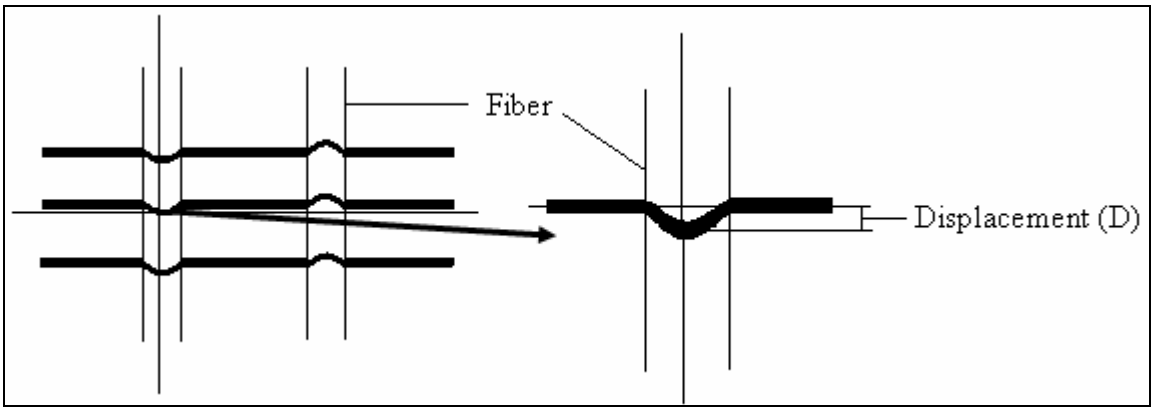

Figure 2.14 Interference fringe pattern (left) and its enlarged image (right) showing the displacement measurement

The displacement is measured as the distance between the center of the darkest fringe and the center of the deviated fringe as shown in Figure 2.14. This displacement gives a measure of the refractive index of the fiber in that direction. Oils with different refractive indices, whose value lies between the parallel ($n_{//}$ = 1.5215) [49] and perpendicular ($n_{\perp}$ = 1.492) [49] refractive indices of iPP fiber were evaluated and the one which produced a very good fringe pattern was selected for the birefringence measurement. The refractive index of the oil used was 1.494. The refractive index of the fiber in parallel and perpendicular direction was determined using equation 2.5,

$$n_{//} \text{ or } n_{\perp} = n_{oil} + (D/d) \qquad (2.5)$$

where

$n_{//}$ = refractive index of the fiber when light is polarized in fiber axis,

$n_{\perp}$ = refractive index of the fiber when light is polarized perpendicular to fiber axis,

n_{oil} = refractive index of the oil used (1.494),

D = displacement of dark fringe on the fiber (nm), and

d = diameter of the fiber (nm).

The diameter of the fiber was measured using the Image Analysis microscope with *Image Pro-Plus* software. At least three fiber samples for each spinning condition were measured. On each fiber sample, a minimum of five measurements were made at five different positions along the fiber sample. The birefringence was calculated using the equation 2.6

$$\Delta n = n_{//} - n_{\perp} \qquad (2.6)$$

where Δn is the birefringence, $n_{//}$ is the refractive index of the fiber in the longitudinal direction and $n_{\perp}$ is the refractive index of the fiber in the transverse direction with respect to the fiber axis.

2.7.2 Polarizing microscope with tilting compensator

The polarizing microscope used was an *Olympus BX60*. In this method birefringence was determined by measuring the optical path difference or retardation of light waves passing through the fiber.

The polarizer and analyzer were cross-polarized and then a single fiber placed on a 72 x 25 x 1 mm glass slide (VWR International, Cat No. 16004-422) was mounted on the platform of the microscope. The fiber was first oriented in the position of extinction, i.e., where the field of view becomes totally dark, and then the platform was rotated 45^0 to orient the fiber in the position of maximum brightness. The Berek compensator (Olympus) scale position was set to 30^0 before it was inserted. A schematic of the fringe pattern observed is shown in Figure 2.15. The compensator knob was rotated until the darkest fringe on the fiber intersected the center of the field of view, as shown in Figure 2.16. The tilting angle reading (θ_1) was noted at this point. Then the compensator knob was rotated in the opposite direction and the tilting angle reading (θ_2) was noted.

The measurement of tilting angles θ_1 and θ_2 was repeated several times and the mean value (θ) was calculated by using equation 2.7. After finding the mean value θ, the conversion table provided with the compensator was used to find the corresponding retardation for a given wavelength. In this study a green filter (Olympus) was used and the wavelength employed was 546.1 nm.

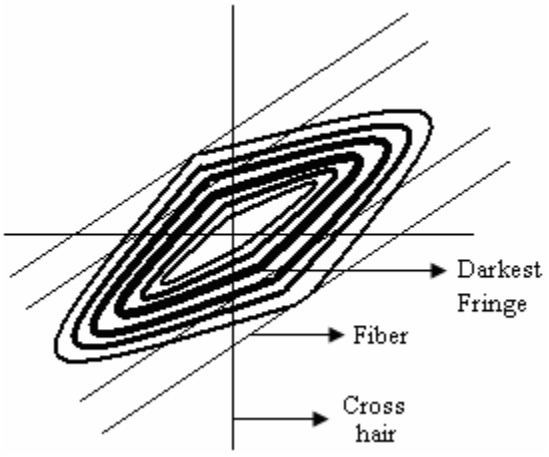

Figure 2.15 Schematic of fringe pattern using a tilting compensator

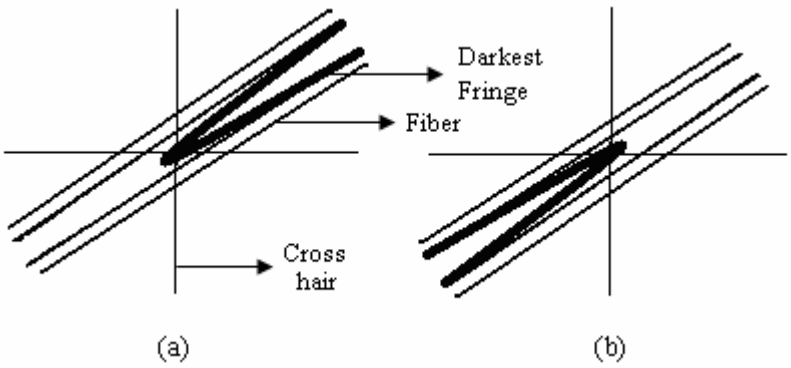

Figure 2.16 Measurement of tilt angles in two different directions, (a) and (b) of the compensator

$$\theta = \frac{|\theta_1 - \theta_2|}{2} \tag{2.7}$$

The diameter of the fiber was then measured using the Image Analysis microscope. At least three fiber samples for each spinning condition were measured. On each fiber sample, a minimum of five measurements were made at five different positions along the fiber sample. The birefringence was calculated using the equation 2.8,

$$\Delta n = \Gamma / t \tag{2.8}$$

where Δn is the birefringence, Γ is the retardation and t is the thickness or diameter of the fiber.

CHAPTER 3

RESULTS AND DISCUSSION

In this research, differential scanning calorimetry (DSC), wide angle x-ray diffraction (WAXD), and Raman spectroscopy were employed to estimate percent crystallinity in as-spun isotactic polypropylene (iPP) fibers. During melt spinning, WAXD and Raman spectroscopy were used simultaneously to estimate percent crystallinity at the same position along the spinline. For orientation measurements in as-spun iPP fibers, birefringence measurements, WAXD, and polarized Raman spectroscopy were employed. WAXD and polarized Raman spectroscopy were used simultaneously for on-line orientation measurements at the same position along the spinline during melt spinning. Based on previous research conducted in CAEFF fiber processing laboratory [26,46], two throughput rates and two take-up velocities were used to produce fiber samples at various drawdown ratios. The throughput rate calculations are presented in Appendix A.

In this chapter, the results obtained after analyzing the Raman spectra and WAXD patterns collected will be interpreted, along with DSC and birefringence results; the effect of polymer throughput rate and take-up velocity on percent crystallinity and orientation will be discussed; a comparison of DSC, WAXD, Raman, and birefringence results will be presented. In addition, some of the pertinent data collected from the preliminary work will be presented.

3.1 Off-line estimation of percent crystallinity

3.1.1 DSC

DSC measurement was done on all the as-spun fiber samples, and it served as a standard from which all other results were compared. Figure 3.1 is a typical DSC thermogram obtained for one of the fiber samples. The peak for the melting endotherm for all fiber samples was observed at approximately 162 °C. The area under the melting peak was determined and the percent crystallinity was calculated using equation 3.1,

$$\% \text{ Crystallinity} = 100\% * (\Delta H_m - \Delta H_c) / \Delta H_m^0 \qquad (3.1)$$

where ΔH_m (J/g) is the enthalpy of fusion and ΔH_c (J/g) is the enthalpy of cold crystallization. The enthalpy of fusion for a pure 100% crystalline iPP, ΔH_m^0, was taken as 209 J/g [52] and the enthalpy of cold crystallization, and ΔH_c was found to be zero for all fiber samples.

The percent crystallinities obtained for off-line fiber samples spun at different spinning conditions are presented in Table 3.1. Statistical hypothesis testing was performed for the comparison of the percent crystallinities for different drawdown ratios at a level of significance (α) of 0.05 (95% confidence interval). A statistical hypothesis test sample is presented in Appendix B and the analysis results are presented in Table 3.2.

It was observed that there was a statistical difference in percent crystallinity for different take-up velocities at same throughput rate at 95% confidence interval. For example, at a throughput rate of 0.89 g/min/hole, fibers spun at a take-up velocity of 400 m/min had 56% crystallinity compared to 60.3% for fibers spun at a take-up velocity of

800 m/min. This observation is in agreement with that of P. E. Lopes [26] and S. Varkol [46]. The average off-line DSC percent crystallinities were correlated to drawdown ratios and a good correlation was observed based on the R^2 value (0.93), as presented in Figure 3.2. The plot suggested that there was no linear correlation between the off-line DSC percent crystallinities and drawdown ratios, as observed by the value of the y intercept.

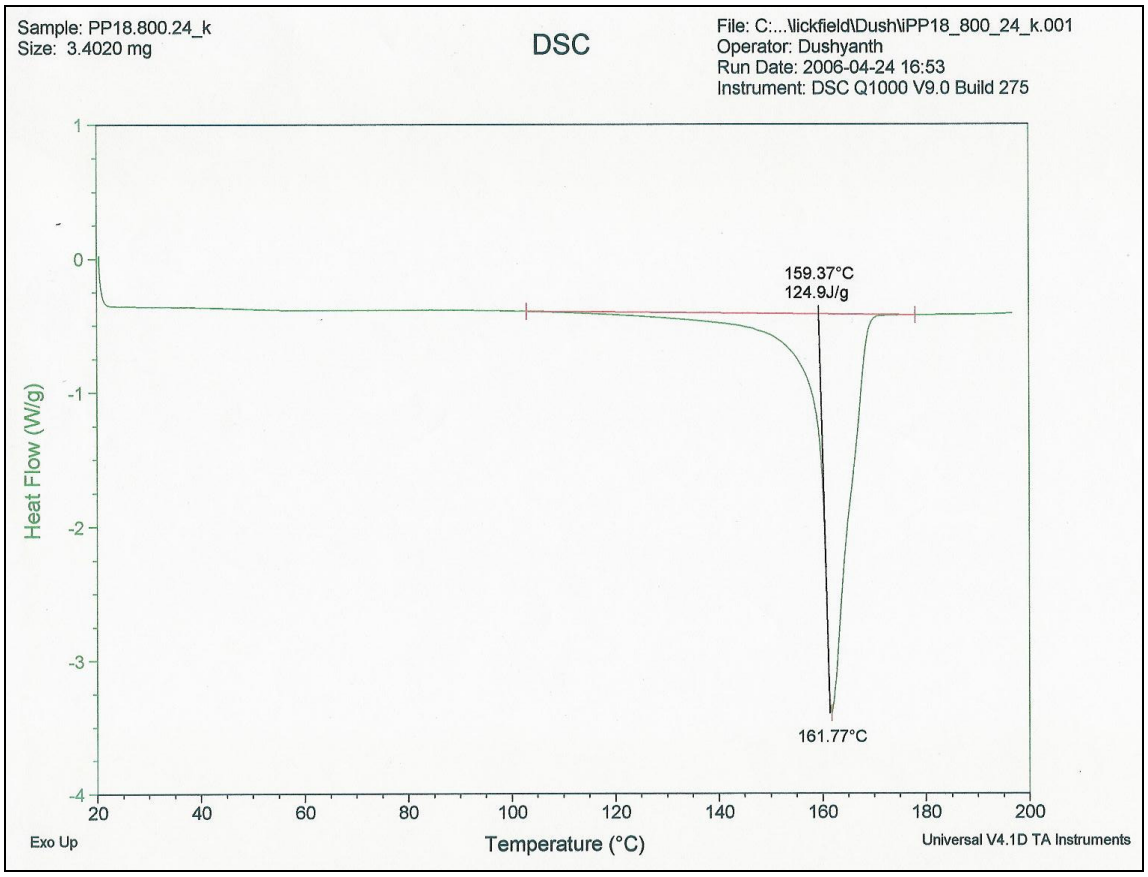

Figure 3.1 DSC thermogram for sample spun at 0.89 g/min/hole and 800 m/min

Table 3.1 Off-line percent crystallinities obtained from DSC measurements for different drawdown ratios

Take-up velocity (m/min)	**Throughput rate (g/min/hole)**	**Drawdown ratio (DDR)**	**Percent crystallinity (%)**
400	0.89	264	56.0 (1.5)
	0.67	353	56.3 (0.7)
800	0.89	529	60.3 (0.4)
	0.67	705	61.4 (0.9)

* Standard deviations from three measurements shown in parentheses

Table 3.2 Statistical analysis results for off-line percent crystallinities obtained from DSC measurements for different drawdown ratios

Drawdown ratio (DDR)	**Percent crystallinity (%)**	**Std. Dev.**	**t_{obs}**	**t_{crit} (95%)**	**Result**
264	56.0	1.5	0.31	2.45	FTR
353	56.3	0.7			
529	60.3	0.4	1.94	2.5	FTR
705	61.4	0.9			
353	56.3	0.7	7.74	2.18	R
705	61.4	0.9			
264	56.0	1.5	4.8	2.76	R
529	60.3	0.4			

* R = Reject null hypothesis (H_0), FTR = Fail to reject null hypothesis (H_0)

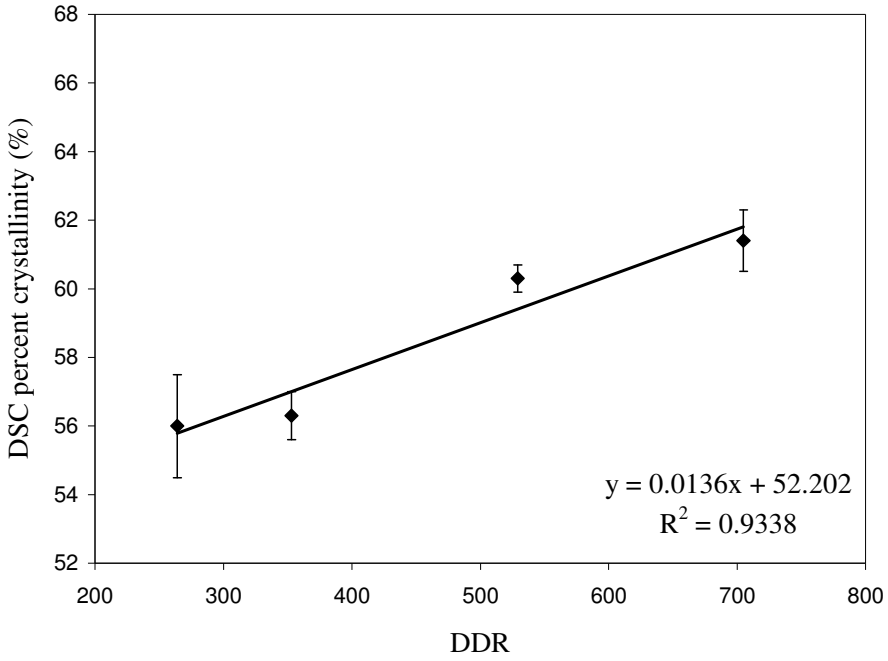

Figure 3.2 Linear correlation between DSC percent crystallinity and drawdown ratio

3.1.2 WAXD

Unprocessed WAXD patterns collected for off-line fiber samples spun at different drawdown ratios are presented in Figure 3.3, and the corresponding integrated intensity profiles are presented in Figure 3.4. The WAXD patterns obtained for drawdown ratios of 529 and 705 showed shorter diffraction rings compared to the ones obtained at drawdown ratios of 264 and 353. The integrated intensity profiles showed the three strong peaks located on the equator indexed (110), (040), and (130) reflections, suggesting the presence of α-form crystal, as discussed in the Introduction section (Chapter 1). A mixed Gaussian-Lorentzian curve fit for an integrated intensity profile is presented in Figure 3.5. Once the areas were determined the degree of crystallinity was calculated using equation 3.2 where I is the intensity or area under the peak and the subscript denotes the Miller indices for the crystallographic plane corresponding to the peak.

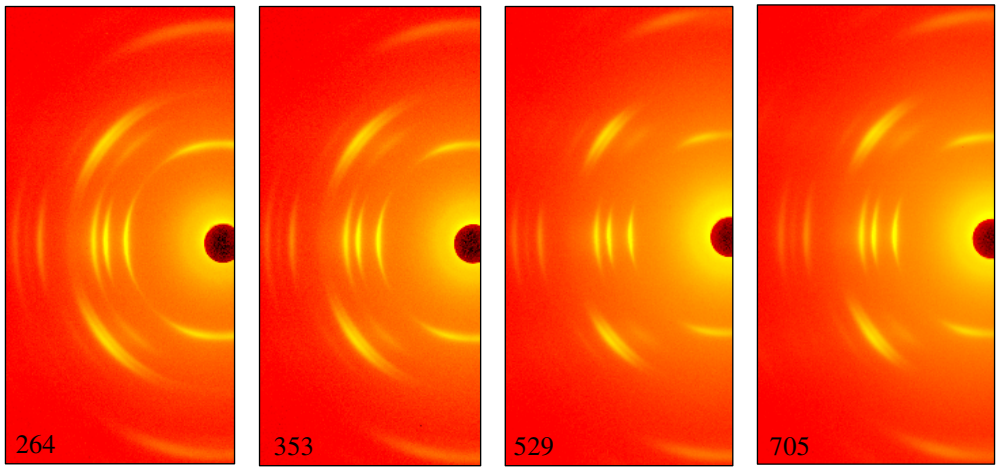

Figure 3.3 Off-line WAXD patterns for different drawdown ratios

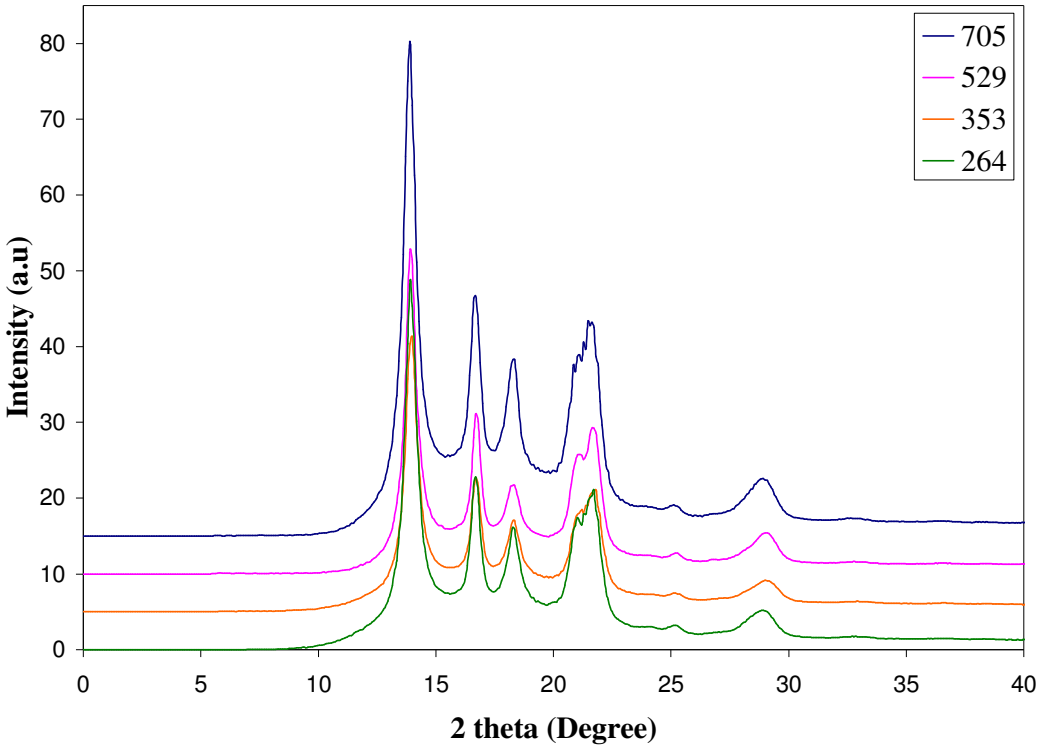

Figure 3.4 Off-line integrated intensity profiles for different drawdown ratios

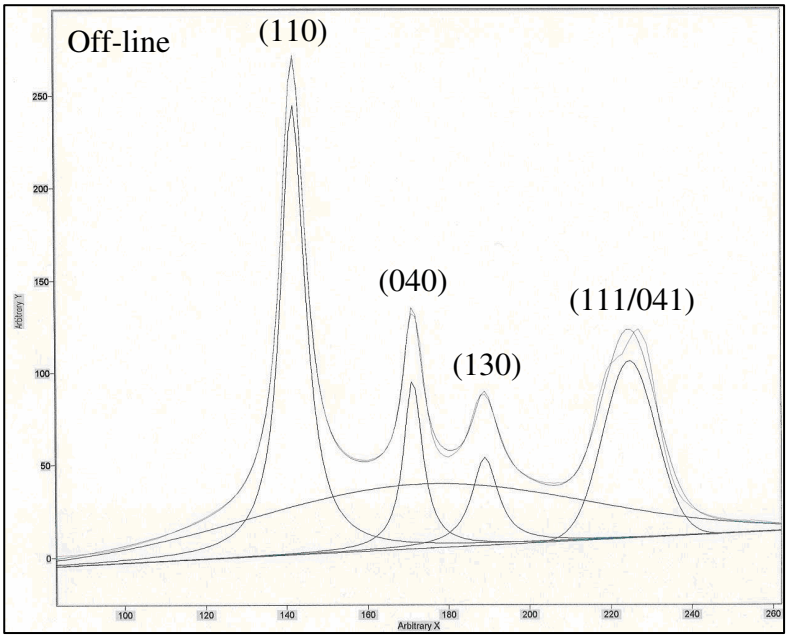

Figure 3.5 Mixed Lorentzian-Gaussian fit for the x-ray integration plot

$$\% \text{ Crystallinity} = 100\,\% * \frac{I_{(110)} + I_{(040)} + I_{(130)} + I_{(111/041)}}{I_{(110)} + I_{(040)} + I_{(130)} + I_{(111/041)} + I_{Halo}} \qquad (3.2)$$

The percent crystallinities obtained for off-line fiber samples spun at different spinning conditions are presented in Table 3.3. Statistical hypothesis testing was performed for the comparison of the percent crystallinities for different drawdown ratios at a level of significance (α) of 0.05 (95% confidence interval). The statistical analysis results are presented in Table 3.4.

It was observed that there was a statistical difference in percent crystallinity for different take-up velocities at a throughput rate of 0.89 g/min/hole. The fibers spun at a take-up velocity of 400 m/min had 57.9% crystallinity compared to 61.8% for fibers spun at a take-up velocity of 800 m/min. This observation is in agreement with Ran et al. [53].

At different throughput rates and same take-up velocity a statistical difference in percent crystallinity was observed only for 400 m/min.

Table 3.3 Off-line percent crystallinities obtained from WAXD for different drawdown ratios

Take-up velocity (m/min)	**Throughput rate (g/min/hole)**	**Drawdown ratio (DDR)**	**Percent crystallinity (%)**
400	0.89	264	57.9 (0.5)
	0.67	353	60.5 (0.5)
800	0.89	529	61.8 (0.7)
	0.67	705	64.6 (1.5)

* Standard deviations from two measurements shown in parentheses

Table 3.4 Statistical analysis results for off-line percent crystallinities obtained from WAXD measurements for different drawdown ratios

Drawdown ratio (DDR)	**Percent crystallinity (%)**	**Std. Dev.**	**t_{obs}**	**t_{crit} (95%)**	**Result**
264	57.9	0.5	5.2	2.92	R
353	60.5	0.5			
529	61.8	0.7	2.39	4.78	FTR
705	64.6	1.5			
353	60.5	0.5	3.67	5.56	FTR
705	64.6	1.5			
264	57.9	0.5	6.41	3.56	R
529	61.8	0.7			

* R = Reject null hypothesis (H_0), FTR = Fail to reject null hypothesis (H_0)

The average off-line WAXD percent crystallinities were correlated to drawdown ratios and a good correlation was observed based on the R^2 value (0.95), as presented in Figure 3.6. The plot suggested that there was no linear correlation between the off-line WAXD percent crystallinities and drawdown ratios, as observed by the value of the y

intercept. A slope test was conducted to compare the slopes of the lines of regression of WAXD with DSC, and no statistical difference was observed. A sample slope test calculation is presented in Appendix B. The average off-line WAXD percent crystallinities were also correlated to the average off-line DSC percent crystallinities, as presented in Figure 3.7, and again a reasonable correlation was observed based on the R^2 value (0.81). The plot suggested that there was no linear correlation between the off-line DSC and WAXD percent crystallinities, as observed by the value of the y intercept.

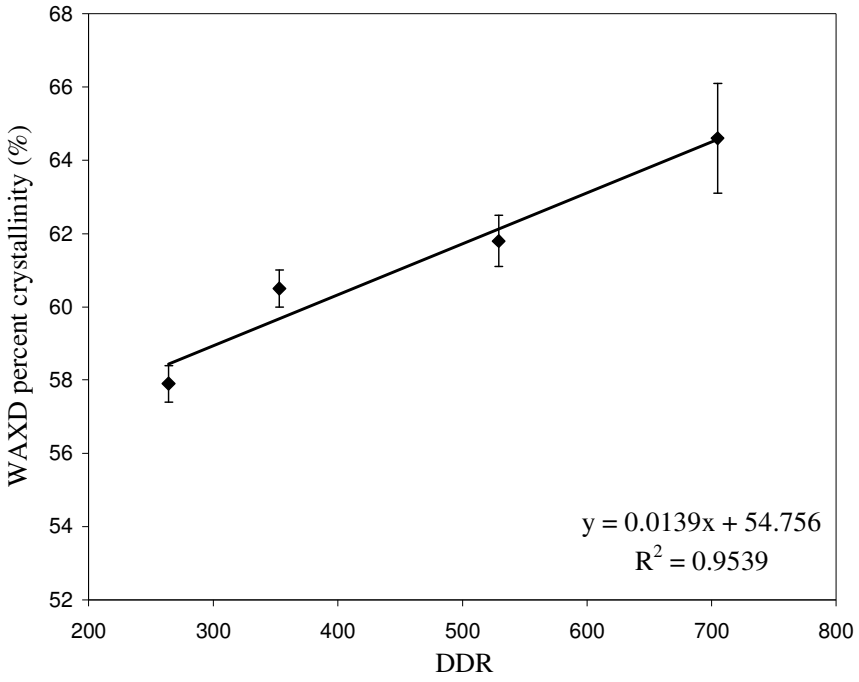

Figure 3.6 Linear correlation between off-line WAXD percent crystallinity and drawdown ratio

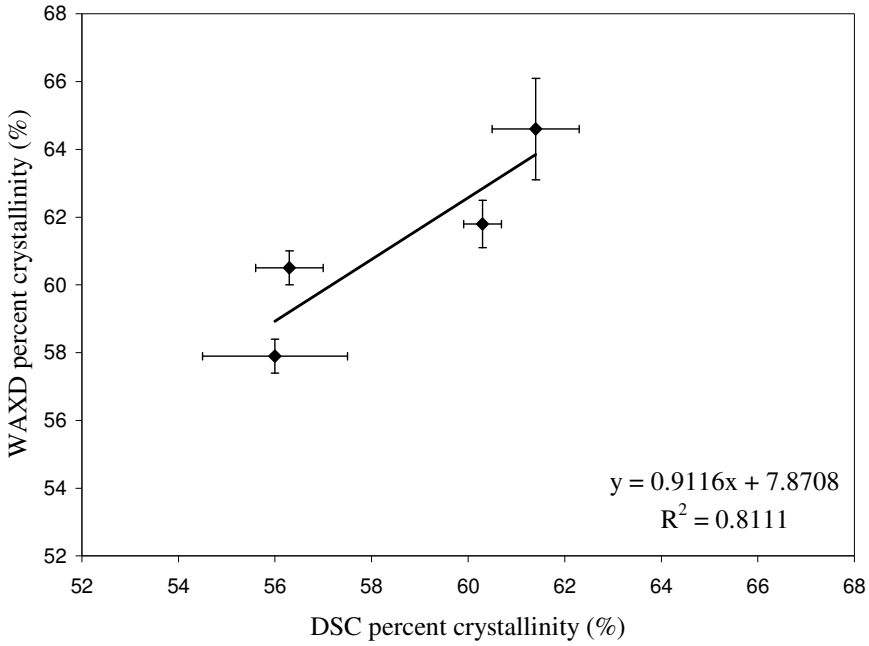

Figure 3.7 Linear correlation between off-line WAXD percent crystallinity and off-line DSC percent crystallinity

3.1.3 Raman spectroscopy

Raman spectra collected for off-line fiber samples spun at different drawdown ratios is presented in Figure 3.8. The spectra collected matched the typical Raman spectra for semi-crystalline iPP, as discussed previously in the Introduction section (Chapter 1). No difference was observed visually between the Raman spectra collected for off-line fiber samples spun at different drawdown ratios. Two types of curve fits were used, as discussed earlier in the Experimental section (Chapter 2): a three-peak curve fit developed by Neilsen et al. [9], and a four-peak curve fit developed by Minogianni et al. [13].

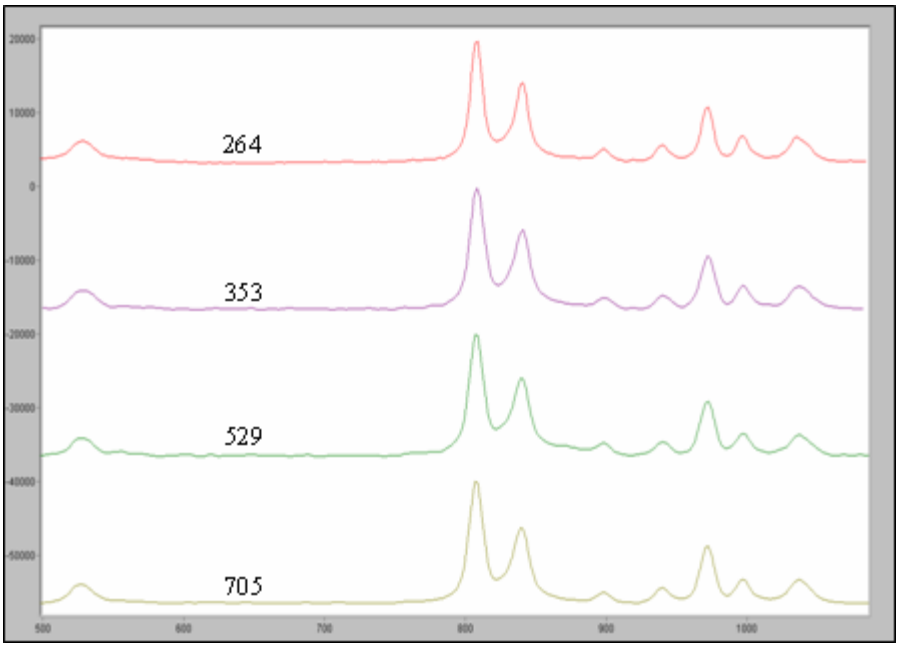

Figure 3.8 Off-line Raman spectra for different drawdown ratios

Using a three-peak curve fit, the areas under the peaks at 808, 830, and 841 cm^{-1} were determined and ratio of these peak areas was calculated using equation 3.3 [9], where I is the integrated intensity or the integrated area of the peak and the subscript denotes the position of the peak. An example of a mixed Gaussian-Lorentzian curve fitting for solid iPP using a three-peak fit is presented in Figure 3.9. Here the area of the peak at 808 cm^{-1} provides a measure of crystalline content in the material and the combined areas of peaks at 830 and 841 cm^{-1} provide a measure of amorphous content in the material.

$$\%\ \text{Raman three-peak ratio} = 100\,\% * \frac{I_{808}}{I_{808} + I_{830} + I_{841}} \qquad (3.3)$$

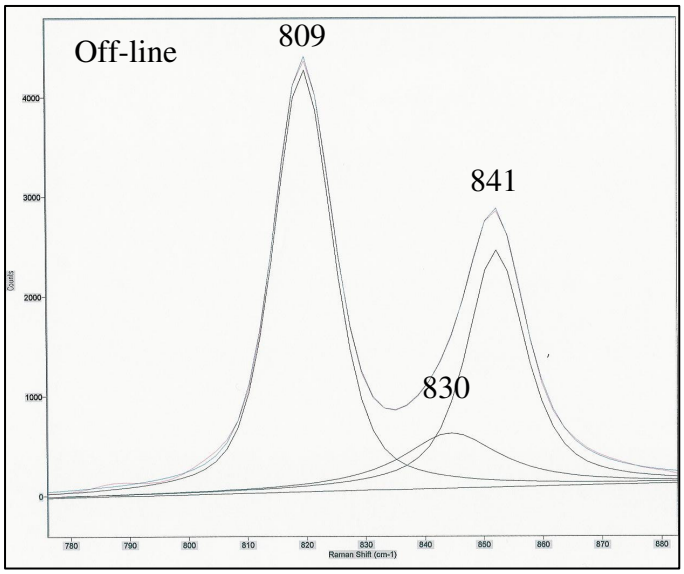

Figure 3.9 Mixed Gaussian-Lorentzian three-peak curve fit for offline iPP fiber spun at 400 m/min and 0.66g/m/hole

Using a four-peak curve fit, the areas under the peaks at 808, 830, 841, and 854 cm^{-1} were determined and ratio of these peak areas was calculated using equation 3.4 [13], where I is the integrated intensity or the integrated area of the peak and the subscript denotes the position of the peak. An example of a mixed Gaussian-Lorentzian curve fitting for solid iPP using a four-peak fit is presented in Figure 3.10. Here the area of the peak at 808 cm^{-1} provides a measure of crystalline content in the material and the combined areas of peaks at 830, 841, and 854 cm^{-1} provide a measure of amorphous content in the material.

$$\%\ \text{Raman three-peak ratio} = 100\,\% * \frac{I_{808}}{I_{808} + I_{830} + I_{841} + I_{854}} \qquad (3.4)$$

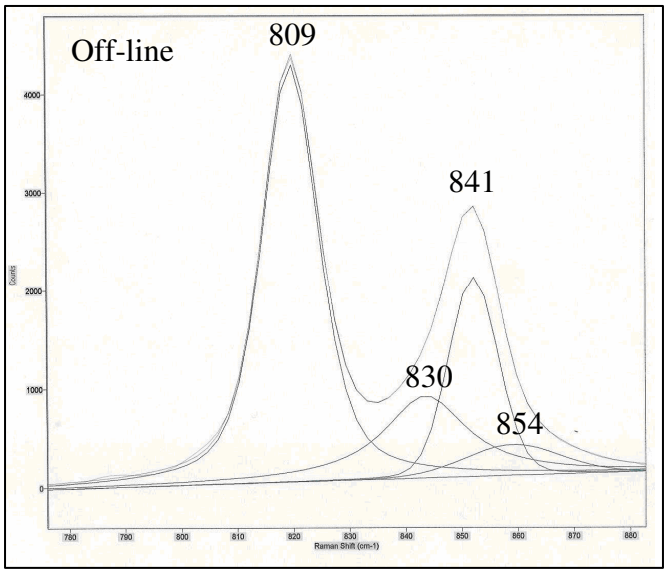

Figure 3.10 Mixed Gaussian-Lorentzian curve fit (Four peaks) for offline iPP fiber spun at 400 m/min and 0.66g/m/hole

The Raman peak ratios obtained for off-line fiber samples spun at different spinning conditions using a three-peak and four-peak fits are presented in Table 3.5. Statistical hypothesis testing was performed for the comparison of the off-line Raman peak ratios for different drawdown ratios at 95% confidence interval. The statistical analysis results are presented in Table 3.6 and Table 3.7.

Table 3.5 Off-line Raman peak ratios for different drawdown ratios

Take-up velocity (m/min)	**Throughput rate (g/min/hole)**	**Drawdown ratio (DDR)**	**Three-peak ratio (%)**	**Four-peak ratio (%)**
400	0.89	264	54.3 (0.7)	54.1 (1.3)
	0.67	353	55.2 (0.9)	55.0 (1.2)
800	0.89	529	56.7 (1.2)	57.3 (1.8)
	0.67	705	57.8 (1.3)	58.1 (1.6)

* Standard deviations from five measurements shown in parentheses

Table 3.6 Statistical analysis results for off-line Raman three-peak ratios obtained for different drawdown ratios

Drawdown ratio (DDR)	Percent crystallinity (%)	Std. Dev.	t_{obs}	t_{crit} (95%)	Result
264	54.3	0.7	1.76	1.88	FTR
353	55.2	0.9			
529	56.7	1.2	1.39	1.86	FTR
705	57.8	1.3			
353	55.2	0.9	3.67	1.89	R
705	57.8	1.3			
264	54.3	0.7	3.86	1.92	R
529	56.7	1.2			

* R = Reject null hypothesis (H_0), FTR = Fail to reject null hypothesis (H_0)

Table 3.7 Statistical analysis results for off-line Raman four-peak ratios obtained for different drawdown ratios

Drawdown ratio (DDR)	Percent crystallinity (%)	Std. Dev.	t_{obs}	t_{crit} (95%)	Result
264	54.1	1.3	1.14	1.86	FTR
353	55.0	1.2			
529	57.3	1.8	0.74	1.86	FTR
705	58.1	1.6			
353	55.0	1.2	3.47	1.88	R
705	58.1	1.6			
264	54.1	1.3	3.22	1.88	R
529	57.3	1.8			

* R = Reject null hypothesis (H_0), FTR = Fail to reject null hypothesis (H_0)

It was observed that there was a statistical difference in off-line Raman three-peak ratios for different take-up velocities at same throughput rate, at 95% confidence intervals. For example, at a throughput rate of 0.89 g/min/hole, fibers spun at a take-up velocity of 400 m/min had 54.3% peak ratio compared to 56.7% for fibers spun at a take-up velocity of 800 m/min. At different throughput rates and the same take-up velocity, no

statistical difference in Raman three-peak ratios was observed. Off-line Raman four-peak ratios for different take-up velocities at same throughput rate also showed a statistical difference at 95% confidence interval. For example, at a throughput rate of 0.89 g/min/hole, fibers spun at a take-up velocity of 400 m/min had 54.1% peak ratio compared to 57.3% for fibers spun at a take-up velocity of 800 m/min. At different throughput rates and the same take-up velocity, no significant difference in Raman four-peak ratios was observed. The off-line Raman peak ratios were correlated to drawdown ratios and a good correlation was observed based on R^2 values (top right hand corner for three-peak and bottom right hand corner for four-peak), as presented in Figure 3.11. The plot suggested that there was no linear correlation between the off-line Raman peak ratios and drawdown ratios, as observed by the value of the y intercept. A slope test was conducted to compare the slopes of the lines of regression of Raman (three-peak and four-peak) with DSC and WAXD, and no statistical difference was observed.

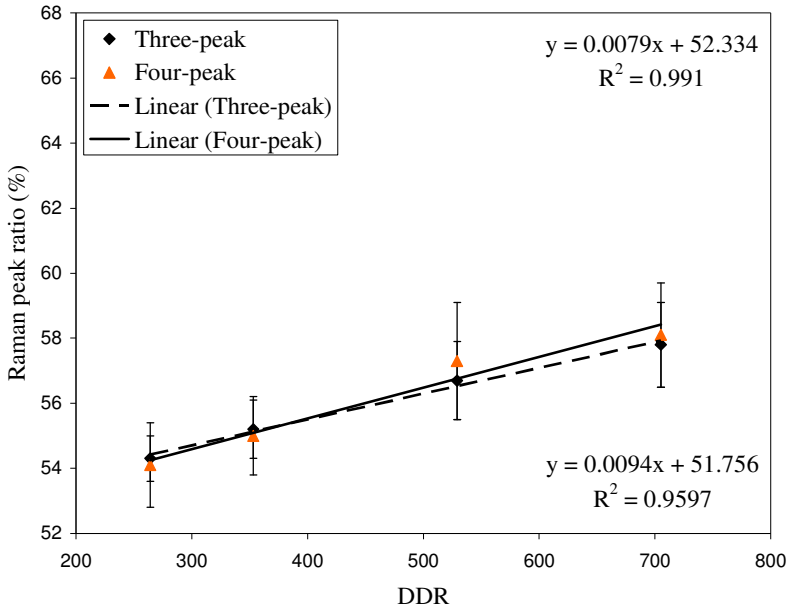

Figure 3.11 Linear correlation between off-line Raman peak ratio and drawdown ratio

Furthermore, the off-line Raman peak ratios were also correlated to off-line DSC and WAXD percent crystallinities, as presented in Figure 3.12 and 3.13 respectively, and a good correlation was observed based on R^2 values (top right hand corner for three-peak and bottom left hand corner for four-peak). The plots suggested that there was no linear correlation between the off-line DSC, WAXD percent crystallinities and Raman peak ratios, as observed by the value of the y intercept. The four-peak ratio showed a better correlation with DSC compared to the three-peak ratio, which is in agreement with Minogianni et al. [13]. The three-peak ratio showed a better correlation with WAXD compared to the four-peak ratio. Comparison of Raman three-peak and four-peak did not show a significant difference, which is not in agreement with the observations of Minogianni et al. [13]. The standard deviations from five measurements were higher for the Raman four-peak ratio compared to the three-peak ratio. A correlation plot of Raman three-peak and four-peak ratios is presented in Figure 3.14. The observed correlation was close to 1:1, suggesting no significant difference between the two methods.

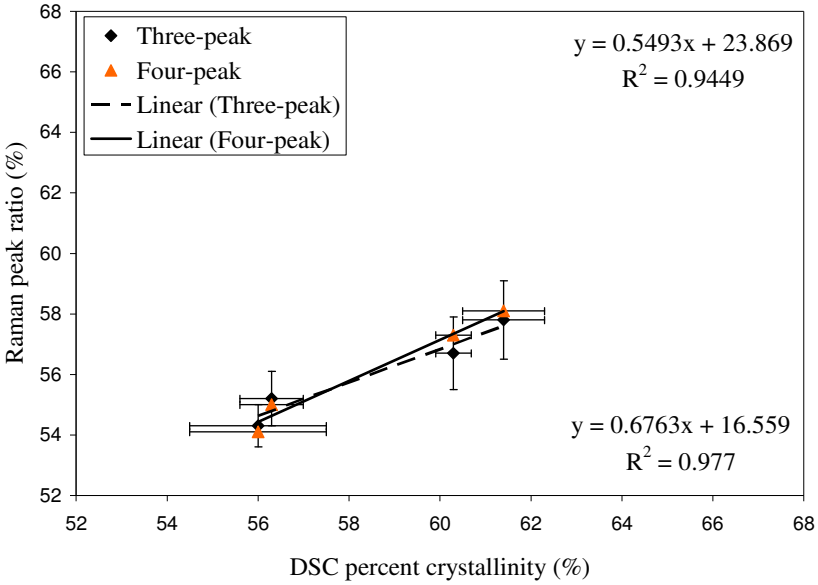

Figure 3.12 Linear correlation between off-line Raman peak ratio and DSC percent crystallinity

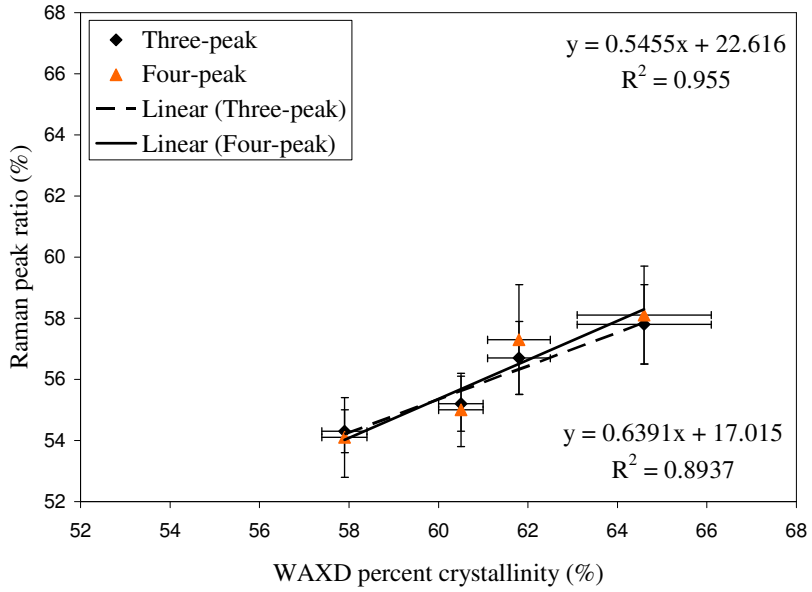

Figure 3.13 Linear correlation between off-line Raman peak ratio and WAXD percent crystallinity

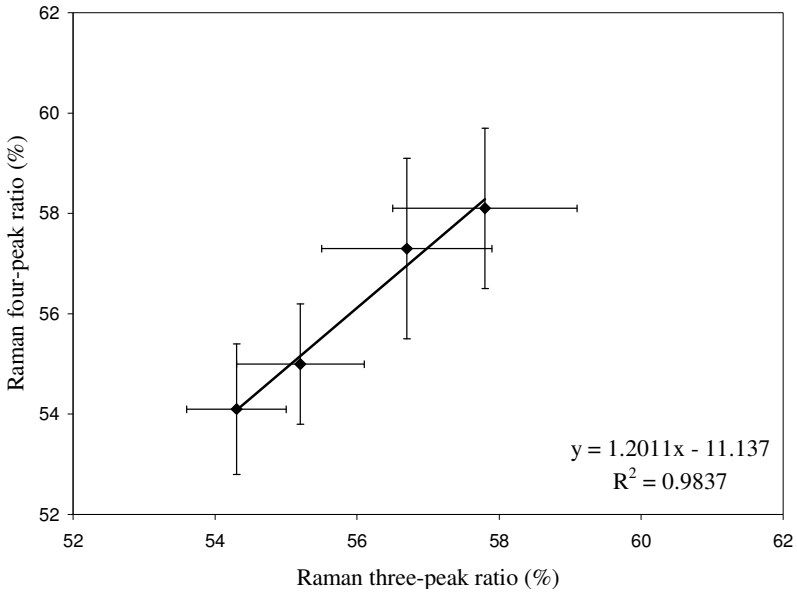

Figure 3.14 Linear correlation between off-line three-peak and four-peak Raman ratios

3.2 Off-line estimation of orientation

3.2.1 WAXD

Unprocessed WAXD patterns collected for off-line fiber samples spun at different drawdown ratios are previously presented in Figure 3.3. The WAXD patterns obtained for drawdown ratios of 529 and 705 showed shorter diffraction rings compared to the ones obtained at drawdown ratios of 264 and 353, suggesting higher orientation. The 'Hermans orientation factor (f)' was calculated using equations 3.5 and 3.6 as discussed previously in the Experimental section (Chapter 2). The Hermans orientation factor obtained for different drawdown ratios are presented in Table 3.8. Statistical hypothesis testing was performed for the comparison of the off-line Hermans orientation factors for different drawdown ratios at 95% confidence interval. The statistical analysis results are presented in Table 3.9.

$$f_{c,x} = (3 < \cos^2 \Phi_{c,x} > - 1) / 2 \quad (3.5)$$

where,

$$< \cos^2 \Phi_{c,x} > = 1 - 1.099 < \cos^2 \Phi_{110,x} > - 0.901 < \cos^2 \Phi_{040,x} > \quad (3.6)$$

Table 3.8 Off-line Hermans orientation factors obtained from WAXD for different drawdown ratios

Take-up velocity (m/min)	**Throughput rate (g/min/hole)**	**Drawdown ratio (DDR)**	**Hermans orientation factor (f)**
400	0.89	264	0.54 (0.01)
	0.67	353	0.57 (0.02)
800	0.89	529	0.59 (0.01)
	0.67	705	0.61 (0.01)

* Standard deviations from two measurements shown in parentheses

Table 3.9 Statistical analysis results for off-line Hermans orientation factor obtained from WAXD measurements for different drawdown ratios

Drawdown ratio (DDR)	**Hermans orientation factor (f)**	**Std. Dev.**	**t_{obs}**	**t_{crit} (95%)**	**Result**
264	0.54	0.01	1.90	4.72	FTR
353	0.57	0.02			
529	0.59	0.01	2.00	2.92	FTR
705	0.61	0.01			
353	0.57	0.02	2.53	4.72	FTR
705	0.61	0.01			
264	0.54	0.01	5.00	2.92	R
529	0.59	0.01			

* R = Reject null hypothesis (H_0), FTR = Fail to reject null hypothesis (H_0)

It was observed that there was a statistical difference in Hermans orientation factor for different take-up velocities only at a throughput rate of 0.89 g/min/hole. Fibers

spun at 400 m/min had a Hermans orientation factor of 0.54 compared to 0.59 for fibers spun at 800 m/min. At different throughput rates and the same take-up velocity a no statistical difference in Hermans orientation factor was observed. The off-line Hermans orientation factor for throughput rate of 0.89 g/min/hole at 400 m/min was compared with off-line Hermans orientation factor in P. E. Lopes' work [26] for the same spinning condition, and a close agreement was observed. P. E. Lopes obtained 0.52 compared to 0.54 observed in this work. The Hermans orientation factor values were correlated to drawdown ratios and a good correlation was observed based on R^2 value, as presented in Figure 3.15. The plot suggested that there was no linear correlation between the off-line Hermans orientation factors and drawdown ratios, as observed by the value of the y intercept. This observation is also in agreement with the work of P. E. Lopes [26].

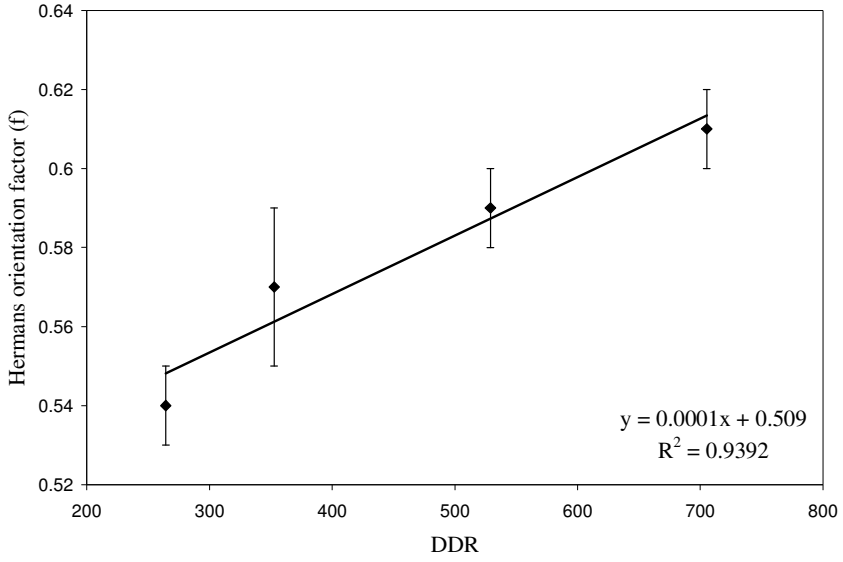

Figure 3.15 Linear correlation between off-line Hermans orientation factor and drawdown ratio

3.2.2 Birefringence

Birefringence measurements were done on all as-spun fiber samples using two methods, as explained in the Experimental section (Chapter 2). One method used the refractive index oil to directly measure the birefringence in fibers, and the other method used a tilting compensator to measure the retardation in fibers. The birefringence values obtained for different drawdown ratios are presented in Table 3.10. Statistical hypothesis testing was performed for the comparison of the off-line birefringence for different drawdown ratios at 95% confidence interval. The statistical analysis results are presented in Table 3.11 and 3.12.

Table 3.10 Off-line birefringence measurements for different drawdown ratios

Take-up velocity (m/min)	**Throughput rate (g/min/hole)**	**Drawdown ratio (DDR)**	**Birefringence (Oil)**	**Birefringence (Compensator)**
400	0.89	264	16.6 (0.5)	18.1 (1.5)
	0.67	353	19.3 (0.4)	19.3 (1.2)
800	0.89	529	22.7 (0.6)	22.7 (0.6)
	0.67	705	22.8 (0.6)	22.7 (0.4)

* Standard deviations from ten measurements shown in parentheses

Table 3.11 Statistical analysis results for off-line birefringence obtained using Mach Zehnder interference microscope for different drawdown ratios

Drawdown ratio (DDR)	Birefringence (Oil)	Std. Dev.	t_{obs}	t_{crit} (95%)	Result
264	16.6	0.5	13.33	1.73	R
353	19.3	0.4			
529	22.7	0.6	0.37	1.73	FTR
705	22.8	0.6			
353	19.3	0.4	15.35	1.74	R
705	22.8	0.6			
264	16.6	0.5	24.70	1.73	R
529	22.7	0.6			

* R = Reject null hypothesis (H_0), FTR = Fail to reject null hypothesis (H_0)

Table 3.12 Statistical analysis results for off-line birefringence obtained using tilting compensator for different drawdown ratios

Drawdown ratio (DDR)	Birefringence (Compensator)	Std. Dev.	t_{obs}	t_{crit} (95%)	Result
264	18.1	1.5	1.97	1.73	R
353	19.3	1.2			
529	22.7	0.6	0.0	1.74	FTR
705	22.7	0.4			
353	19.3	1.2	8.50	1.77	R
705	22.7	0.4			
264	18.1	1.5	9.00	1.78	R
529	22.7	0.6			

* R = Reject null hypothesis (H_0), FTR = Fail to reject null hypothesis (H_0)

It was observed that there was a statistical difference in birefringence for different take-up velocities at the same throughput rate. For example, at a throughput rate of 0.89 g/min/hole, fibers spun at 400 m/min had a birefringence of 16.6 (oil) and 18.1 (compensator) compared to 22.7 (both oil and compensator) for fibers spun at 800 m/min. At different throughput rates and same take-up velocity a statistical difference in birefringence was observed for 400 m/min only. The birefringence values were correlated

to drawdown ratios and a good correlation was observed based on R^2 values (top left hand corner for oil and bottom right hand corner for compensator), as presented in Figure 3.16. This is in agreement with previous work [14,24,46]. The plot suggested that there was no linear correlation between the off-line birefringence values and drawdown ratios, as observed by the value of the y intercept. The off-line birefringence values for fibers spun under similar spinning conditions observed by S. Varkol [46] were lower than the ones observed in this work, which may be due to the fact that the polymer used in this work has a lower melt flow index (18 MFI) compared to the ones used in S. Varkol's work (35 and 400 MFI). Lower molecular weight polymer chains relax faster when compared to the higher molecular weight polymer chains. Both the refractive index oil method and the compensator method showed similar correlation with drawdown ratio.

Furthermore, the birefringence values were also correlated to Hermans orientation factor, as presented in Figure 3.17, and a good correlation was observed based on R^2 value (top left hand corner for oil and bottom right hand corner for compensator). The refractive index oil method had a better correlation with the Hermans orientation factor compared to the compensator method. The plot suggested that there was no linear correlation between the off-line Hermans orientation factors and birefringence values, as observed by the value of the y intercept. Birefringence obtained from both the methods was correlated and a good correlation was observed based on R^2 value (0.97), as presented in Figure 3.18. For the compensator method the standard deviations from ten measurements were higher for fibers spun at lower drawdown ratios due to the reason that the darkest fringe observed for these fibers were not clear, resulting in more error in measurement. A slope test was conducted to compare the slopes of the lines of regression

of Birefringence (oil and compensator) with Hermans orientation factor, and a statistical difference was observed. This indicates that birefringence was more sensitive to drawdown ratio compared to Hermans orientation factor. When the slopes for birefringence (oil and compensator) were compared, no statistical difference was observed.

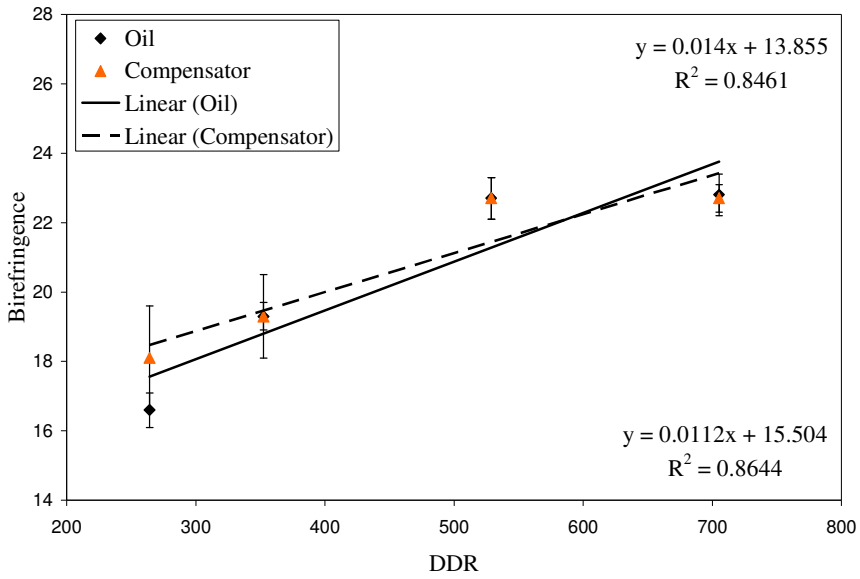

Figure 3.16 Linear correlation between off-line birefringence and drawdown ratio

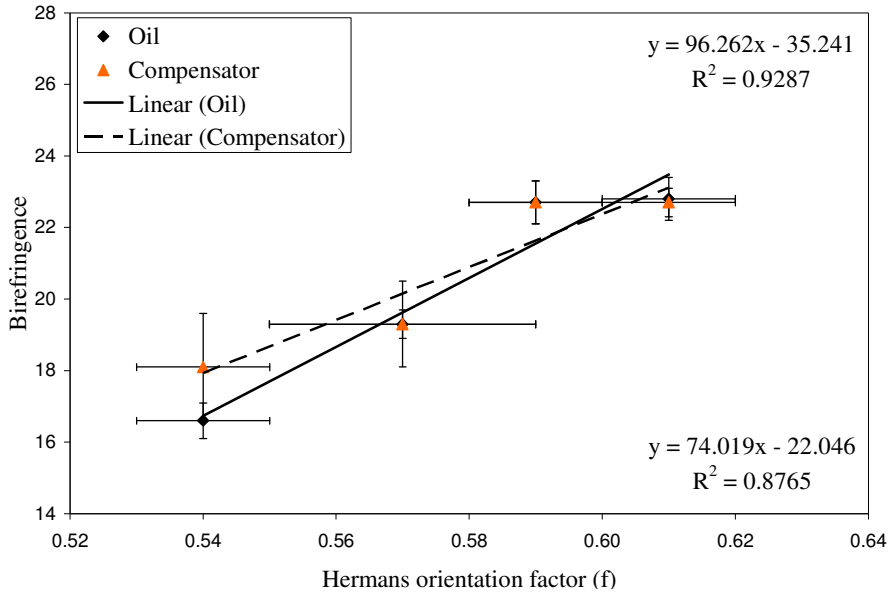

Figure 3.17 Linear correlation between off-line birefringence and off-line Hermans orientation factor

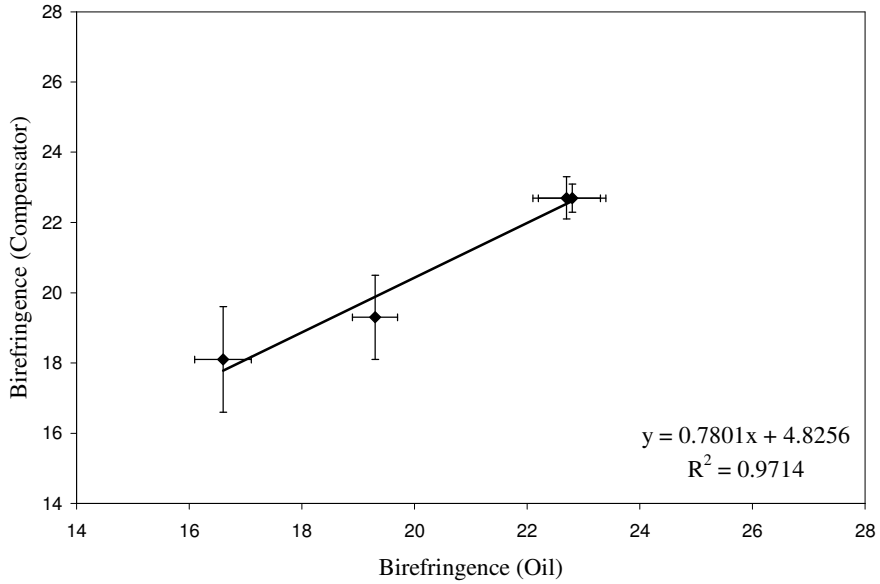

Figure 3.18 Linear correlation between off-line birefringences (oil and compensator)

3.2.3 Polarized Raman spectroscopy

Polarized Raman spectra were collected for all as-spun fiber samples. The spectra collected matched the typical polarized Raman spectra for semi-crystalline iPP. Comparison of off-line spectra for different drawdown ratios is presented in Figure 3.19. The appearance of 998 cm^{-1} band suggested the presence of α-form crystal [15], which was in agreement of WAXD off-line results discussed previously in this chapter. The areas under the peaks at 808 and 841 cm^{-1} were determined, and the ratio of areas of 808 to 841 cm^{-1} was calculated. The polarized Raman peak ratios for different drawdown ratios are presented in Table 3.13. Statistical hypothesis testing was performed for the comparison of the off-line polarized Raman peak ratios for different drawdown ratios at 95% confidence interval. The statistical analysis results are presented in Table 3.14.

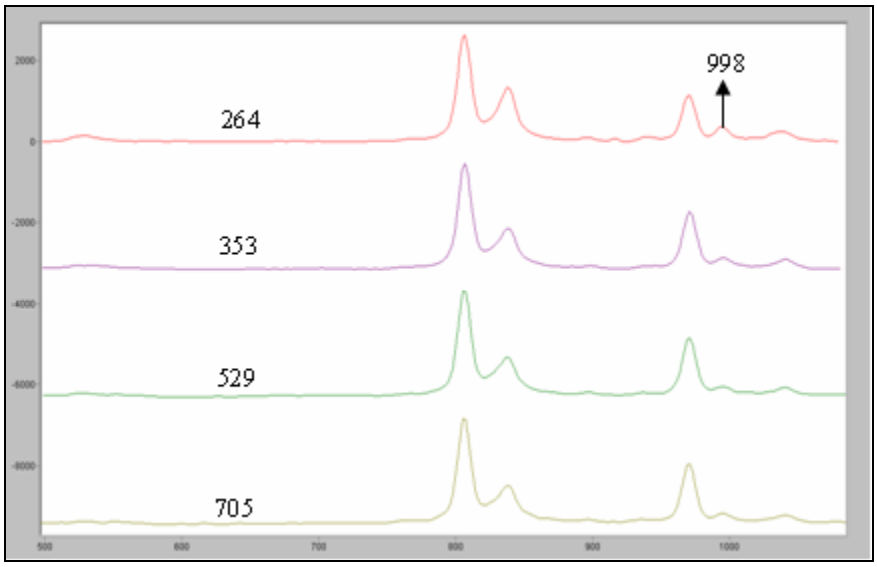

Figure 3.19 Comparison of off-line polarized Raman spectra for different drawdown ratios

Table 3.13 Off-line polarized Raman peak ratios for different drawdown ratios

Take-up velocity (m/min)	Throughput rate (g/min/hole)	Drawdown ratio (DDR)	Polarized Raman peak ratio
400	0.89	264	1.44 (0.08)
	0.67	353	1.58 (0.05)
800	0.89	529	1.66 (0.05)
	0.67	705	1.7 (0.03)

* Standard deviations from five measurements shown in parentheses

Table 3.14 Statistical analysis results for off-line Raman four-peak ratios obtained for different drawdown ratios

Drawdown ratio (DDR)	Polarized Raman peak ratio	Std. Dev.	t_{obs}	t_{crit} (95%)	Result
264	1.44	0.08	3.32	1.90	R
353	1.58	0.05			
529	1.66	0.05	1.53	1.92	FTR
705	1.70	0.03			
353	1.58	0.05	4.60	1.92	R
705	1.70	0.03			
264	1.44	0.08	5.21	1.90	R
529	1.66	0.05			

* R = Reject null hypothesis (H_0), FTR = Fail to reject null hypothesis (H_0)

It was observed that there was a statistical difference in polarized Raman peak ratio for different take-up velocities at the same throughput rate, at 95% confidence interval. For example, at a throughput rate of 0.89 g/min/hole, fibers spun at 400 m/min had a polarized peak ratio of 1.44 compared to 1.66 for fibers spun at 800 m/min. For different throughput rates at the same take-up velocity a statistical difference was observed only at a take-up velocity of 400 m/min. Fibers spun at 0.89 g/min/hole had a polarized peak ratio of 1.44 compared to 1.58 for fibers spun at 0.67 g/min/hole. The

polarized Raman peak ratios were correlated to drawdown ratios and a good correlation was observed based on R^2 value (0.85), as presented in Figure 3.20. This observation is in line with previous work of Paradkar et al. [14] and Ran et al. [15]. The plot suggested that there was no linear correlation between the off-line polarized Raman peak ratios and drawdown ratios, as observed by the value of the y intercept. A slope test was conducted to compare the slopes of the lines of regression of polarized Raman with Birefringence (oil and compensator) and Hermans orientation factor. A statistical difference was observed between the slopes only for polarized Raman and birefringence, and not for polarized Raman and Hermans orientation factor, suggesting that birefringence was more sensitive to drawdown ratio compared to Hermans orientation factor or polarized Raman peak ratio.

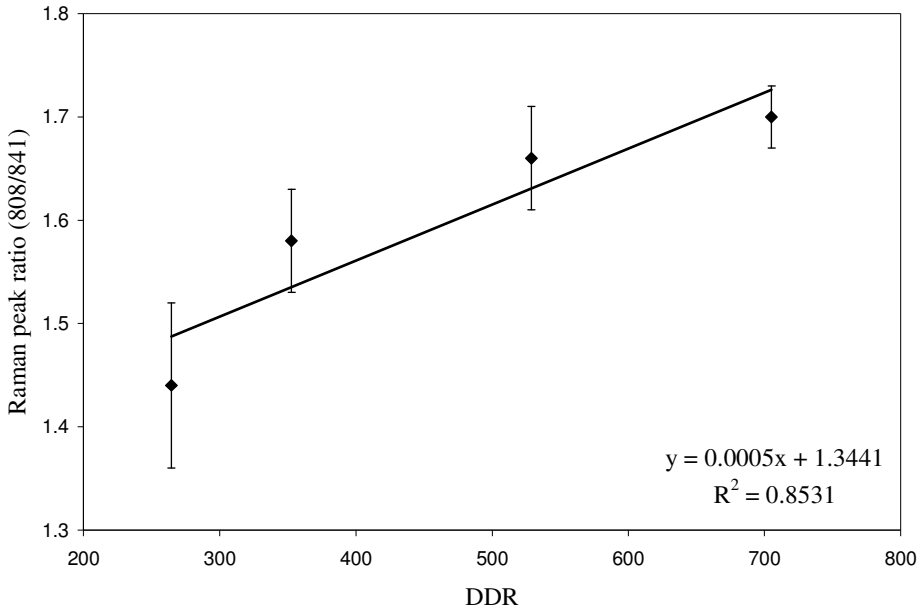

Figure 3.20 Linear correlation between off-line polarized Raman peak ratio and drawdown ratio

Furthermore, the polarized Raman peak ratios were also correlated to Hermans orientation factor, birefringence (using both the method), as presented in Figure 3.21 and 3.22 respectively. A good correlation was observed based on R^2 value (top left hand corner for oil and bottom right hand corner for compensator). The polarized Raman peak ratio had better correlation with Hermans orientation factor and birefringence (oil) compared to that with birefringence (compensator). The plots suggested that there was no linear correlation between the off-line Hermans orientation factors, birefringence values, and polarized Raman peak ratios, as observed by the value of the y intercept.

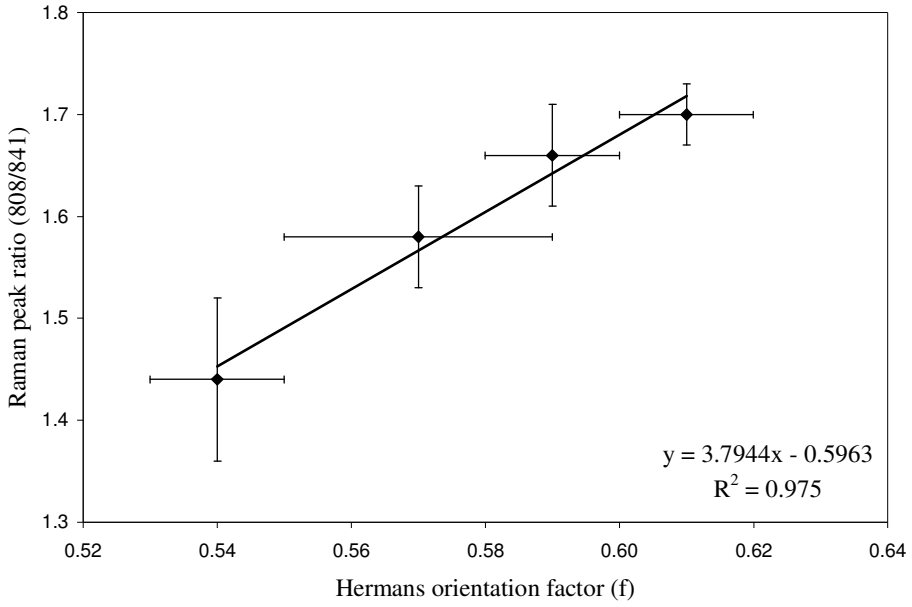

Figure 3.21 Linear correlation between off-line polarized Raman peak ratio and off-line Hermans orientation factor

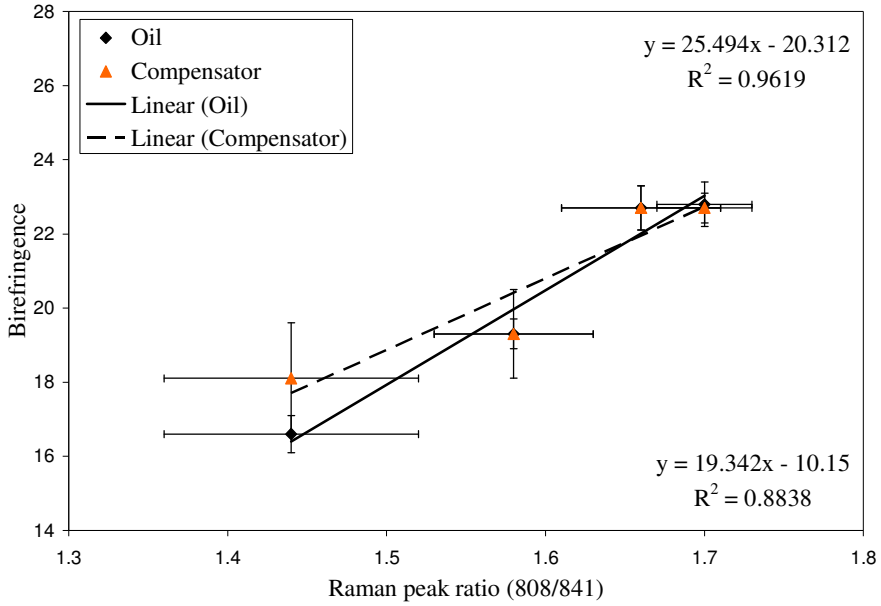

Figure 3.22 Linear correlation between off-line polarized Raman peak ratio and off-line birefringence (oil)

3.3 Estimation of percent crystallinity along the spinline

3.3.1 WAXD

The on-line WAXD images collected along the spinline for one of the spinning conditions are presented in Figure 3.23. The corresponding integrated intensity profiles are presented in Figure 3.24. The integrated intensity profiles showed the three strong peaks located on the equator indexed (110), (040), and (130) reflections, suggesting the presence of α-form crystal, as discussed in the Introduction section (Chapter 1). The diffraction rings started disappearing as the platform was moved closer to the spinneret. In Figure 3.23, the WAXD pattern at 30 cm from the spinneret shows no diffraction rings and the corresponding integrated intensity plot shows a halo profile, suggesting the presence of amorphous phase only. At distances further down the spinneret, the diffraction rings are seen forming, and the corresponding integrated

intensity profiles show an increase in the intensities of (110), (040), (130), and (111/041) peaks, suggesting the presence of crystalline phase. Percent crystallinities were calculated in the same fashion as for off-line samples, using equation 3.2, as discussed previously in this chapter. The on-line WAXD percent crystallinities were plotted against distance from the spinneret, as presented in Figure 3.25. In Figure 3.26, the same results are presented in a different fashion. Figure 3.25 presents the effect of throughput rate on percent crystallinity and Figure 3.26 presents the effect of take-up velocity on percent crystallinity.

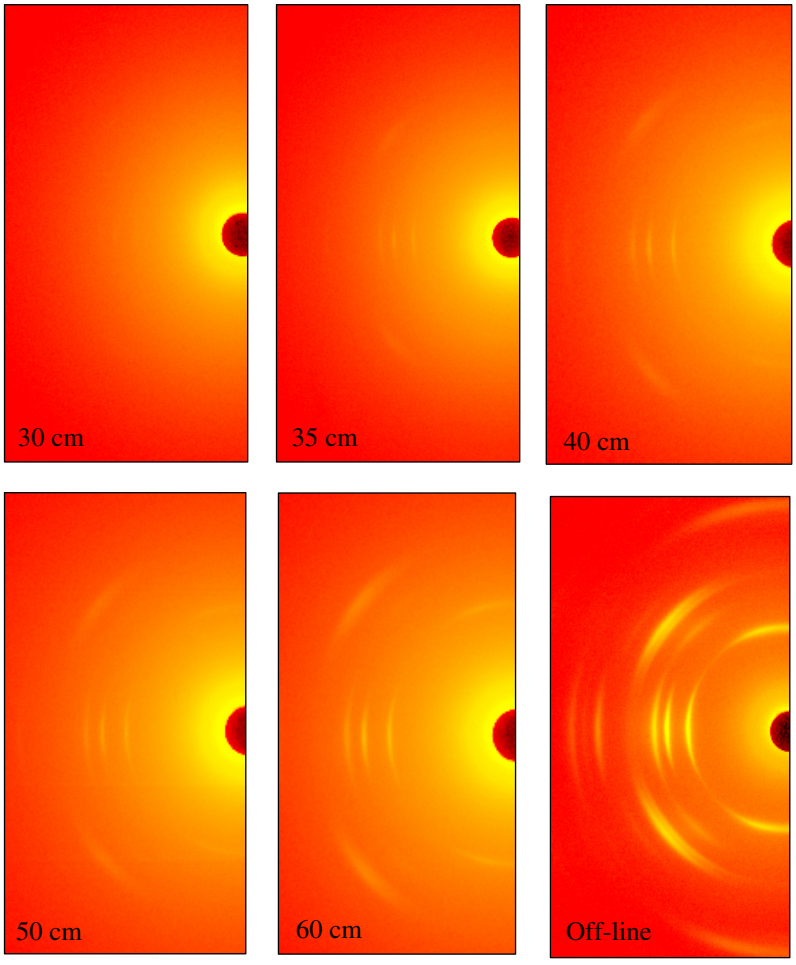

Figure 3.23 WAXD patterns for 400 m/min and 0.89 g/min/hole

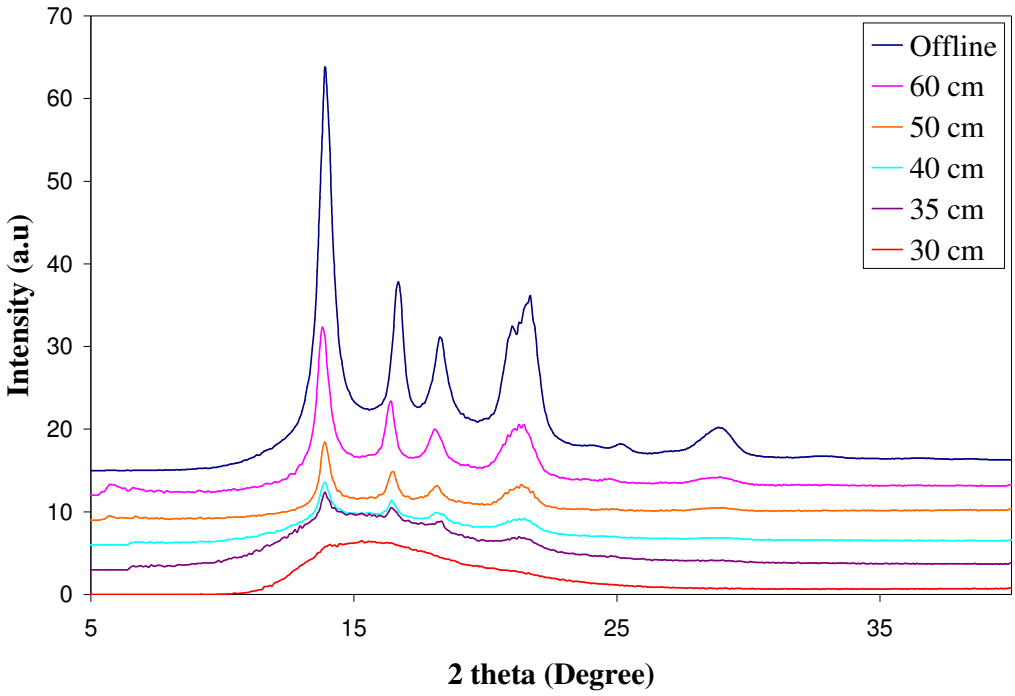

Figure 3.24 Integrated intensity profile plots for 400 m/min and 0.89 g/min/hole

WAXD patterns and the percent crystallinity plots showed an increase in percent crystallinity with increasing distance from the spinneret. At a fixed take-up velocity, a decrease in percent crystallinity was observed with an increase in throughput rate (Figure 3.25). This may be because of two reasons. At higher throughput rate, the cooling rate decreases as a sample volume is larger, and drawdown ratio is lower. At a fixed throughput, an increase in percent crystallinity was observed with an increase in take-up velocity (Figure 3.26). This may be mainly because of the increase in spinline stress with take-up velocity, or due to the increase in cooling rate. The onset of crystallization was observed at 30 cm from the spinneret for 0.67 g/min/hole and 35 cm from the spinneret for 0.89 g/min/hole. This observation is not in agreement with the work of P. E. Lopes [26], as he observed onset of crystallization for 0.89 g/min/hole at positions closer than

30 cm from the spinneret. This may be because of two reasons. The spinneret used in Lopes' work was the non-symmetrical spinneret ('W' spinneret), compared to the symmetrical spinneret ('O' spinneret) used in this work. These differences will be addressed later in this chapter. The on-line WAXD percent crystallinity values for different spinning conditions are presented in Appendix C.

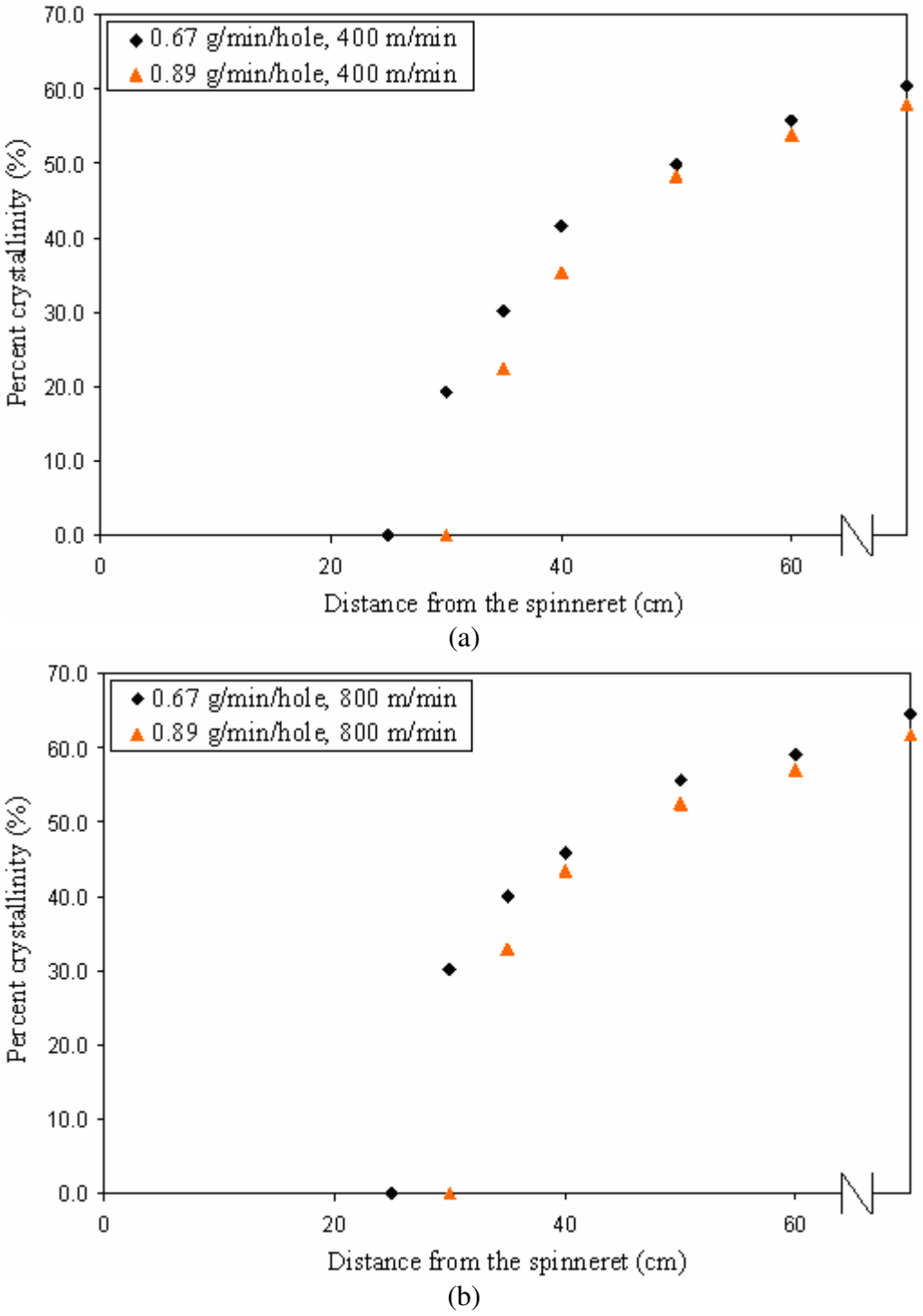

Figure 3.25 Plot of WAXD percent crystallinity and distance from the spinneret for different throughput rates at (a) 400 m/min and (b) 800 m/min

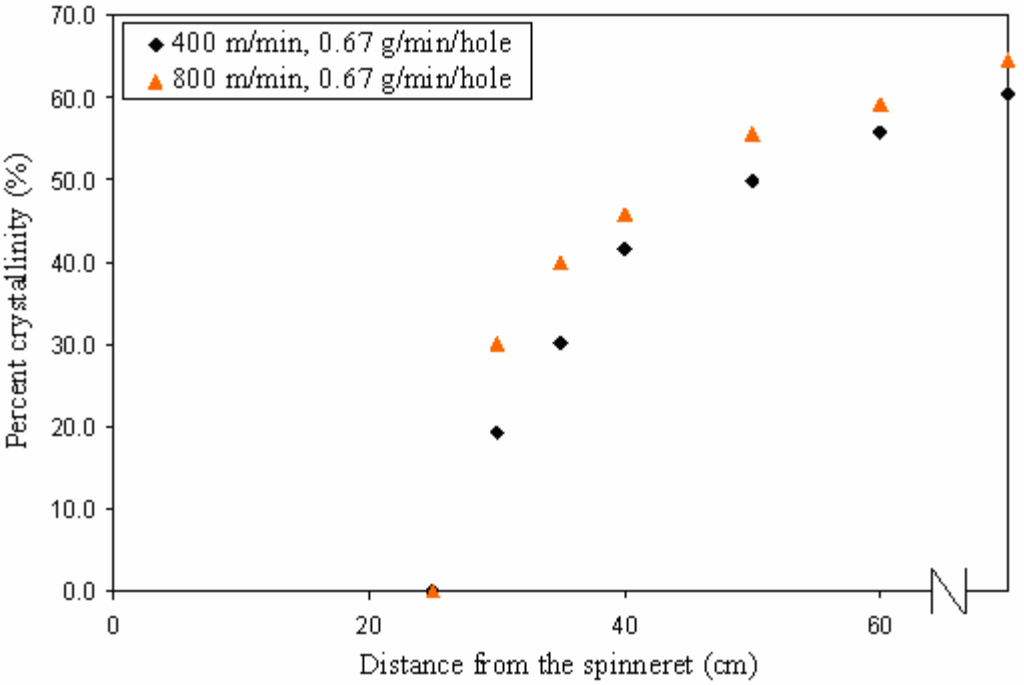

(a)

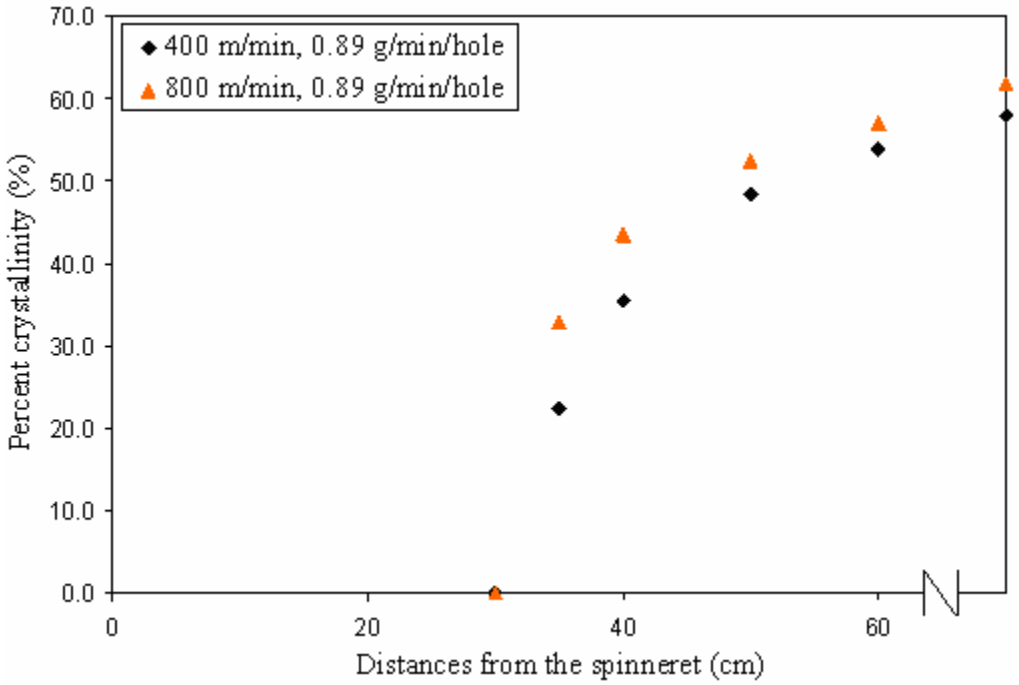

(b)

Figure 3.26 Plot of WAXD percent crystallinity and distance from the spinneret for different take-up velocities at (a) 0.67 g/min/hole and (b) 0.89 g/min/hole

3.3.2 Raman spectroscopy

The on-line Raman spectra collected along the spinline for one of the spinning conditions are presented in Figure 3.27. A change in intensity of peaks at 808 cm^{-1} and 841 cm^{-1} was observed with the change in spinline position, which was in agreement with the work of Nielsen et al. [9]. The peak at 808 cm^{-1}, which was found sensitive to the crystalline content in the iPP fiber, as discussed in Chapter 1, became less intense and eventually was shifted to 801 cm^{-1} in the melt. The peak at 841 cm^{-1}, which was found sensitive to the amorphous content in the iPP fiber, broadened and was shifted to 835cm^{-1} in the melt, as presented in Figure 3.28.

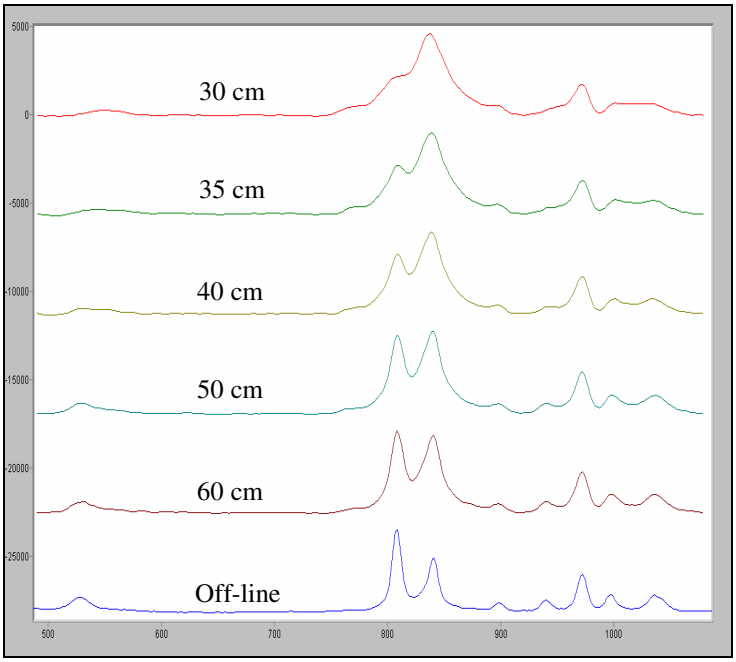

Figure 3.27 Raman spectra at different positions along the spinline for 400 m/min at 0.89 g/min/hole

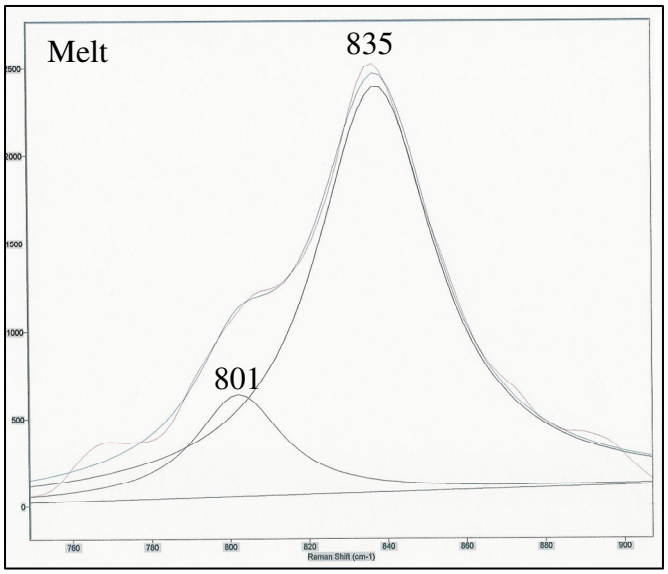

Figure 3.28 Mixed Gaussian-Lorentzian curve fit for iPP melt at 400 m/min and 0.67 g/m/hole

Raman peak ratios were calculated in the same fashion as for off-line samples, using only equation 3.4 (four-peak fit), as the three-peak ratio and four-peak ratio did not show a significant difference for off-line samples. The on-line Raman four-peak ratios were plotted against distance from the spinneret, as presented in Figure 3.29. In Figure 3.30, the same results are presented in a different fashion. Figure 3.29 presents the effect of throughput rate on Raman four-peak ratio and Figure 3.30 presents the effect of take-up velocity on Raman four-peak ratio. At a fixed take-up velocity, a decrease in Raman four-peak ratio was observed with an increase in throughput rate (Figure 3.29). This may be because of two reasons. At higher throughput rate, the cooling rate decreases as a sample volume is more, and drawdown ratio is lower. At a fixed throughput, an increase in Raman four-peak ratio was observed with an increase in take-up velocity (Figure 3.30). This may be mainly because of the increase in spinline stress with take-up velocity. The onset of crystallization was observed at 30 cm from the spinneret for 0.67 g/min/hole

and 35 cm from the spinneret for 0.89 g/min/hole. The on-line Raman four-peak ratios for different spinning conditions are presented in Appendix C.

Both WAXD and Raman spectroscopy showed a similar trend for the increase in percent crystallinity along the spinline. The on-line four-peak Raman ratios were converted to DSC percent crystallinity by multiplying the Raman four-peak ratio with a conversion factor. The conversion factor used for each spinning condition was the ratio of off-line DSC percent crystallinity to the off-line Raman four-peak ratio obtained at that spinning condition. The calculated on-line Raman four peak percent crystallinities were plotted against the on-line WAXD percent crystallinities, and a good correlation was observed based on R^2 value (0.97), as shown in Figure 3.31. The on-line Raman four-peak percent crystallinities for different spinning conditions are presented in Appendix C.

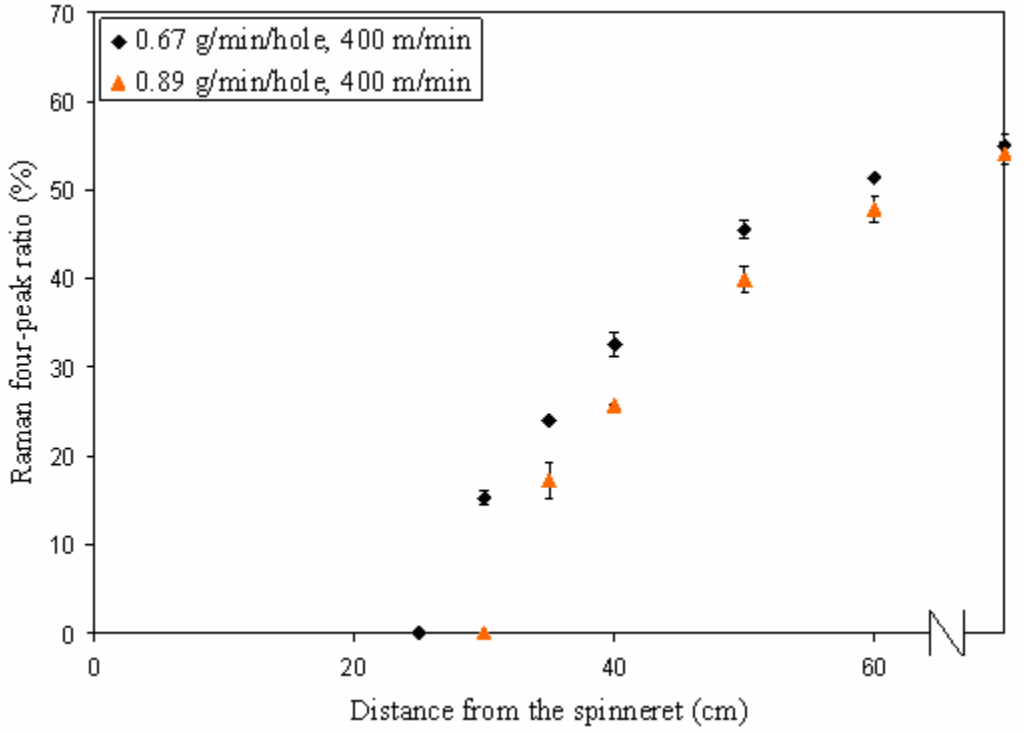

(a)

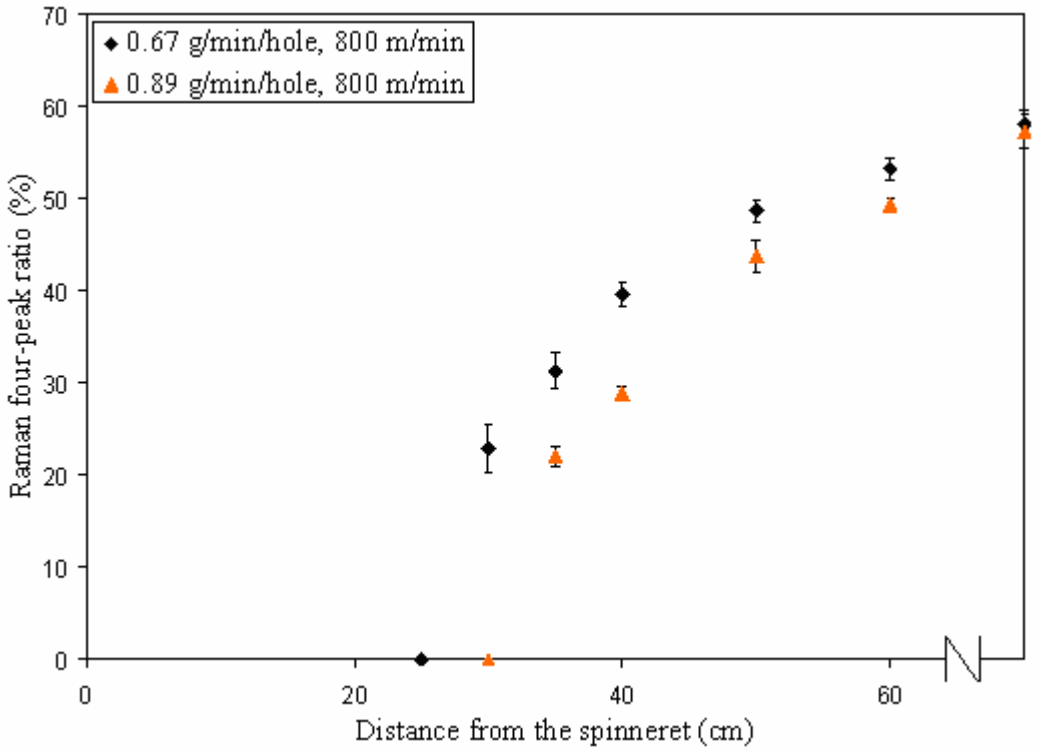

(b)

Figure 3.29 Plot of Raman four-peak ratio and distance from the spinneret for different throughput rates at (a) 400 m/min and (b) 800 m/min

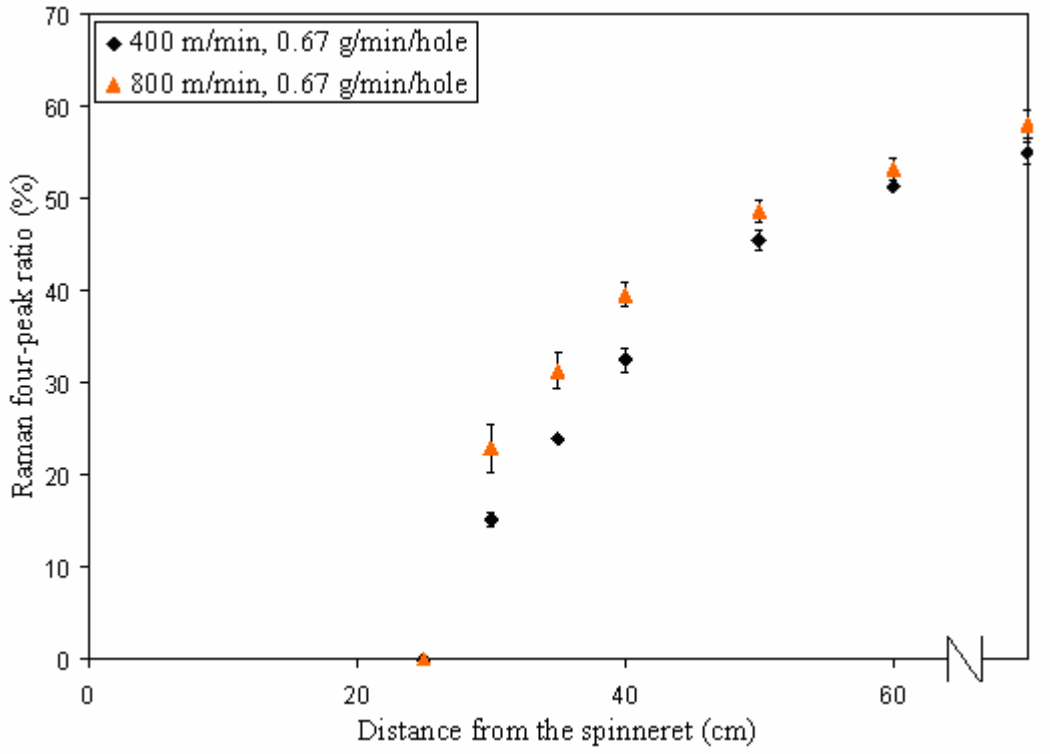

(a)

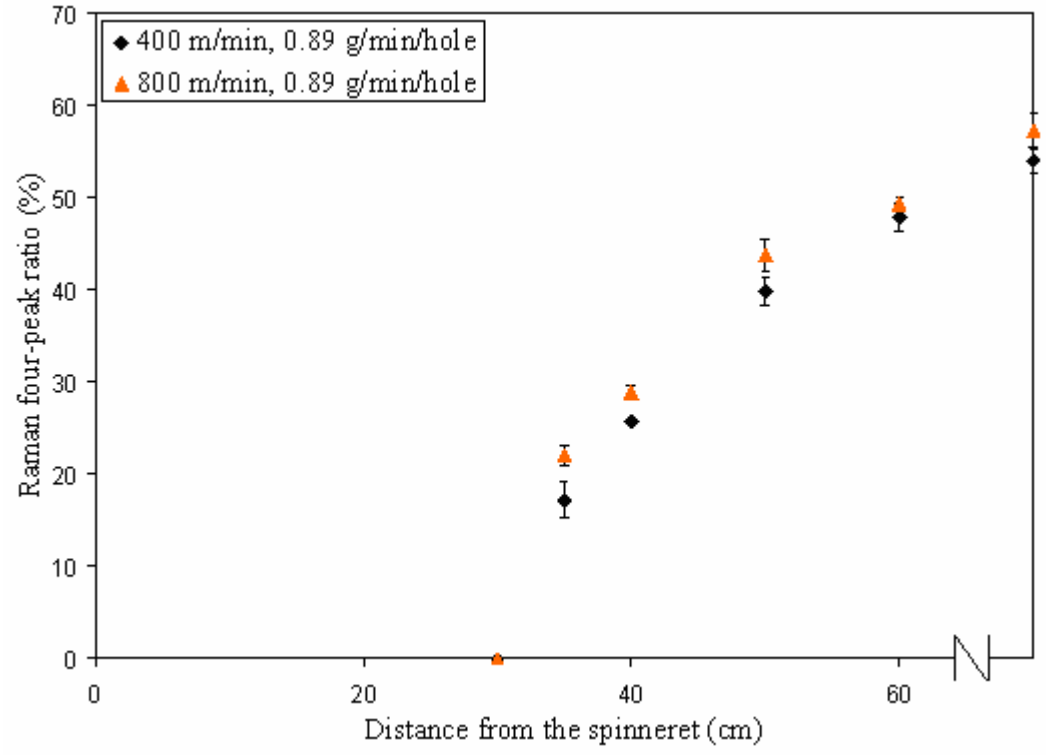

(b)

Figure 3.30 Plot of Raman four-peak ratio and distance from the spinneret for different take-up velocities at (a) 0.67 g/min/hole and (b) 0.89 g/min/hole

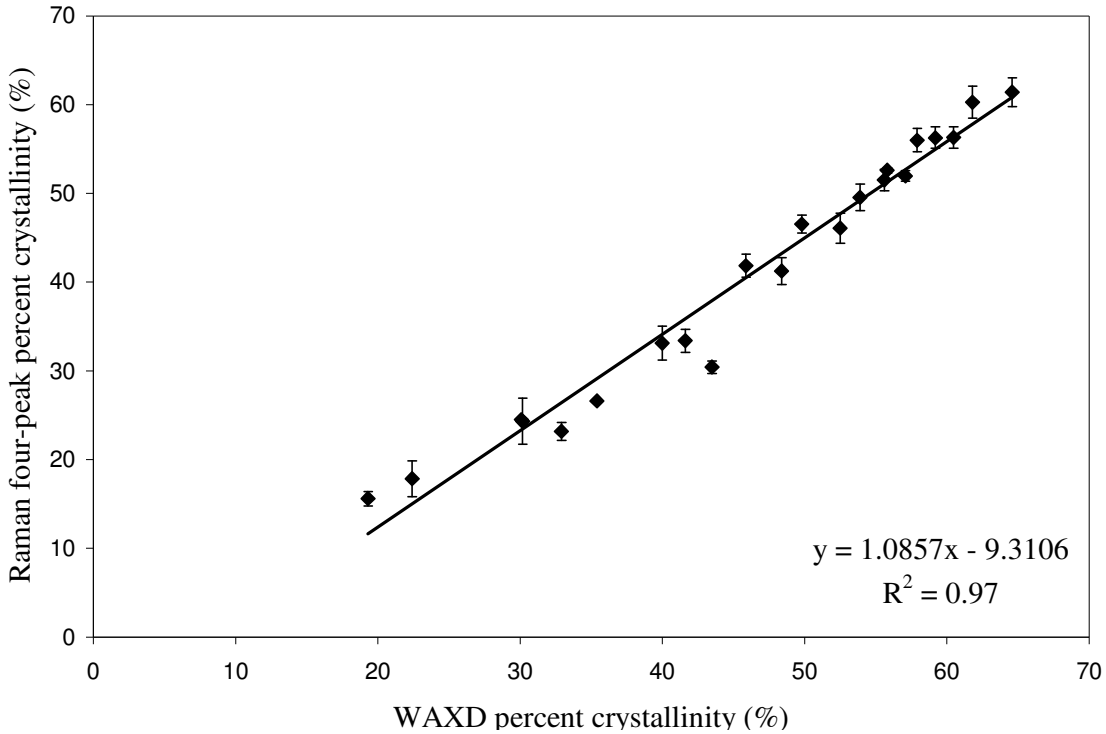

Figure 3.31 Linear correlation between on-line Raman four-peak and WAXD percent crystallinities for all off-line and on-line fiber samples

3.4 Estimation of orientation along the spinline

3.4.1 WAXD

The on-line WAXD images collected along the spinline were previously presented in Figure 3.23. The Hermans orientation factor (f) was calculated in the same fashion as for off-line samples, using equation 3.5 and 3.6, as discussed previously in the chapter. The on-line Hermans orientation factors were plotted against distance from the spinneret, as presented in Figure 3.32. In Figure 3.33, the same results are presented in a different fashion. Figure 3.32 presents the effect of throughput rate on percent crystallinity and Figure 3.33 presents the effect of take-up velocity on percent crystallinity.

At a fixed take-up velocity, a decrease in Hermans orientation factor was observed with an increase in throughput rate (Figure 3.32). This may be because of two reasons. At higher throughput rate, the cooling rate decreases as a sample volume is more, and drawdown ratio is lower. At a fixed throughput, an increase in Hermans orientation factor was observed with an increase in take-up velocity (Figure 3.33). This may be mainly because of the increase in spinline stress with take-up velocity. The onset of orientation was observed at 30 cm from the spinneret for 0.67 g/min/hole and 35 cm from the spinneret for 0.89 g/min/hole. The Hermans orientation factor for a throughput rate of 0.89 g/min/hole and a take-up velocity of 400 m/min was compared with P. E. Lopes' [26] observation and a close agreement was seen, except for the onset of orientation, which was closer than 35 cm from the spinneret in Lopes' work. The on-line WAXD Hermans orientation factor values for different spinning conditions are presented in Appendix C.

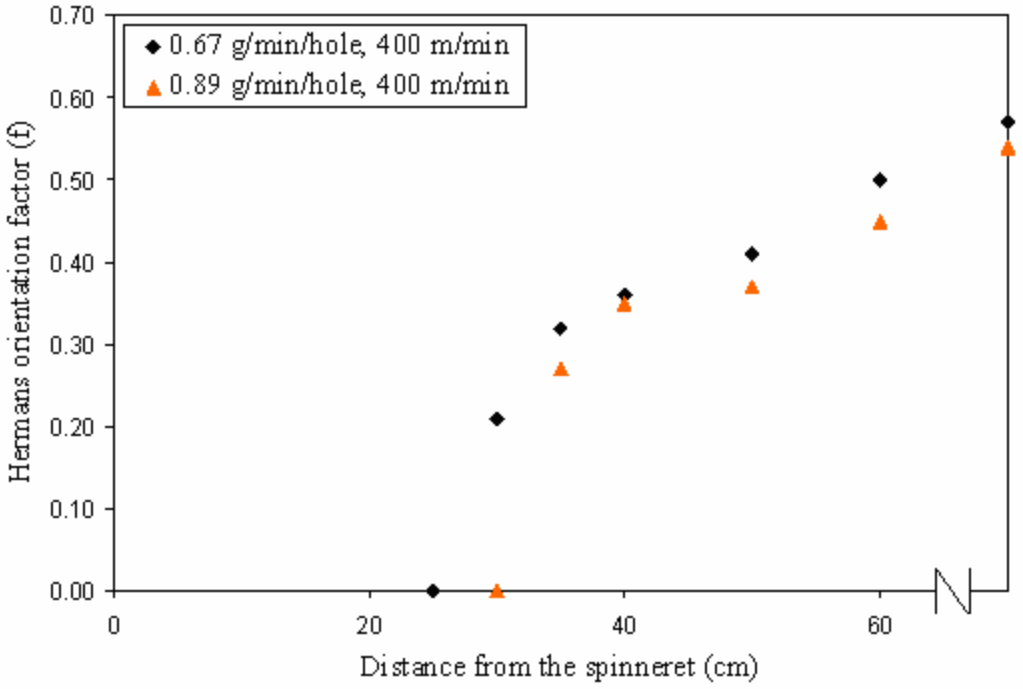

(a)

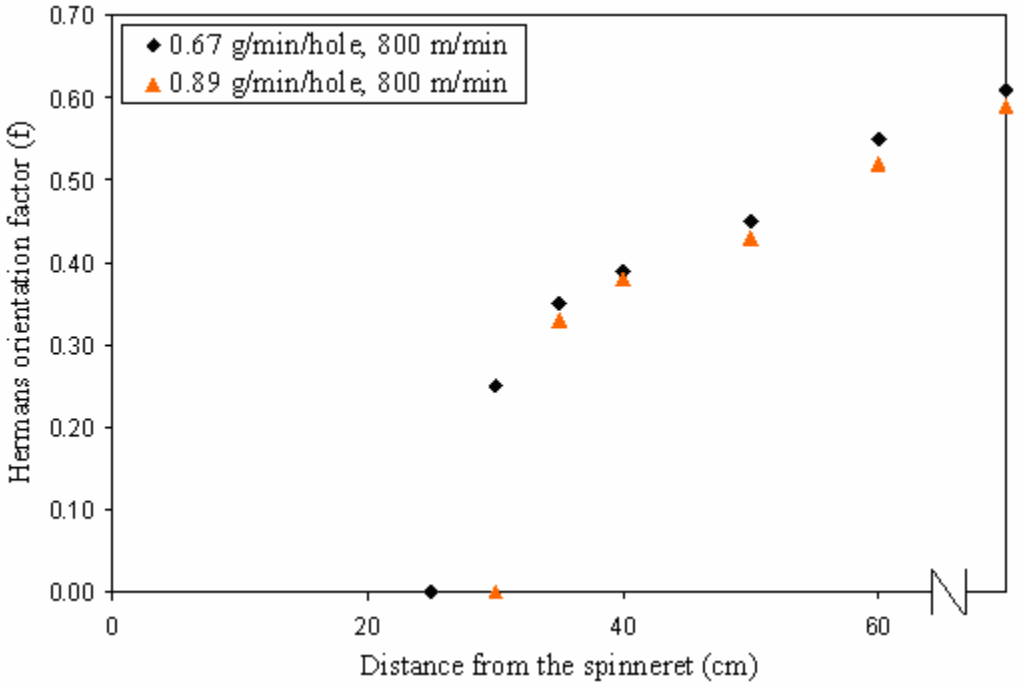

(b)

Figure 3.32 Plot of Hermans orientation factor and distance from the spinneret for different throughput rates at (a) 400 m/min and (b) 800 m/min

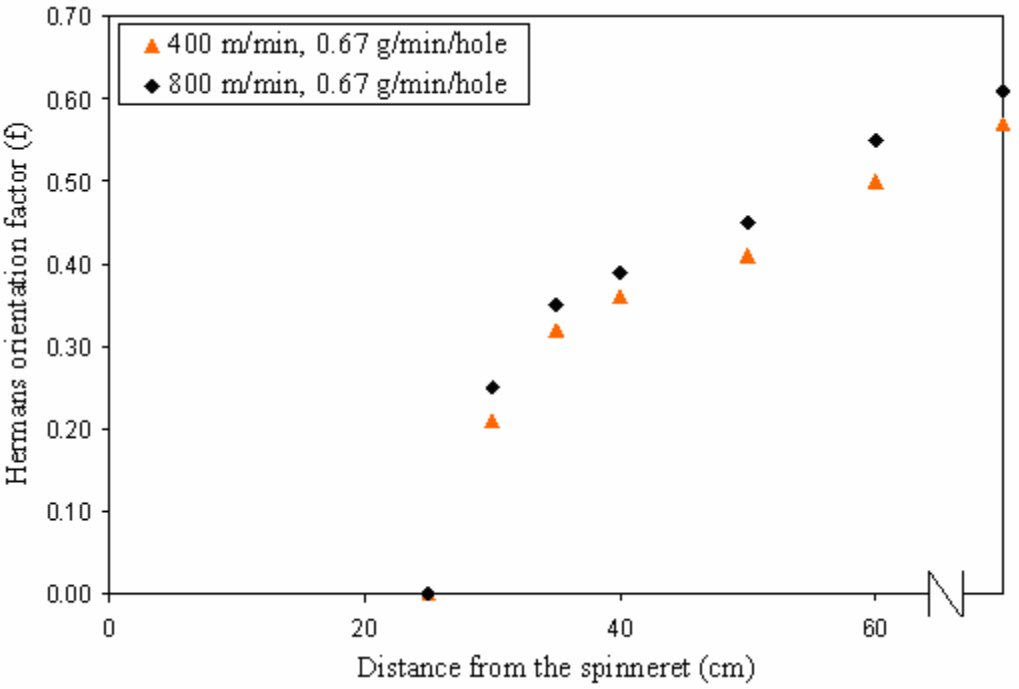

(a)

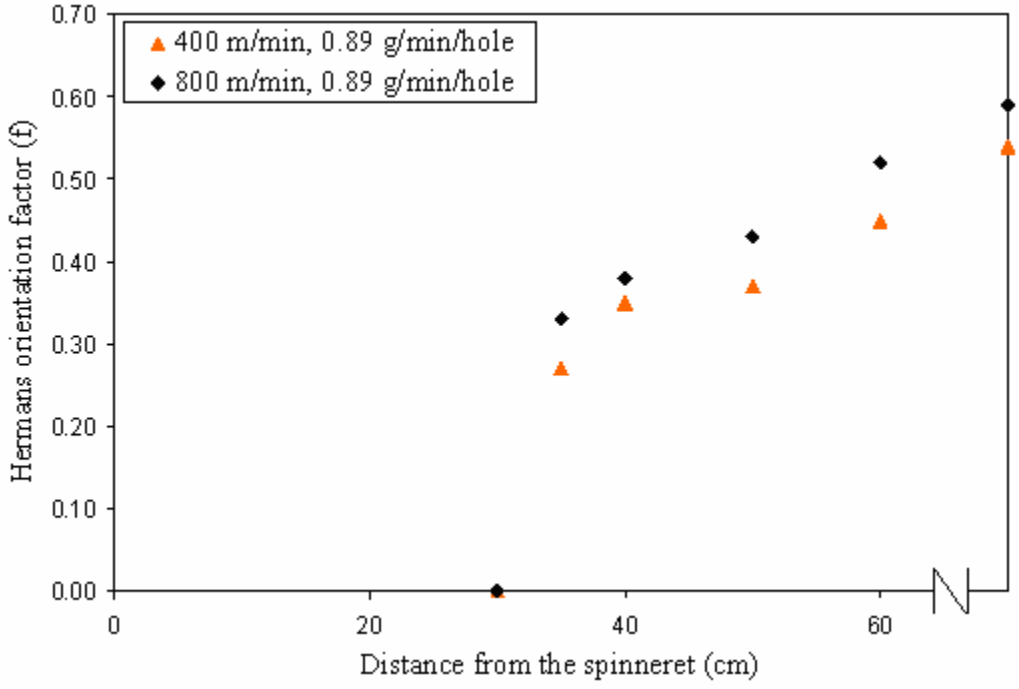

(b)

Figure 3.33 Plot of Hermans orientation factor and distance from the spinneret for different take-up velocities at (a) 0.67 g/min/hole and (b) 0.89 g/min/hole

3.4.2 Polarized Raman spectroscopy

The polarized (XX) Raman spectra for one of the spinning conditions collected at different positions along the spinline is presented Figure 3.34. Variation in intensities of peaks at 808 cm^{-1} and 841 cm^{-1} was observed along the spinline. The polarized Raman peak ratio was calculated in the same fashion as for off-line samples. The on-line polarized Raman peak ratios were plotted against distance from the spinneret, as presented in Figure 3.35. In Figure 3.36, the same results are presented in a different fashion. Figure 3.35 presents the effect of throughput rate on percent crystallinity and Figure 3.36 presents the effect of take-up velocity on percent crystallinity. The on-line polarized Raman peak ratio values for different spinning conditions are presented in Appendix C.

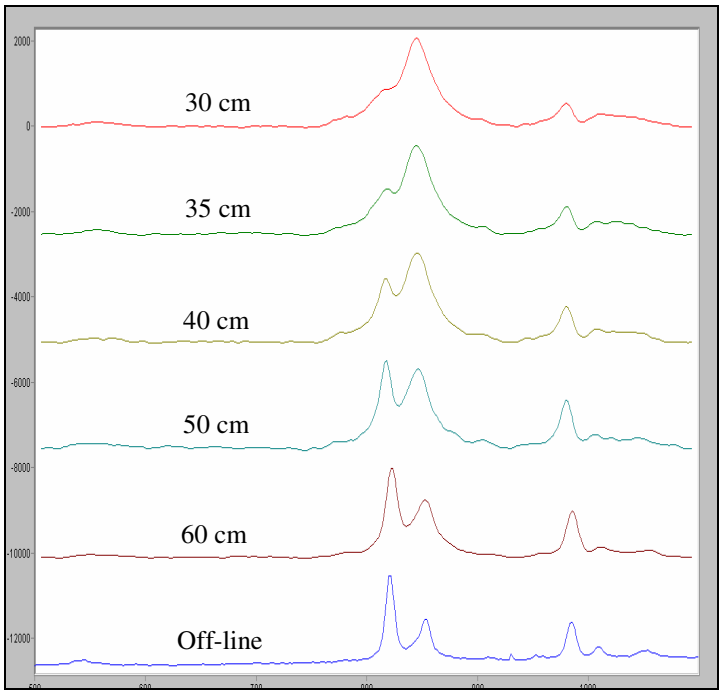

Figure 3.34 Polarized (XX) Raman spectra at different positions along the spinline for 400 m/min at 0.89 g/min/hole

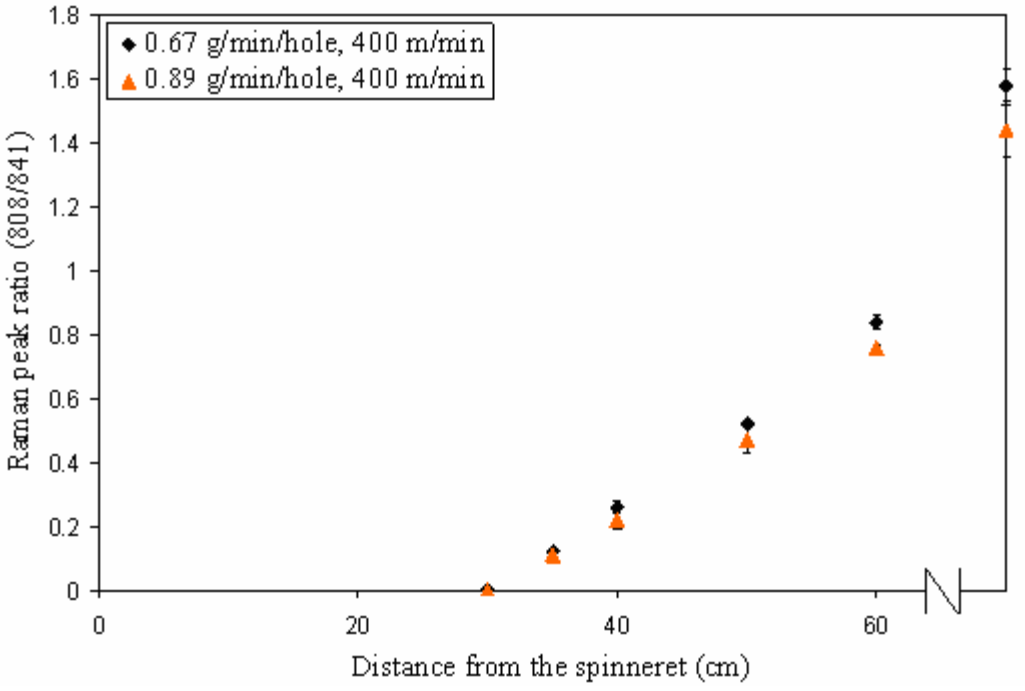

(a)

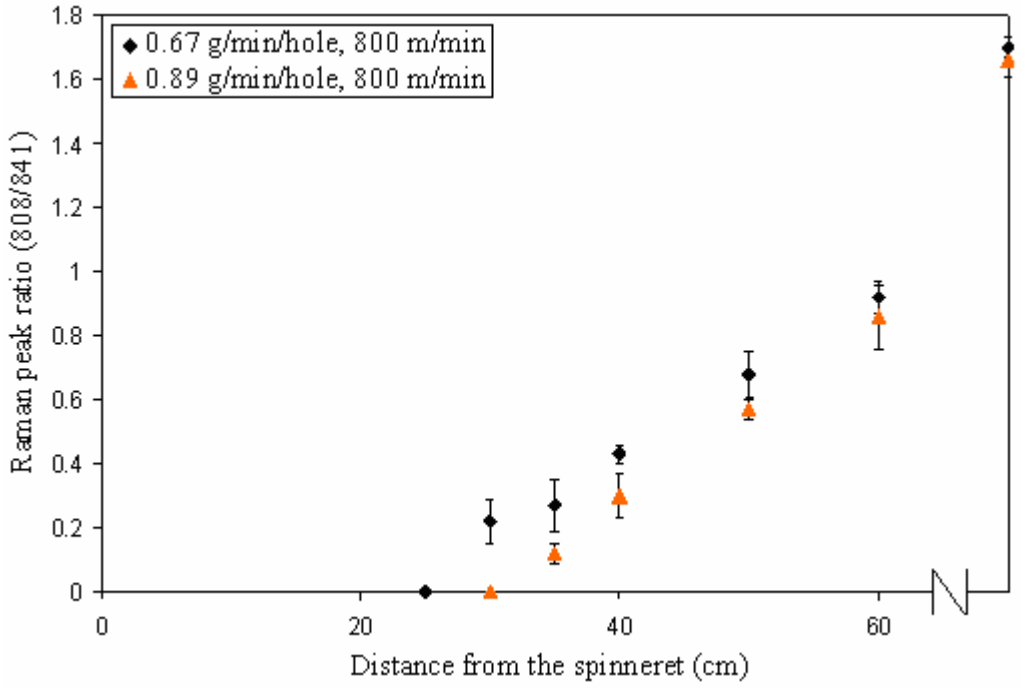

(b)

Figure 3.35 Plot of polarized Raman peak ratio and distance from the spinneret for different throughput rates at (a) 400 m/min and (b) 800 m/min

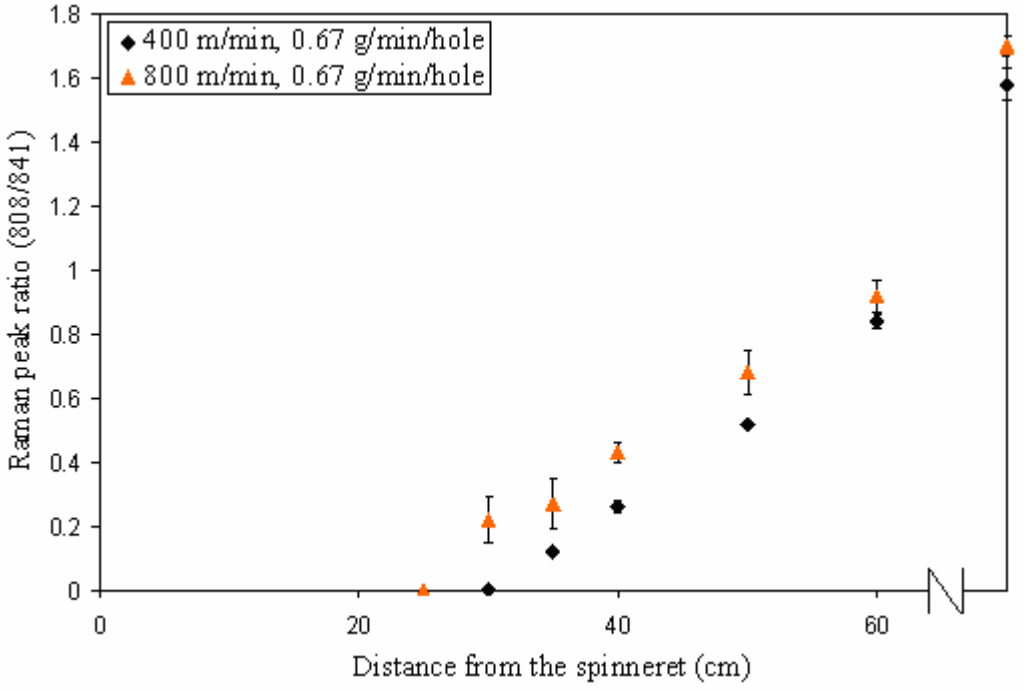

(a)

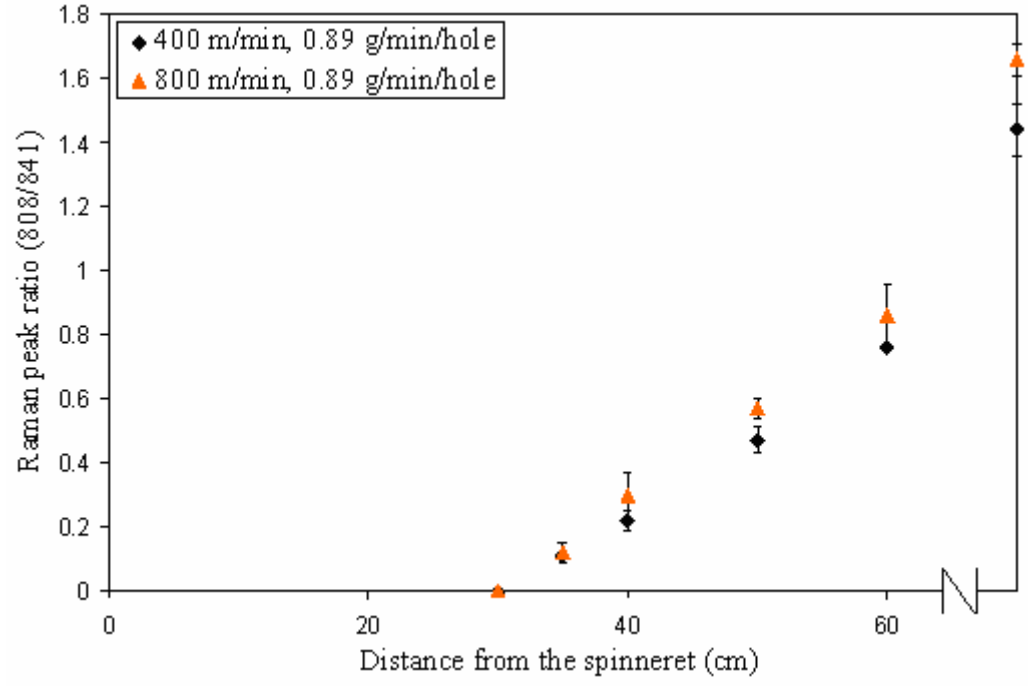

(b)

Figure 3.36 Plot of polarized Raman peak ratio and distance from the spinneret for different take-up velocities at (a) 0.67 g/min/hole and (b) 0.89 g/min/hole

At a fixed take-up velocity, a decrease in polarized Raman peak ratio was observed with an increase in throughput rate (Figure 3.35). This may be because of two reasons. At higher throughput rate, the cooling rate decreases as a sample volume is more, and drawdown ratio is lower. At a fixed throughput, an increase in polarized Raman peak ratio was observed with an increase in take-up velocity (Figure 3.36). This may be mainly because of the increase in spinline stress with take-up velocity. The onset of orientation was observed at 30 cm and 35 cm from the spinneret for 0.67 g/min/hole, and 35 cm from the spinneret for 0.89 g/min/hole.

WAXD and polarized Raman spectroscopy did not show a same trend for the increase in orientation along the spinline. The on-line Hermans orientation factor was observed to increase rapidly at distances closer to the spinneret and then a gradual increase was observed, as shown in Figure 3.32 and 3.33. Polarized Raman spectroscopy showed gradual increase in Raman peak ratio at distances closer to the spinneret and a rapid increase was observed as shown in Figure 3.35 and 3.36. The on-line polarized Raman peak ratios were correlated with the Hermans orientation factor and a good correlation was observed based on R^2 value (0.88), as presented in Figure 3.37. Hermans orientation gives a quantitative measure of orientation in fibers compared to polarized Raman peak ratio, which does not give a quantitative measure of orientation in fibers.

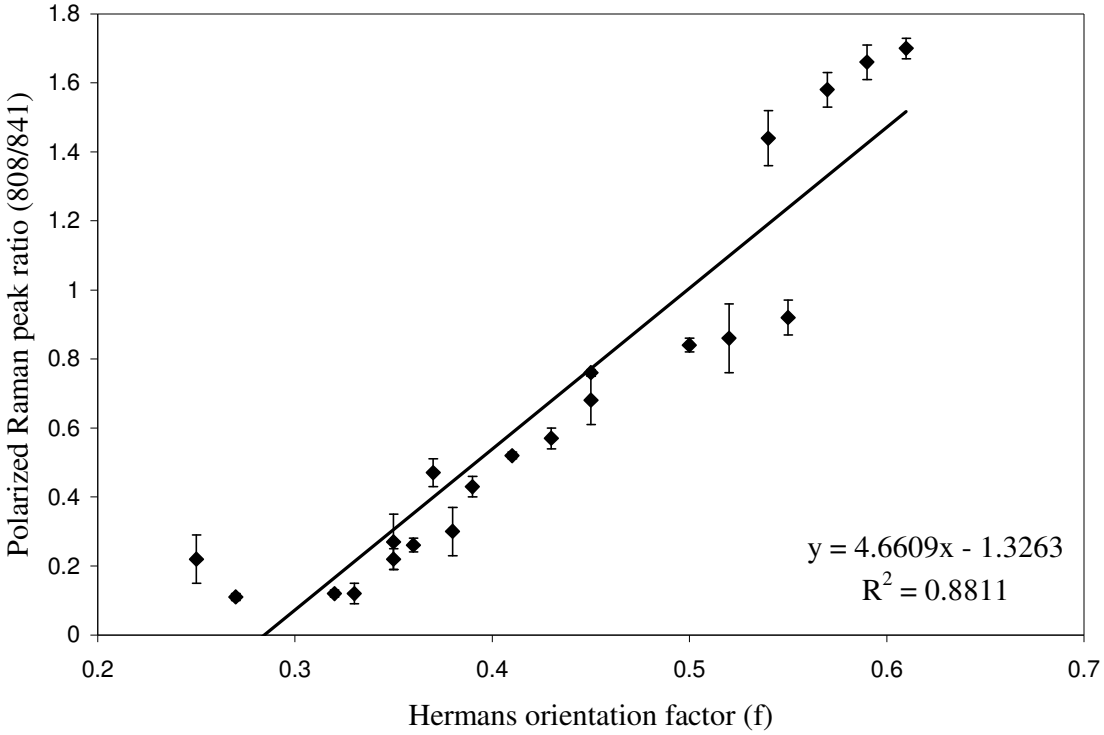

Figure 3.37 Linear correlation between polarized Raman peak ratio and Hermans orientation factors for all off-line and on-line fiber samples

3.5 Preliminary work

3.5.1 Material

The material used in the initial studies was Pro-fax PH 835 (PP35) iPP chips supplied by Basell Inc., Canada. This polymer was melt spun at different drawdown ratios, and both Raman spectra and WAXD patterns were collected. The Raman spectra collected are presented in Figure 3.38. A change in intensity of peaks at 808 cm^{-1} and 841 cm^{-1} was observed with the change in spinline position. The peak at 808 cm^{-1}, which was found sensitive to the crystalline content in the iPP fiber, as discussed in the introduction section (Chapter 1), became less intense and eventually was shifted to 801 cm^{-1} in the

melt. The peak at 841 cm^{-1}, which was found sensitive to the amorphous content in the iPP fiber, broadened and was shifted to 835 cm^{-1} in the melt.

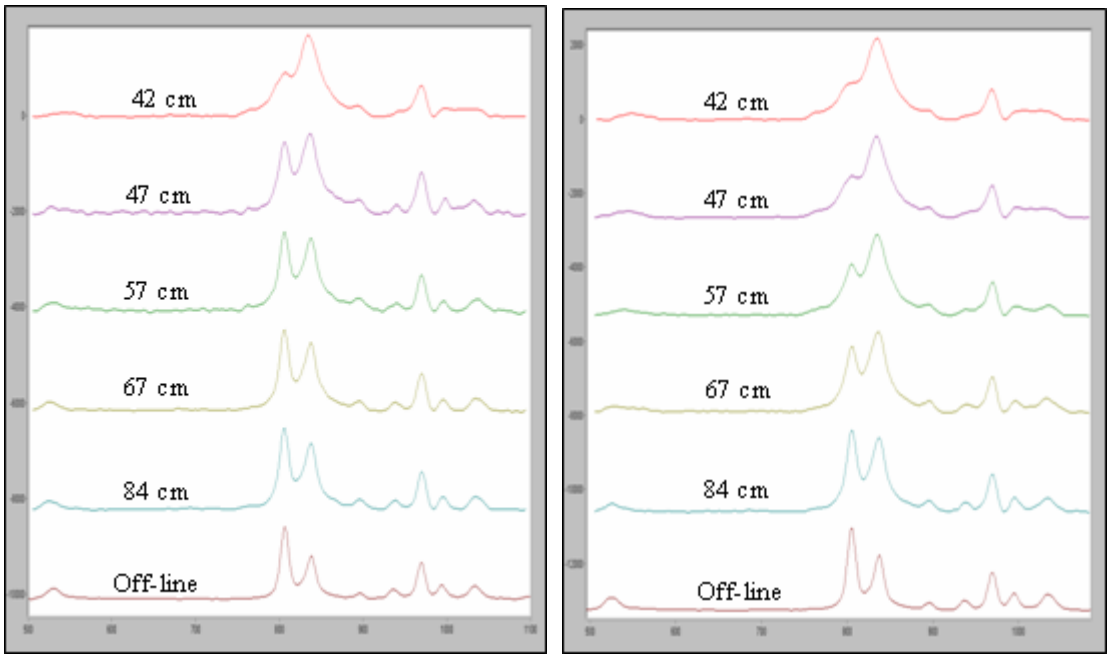

(a) (b)

Figure 3.38 Raman spectra at different positions along the spinline for 1000 m/min at (a) 0.67 g/min/hole, (b) 0.89 g/min/hole

Raman three-peak ratios were calculated in the same fashion as for off-line samples, using equation 3.3. The on-line Raman three-peak ratios were plotted against distance from the spinneret, as presented in Figure 3.39. In Figure 3.40 the same results are presented in a different fashion. Figure 3.39 presents the effect of throughput rate on Raman three-peak ratio and Figure 3.40 presents the effect of take-up velocity on Raman three-peak ratio.

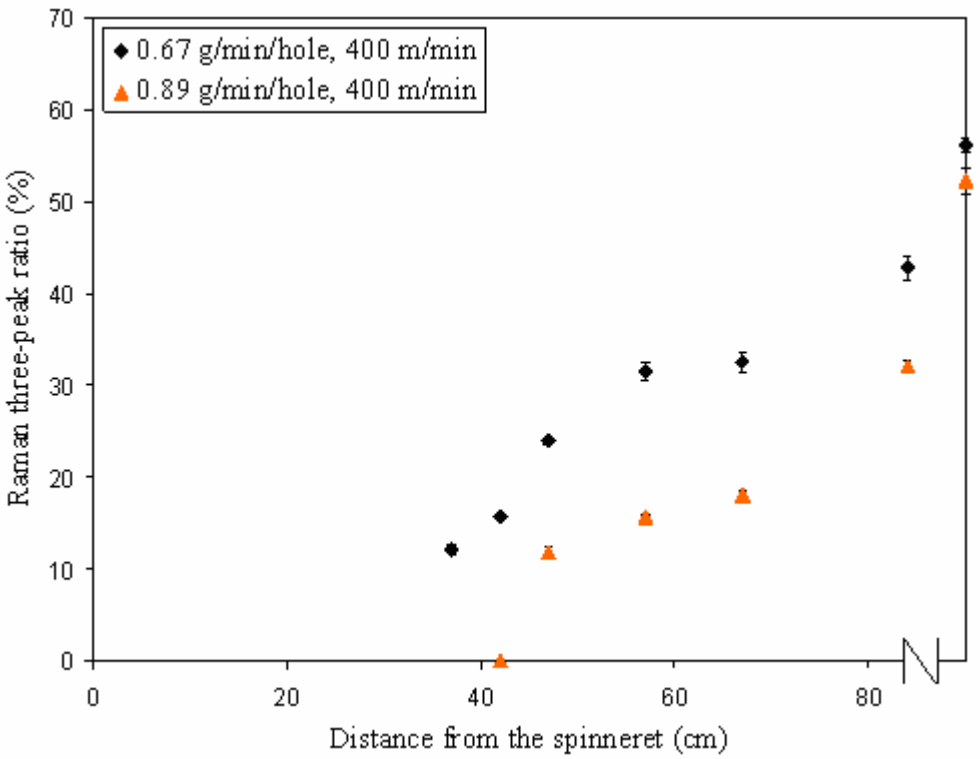

(a)

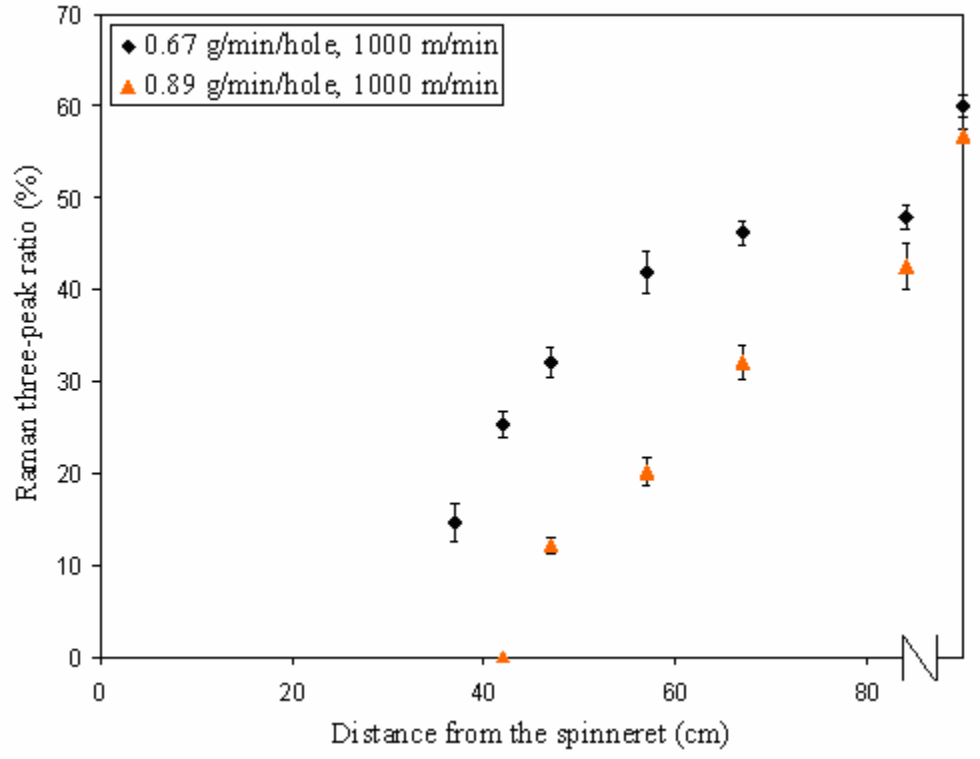

(b)

Figure 3.39 Plot of Raman percent crystallinity and distance from the spinneret for different throughput rates at (a) 400 m/min and (b) 800 m/min

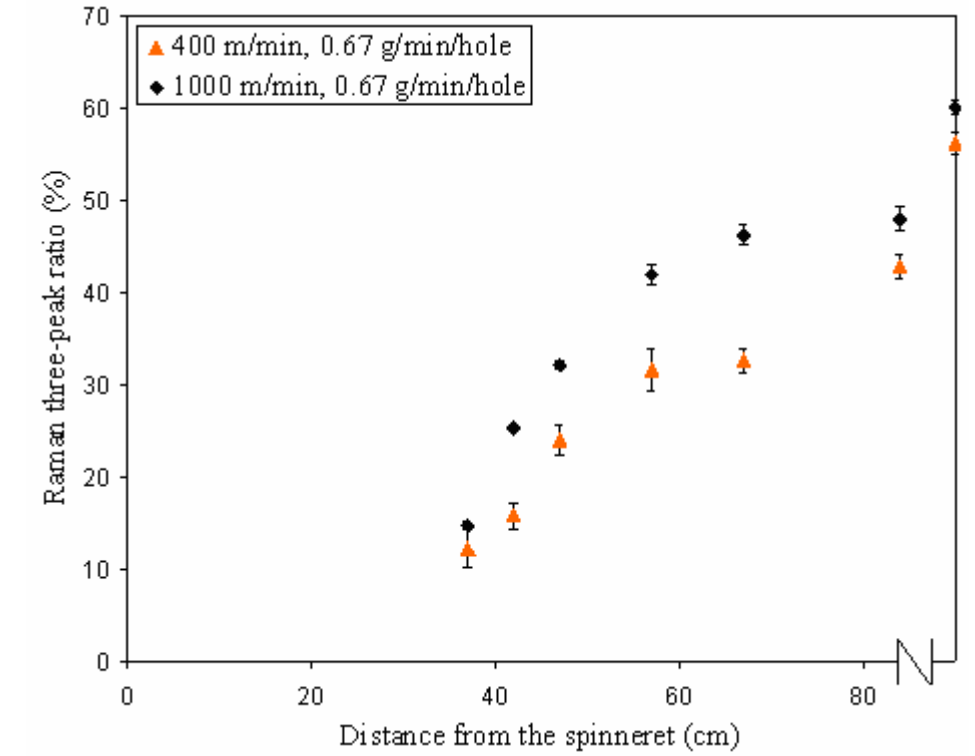

(a)

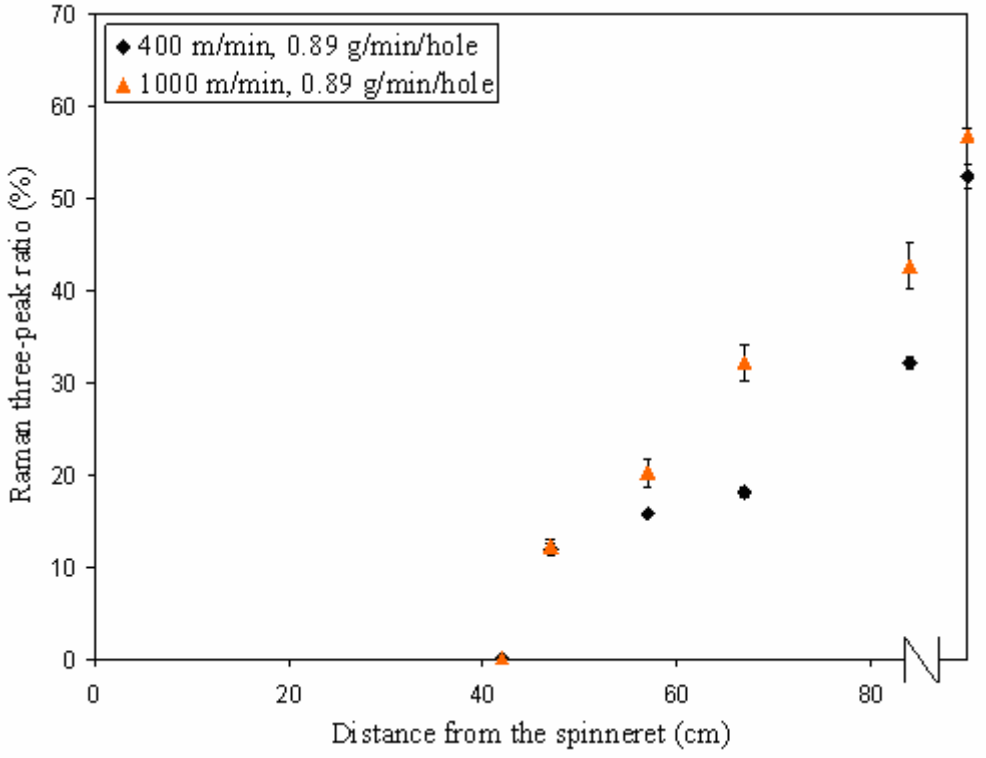

(b)

Figure 3.40 Plot of Raman percent crystallinity and distance from the spinneret for different take-up velocities at (a) 0.67 g/min/hole and (b) 0.89 g/min/hole

At a fixed take-up velocity, a decrease in Raman three-peak ratio was observed with an increase in throughput rate (Figure 3.39). This may be because of two reasons. At higher throughput rate, the cooling rate decreases as the sample volume is more, and drawdown ratio is lower. At a fixed throughput, an increase in Raman three-peak ratio was observed with an increase in take-up velocity (Figure 3.40). This may be mainly because of the increase in spinline stress with take-up velocity. The onset of crystallization was observed at 42 cm from the spinneret for 0.67 g/min/hole and 47 cm from the spinneret for 0.89 g/min/hole.

The on-line WAXD patterns showed very low intensities, even with larger sample volumes. An off-line WAXD pattern collected for a PP35 fiber sample spun at a throughput rate of 0.67 g/min/hole and a take-up velocity of 800 m/min is presented in Figure 3.41 (a). The three strong peaks located on the equator ((110), (040, (130))) were the fingerprints of the α-form iPP crystal. The diffused diffraction rings in the pattern suggested the presence of defective crystals or the paracrystalline mesophase [15]. The corresponding integrated intensity profile, presented in Figure 3.41 (b), also suggested the same. The broadening and overlapping of the peaks corresponding to (110), (040) and (130) could be due the presence of defective crystals or the mesophase.

The polarized (XX) Raman spectra collected for the same sample is presented in Figure 3.42. The bands at 898, 940, and 998 cm^{-1} are very weak. This suggested the presence of mesophase. It is found that during the transition from the α-form crystal to the mesophase, characteristic crystalline bands (898, 940, and 998 cm^{-1}) become much weaker and/or disappear [15]. Ran et al. [15] observed the same transformation in their work. The polymer used by Ran et al. had a melt flow index of 40, which is close to the

melt flow index of PP35. This could be one of the reasons why similar observations were made in both the works.

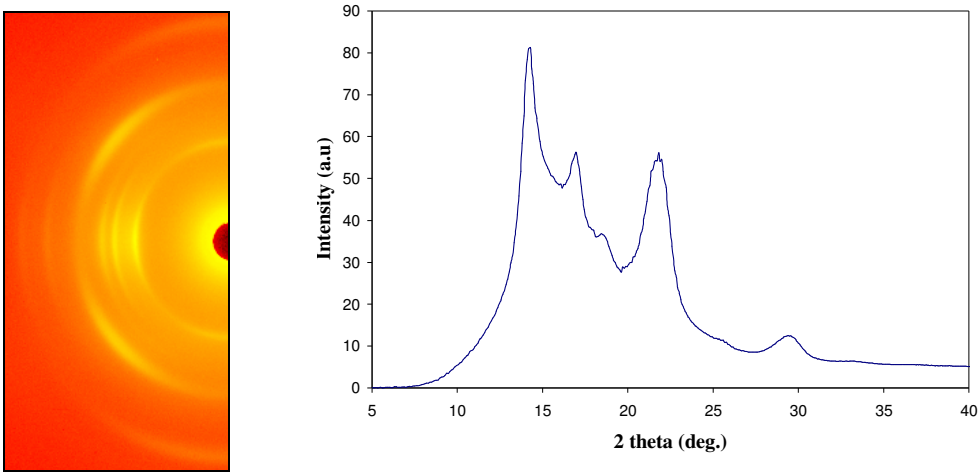

(a) (b)

Figure 3.41 (a) WAXD pattern, and (b) Corresponding integrated intensity profile, for PP35 spun at 0.67 g/min/hole and 800 m/min

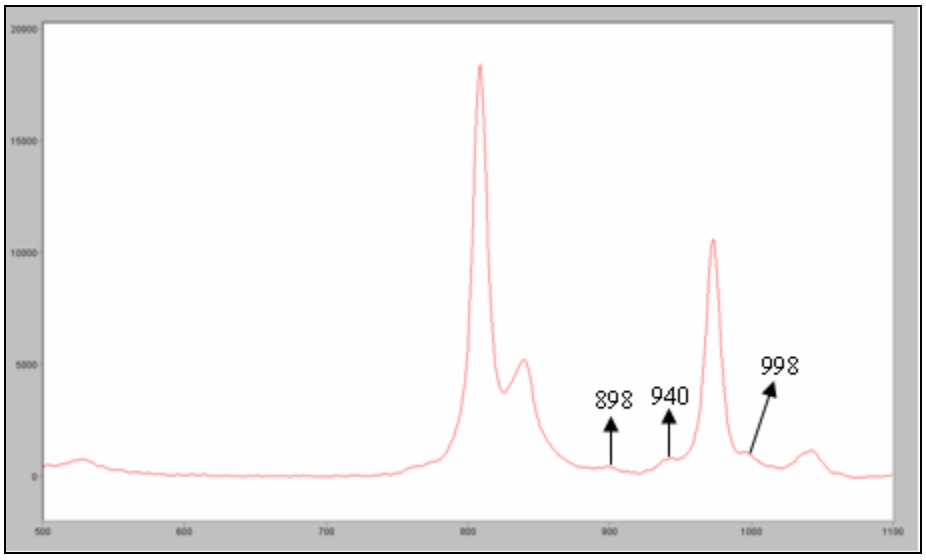

Figure 3.42 Polarized (XX) Raman spectrum for PP35 spun at 0.67 g/min/hole and 800 m/min

On-line experiments run at higher drawdown ratios also failed to show good WAXD patterns. Considering these observations, it was concluded that PP35 was not the suitable material for WAXD studies in this work.

3.5.2 Spinneret

Initial on-line studies were conducted using a six hole spinneret ('W' spinneret) as presented in Figure 3.43. This spinneret was designed to facilitate on-line temperature and diameter measurements on the single filament (hole # 6 in Figure 3.43), and on-line velocity measurements on the bundle of five fibers (hole # 1, 2, 3, 4, and 5 in Figure 3.43). This was the same spinneret was used in previous work conducted at the Center for Advanced Engineering Fibers and Films (CAEFF) [26,46]. S. Varkol [46] collected on-line diameter and temperature measurements on the single filament, and on-line velocity measurements for the bundle of five fibers. P. E. Lopes collected on-line WAXD and SAXS data for the bundle of six fibers. In both these works, the data collected had good reproducibility, i.e. the data collected at each position along the spinline was consistent.

When on-line Raman spectra were collected using the same spinneret, it was observed that at the same distance from the spinneret, depending on where on the spinline the laser was focused, spectra collected were significantly different. Raman spectra collected for a take-up velocity of 400 m/min and 0.45 g/min/hole at 30 cm from the spinneret is presented in Figure 3.44. The intensity of the band at 808 cm^{-1} is higher for spectrum 'a' compared to that of spectrum 'b'. The three-peak ratios were determined using equation 3.3, as discussed earlier in the chapter, for both the spectra, and the percent Raman three-peak ratio obtained for spectrum 'a' was higher than that of

spectrum ‘b’. Initially it was assumed that it was due to the instability in the spinline. Further investigation showed that the fibers exiting from the spinneret holes 1 and 2 presented in Figure 3.43 were pulled more towards the center of the spinneret by the guide. A schematic of the spinline is presented in Figure 3.45. As a result of this, these fibers were under more stress and were rapidly cooled compared to other fibers. The calculated Raman three-peak ratio for these fibers was higher compared to other fibers (as observed by the increase in intensity of 808 cm^{-1} peak in Figure 3.44).

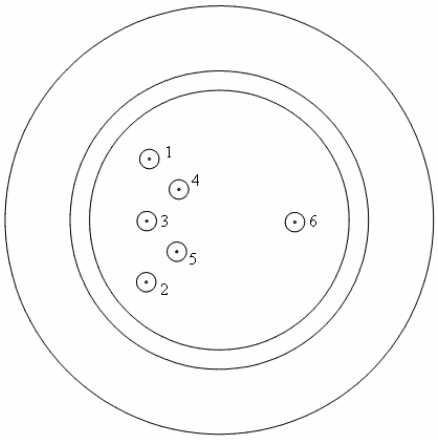

Figure 3.43 Non-symmetrical six hole spinneret (‘W’ Spinneret)

To ensure that the Raman data collected were reproducible, a new spinneret (‘O’ spinneret) was designed, as presented in Figure 3.46. The holes in this spinneret were positioned at equal distances from the center of the spinneret, so that no unnecessary stress was applied on the fibers while positioning the spinline, unlike the spinneret used previously. The Raman spectra collected using the new spinneret had good reproducibility, i.e. the spectra collected at each position along the spinline were consistent.

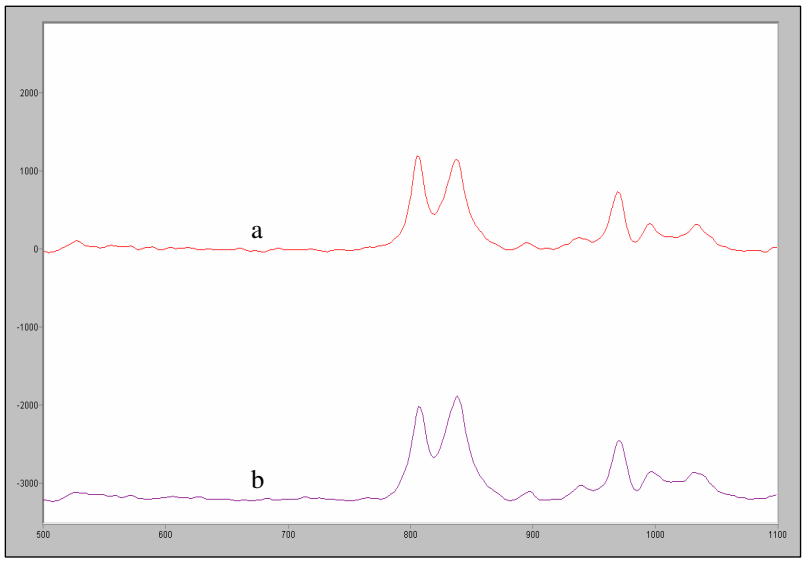

Figure 3.44 Raman spectra collected at 30 cm from the spinneret

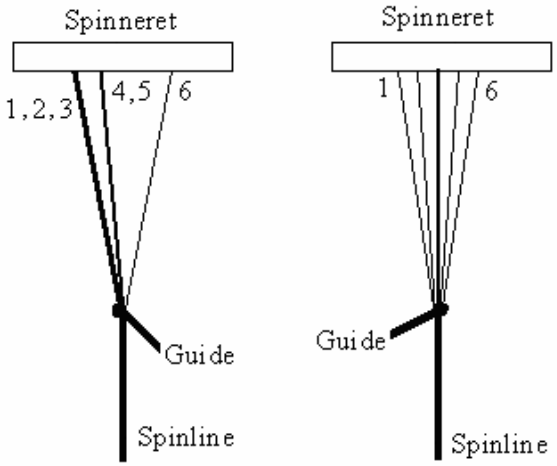

(a) (b)

Figure 3.45 Schematic of spinline for 'W' spinneret (a) Front view (b) Side view

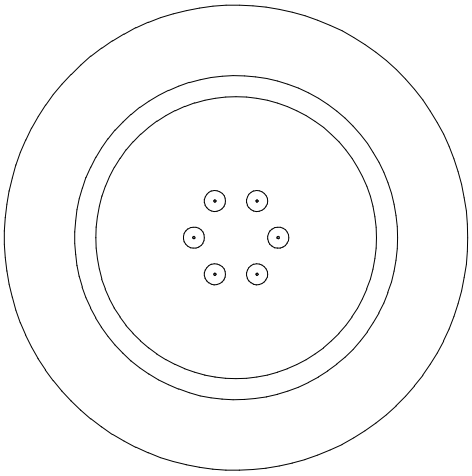

Figure 3.46 Symmetrical six hole spinneret (‘O’ spinneret)

CHAPTER 4

CONCLUSIONS AND RECOMMENDATIONS

4.1 Conclusions

Isotactic polypropylene (Pro-fax PDC 1267) was successfully melt spun at different processing conditions. The processing variables of interest in this research were throughput rate and take-up velocity. Two throughput rates (0.67 and 0.89 g/min/hole) and two take-up velocities (400 and 800 m/min) were used, which provided four different drawdown ratios (264, 353, 529, and 705). All other processing variables were kept constant. Structure development (crystallinity and molecular orientation) in iPP fibers during melt spinning was studied using Raman spectroscopy, polarized Raman spectroscopy, and wide angle x-ray diffraction (WAXD) simultaneously. The melt spun fibers were collected on a bobbin, and the crystallinity and molecular orientation in as-spun fibers were estimated using differential scanning calorimetry (DSC), Raman spectroscopy (polarized and unpolarized), WAXD, and polarizing microscope (refractive index oils and tilting compensator).

The development of structure along the spinline during the melt spinning of iPP, as the fibers transform from a molten state to a solid state, was successfully studied. To accomplish this study, both Raman spectroscopy and WAXD were employed simultaneously for the first time. Both WAXD and Raman spectroscopy suggested the presence of α-form crystal, and showed same trend for the development of crystallinity and orientation.

Two types of curve fits were used for the calculation of Raman peak ratio, a three-peak fit and a four-peak fit. No significant difference was observed between these two fits.

Birefringence was measured using two methods, the refractive index oil and the compensator method. The difference observed between these methods was not significant.

Off-line percent crystallinity measured by both DSC and WAXD, Raman spectroscopy (both three-peak and four-peak ratios), all showed a good correlation with respect to the drawdown ratio. Hermans orientation factor, birefringence, and polarized Raman peak ratios also showed a good correlation with respect to the drawdown ratio. These observations were in agreement with previous work. Take-up velocity had a greater effect on percent crystallinity and orientation than the throughput rate in all cases. Comparison of off-line DSC and WAXD percent crystallinity, and Raman peak ratio showed a good correlation. Comparison of off-line Hermans orientation factor, birefringence, and polarized Raman peak ratio also showed a good correlation. Although each technique used in this research to estimate percent crystallinity and orientation gave a different value, all these techniques showed the same trend and a good correlation was observed.

Raman spectroscopy can be used successfully to study the structure development during melt spinning of polymer fibers. The off-line WAXD patterns observed for PP18 and PP35 were different. PP18 exhibited α-form crystal, whereas PP35 exhibited a combination of both α-form and mesophase. On the other hand, off-line unpolarized spectra for these two polymers did not show any difference. This may be due to the

reason that Raman spectroscopy is usually sensitive to chain conformation and insensitive to the lateral order of the crystalline phase, unlike WAXD.

The WAXD setup used in this study had a few disadvantages. Compared to Raman spectroscopy, the WAXD setup was expensive. WAXD had safety issues due to the x-rays used and a protective shield had to be installed. Raman spectroscopy had very good portability, as it was coupled to a fiber optic probe, unlike WAXD, which was fixed. WAXD had longer collection times (20 minutes for each exposure and 12 minutes for image plate loading and unloading) compared to Raman spectroscopy (2 minutes for each exposure).

4.2 Recommendations

Using polarized Raman spectroscopy, orientation in fibers was estimated by determining the peak ratio in only one geometry (XX). By determining the peak ratios in three geometries, i.e., XX, YY, and XY the second and fourth order co-efficients of the orientation distribution function (P_2 and P_4 respectively) can be estimated. As P_2 and Hermans orientation factor are the same, P_2 obtained from polarized Raman spectroscopy can be compared with the Hermans orientation factor measured by WAXD. Furthermore, on-line birefringence measurements using a compensator, along with Raman spectroscopy and WAXD can also be helpful in providing a clear picture of the development of molecular orientation along the spinline.

The highest drawdown ratio obtained in this work was 705. At a drawdown ratio of 705, the off-line value of Hermans orientation factor was 0.6 and the off-line percent crystallinity obtained by different methods was in the range of 60-65%. Using higher

drawdown ratios may increase the spinline stress, and result in fibers with higher percent crystallinities and orientation. However, it is necessary to make sure that sufficient sample volume is available to obtain good Raman spectra or WAXD patterns. Structure development studies during post drawing of fibers and using different polymers can also be an extension to the studies reported here.

The on-line data collection setup can be improved to facilitate data collection. For example, increasing the range of vertical displacement. The platform on the present on-line setup could move approximately 70 cm away from the spinneret, leaving 110 cm of spinline inaccessible. By increasing the range of vertical displacement information can be obtained on the structure development near the feed roll. Furthermore, during simultaneous data collection, the data collection time is crucial. By reducing the elapsed time between WAXD exposures, as suggested by P. E. Lopes [26], the data collection process can be made faster.

APPENDICES

Appendix A

Throughput rate calculations

PP18 was extruded at different metering pump speeds and the amount of polymer extruded for three minutes was collected. Three trials were run per metering pump speed. The collected polymer was weighed and the mass was recorded. The calculated throughput rates are presented in Table A.1 and a correlation plot between the flow rate and the speed of the metering pump is presented in Figure A.1. A very good correlation was observed based on the R^2 value (0.99).

Table A.1 Throughput rate measurements for different speeds of metering pump

Metering pump speed (rpm)	Throughput rate 1 (g/3min)	Throughput rate 2 (g/3min)	Throughput rate 3 (g/3min)	Average throughput rate (g/3min)	Average throughput rate per hole (g/min/hole)
10	6.7	6.8	6.7	6.73	0.37
18	12.1	12	12.2	12.1	0.67
20	13.5	13.4	13.7	13.53	0.75
24	16	16.1	16.1	16.07	0.89
30	20.3	20.2	20	20.17	1.12

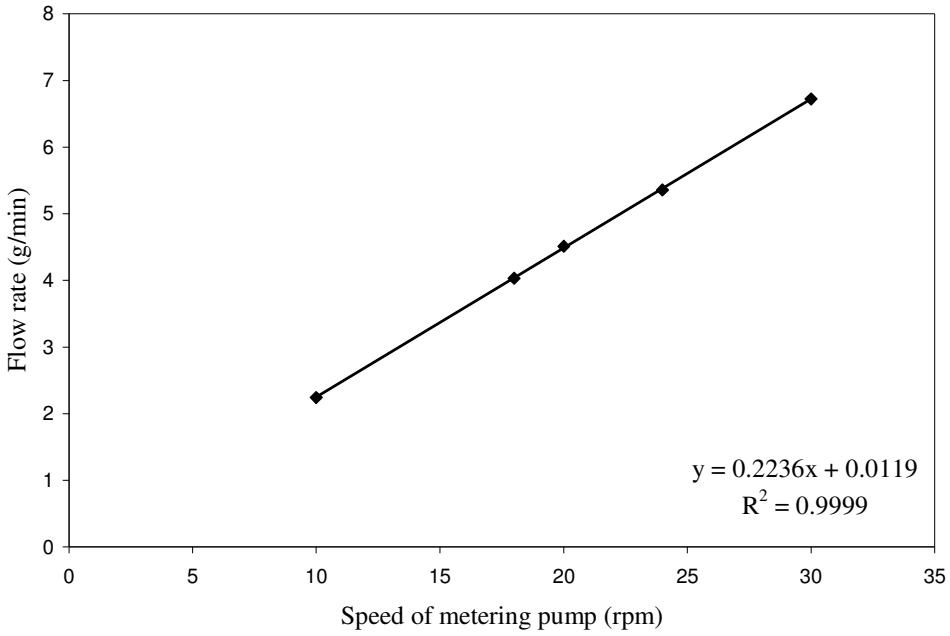

Figure A.1 Linear correlation between flow rate and speed of metering pump

Appendix B

Sample statistical analysis

a) Hypothesis testing for comparing off-line DSC percent crystallinities for drawdown ratios of 353 (μ_{353}) and 705 (μ_{705}), at a level of significance (α) of 0.1.

Hypothesis

H_0 (null): $\mu_{353} = \mu_{705}$

H_a (alternative): $\mu_{705} > \mu_{353}$

$\bar{y}_1 = 61.4$ $\quad s_1 = 0.9$ $\quad n_1 = 3$

$\bar{y}_2 = 56.3$ $\quad s_2 = 0.7$ $\quad n_1 = 3$

Test statistics:

$$t_{obs} = \frac{(\bar{y}_1 - \bar{y}_2)}{\sqrt{\frac{s_1^2}{n_1} + \frac{s_2^2}{n_2}}} = 7.747$$

Rejection region:

$$df = \frac{(n_1 - 1)(n_2 - 1)}{(n_2 - 1)c^2 + (1 - c)^2 (n_1 - 1)} = 3.77$$

where

$$c = \frac{\frac{s_1^2}{n_1}}{\frac{s_1^2}{n_1} + \frac{s_2^2}{n_2}} = 0.623$$

$t_{crit}(90\%) = t_{0.1,3.77} = 1.56$ and $t_{crit}(95\%) = t_{0.05,3.77} = 2.18$

Conclusion:

As $t_{obs} > t_{crit}$ at 95% confidence intervals, reject the null hypothesis (H_0). Therefore there is sufficient evidence to say that $\mu_{705} > \mu_{353}$ at 95% confidence interval.

b) Hypothesis testing for comparing the slopes (β) of the regression lines for correlation with drawdown ratio a level of significance (α) of 0.05.

Hypothesis

H_0 (null): $\beta_{DSC} = \beta_{WAXD}$

H_a (alternative): $\beta_{DSC} > \beta_{WAXD}$

$m_1 = 0.01361$ $\quad SE_1^2 = 0.002563$

$m_2 = 0.01392$ $\quad SE_2^2 = 0.002165$

Test statistics:

$$t_{obs} = \frac{(m_1 - m_2)}{\sqrt{SE_1^2 + SE_2^2}} = 0.0936$$

Rejection region:

$$df = df_{DSC} + df_{WAXD} = 2 + 2 = 4$$

$t_{crit}(95\%) = t_{0.025,4} = 2.78$

Conclusion:

As $t_{obs} < t_{crit}$ at 95% confidence interval, fail to reject the null hypothesis (H_0). Therefore there is sufficient evidence to say that $\beta_{DSC} = \beta_{WAXD}$ at 95% confidence interval.

Appendix C

Online data tables

Table C.1 On-line WAXD percent crystallinity values for different spinning conditions

Distance from the spinneret (cm)	400 m/min, 0.67 g/min/hole	400 m/min, 0.89 g/min/hole	800 m/min, 0.67 g/min/hole	800 m/min, 0.89 g/min/hole
	% C	% C	% C	% C
25	0	0	0	0
20	19.3	0	30.2	0
35	30.1	22.4	40.0	32.9
40	41.6	35.4	45.9	43.5
50	49.8	48.4	55.6	52.5
60	55.8	53.9	59.2	57.1

Table C.2 On-line Raman four-peak ratios for different spinning conditions

Distance from the spinneret (cm)	400 m/min, 0.67 g/min/hole		400 m/min, 0.89 g/min/hole		800 m/min, 0.67 g/min/hole		800 m/min, 0.89 g/min/hole	
	% C	SD	% C	SD	% C	SD	% C	SD
25	0.0	0	0.0	0	0.0	0	0.0	0
30	15.2	0.8	0.0	0	23.0	2.6	0.0	0
35	24.0	0.2	17.2	2.0	31.4	1.9	22.0	1.0
40	32.6	1.3	25.7	0.1	39.6	1.3	28.9	0.7
50	45.5	1.0	39.9	1.5	48.7	1.2	43.8	1.7
60	51.4	0.3	47.9	1.5	53.3	1.2	49.4	0.6

* Standard deviations from five measurements shown in parentheses

Table C.3 On-line Raman four-peak percent crystallinities for different spinning conditions

Distance from the spinneret (cm)	400 m/min, 0.67 g/min/hole		400 m/min, 0.89 g/min/hole		800 m/min, 0.67 g/min/hole		800 m/min, 0.89 g/min/hole	
	% C	SD	% C	SD	% C	SD	% C	SD
25	0	0	0	0	0	0	0	0
30	15.5	0.8	0	0	24.3	2.6	0	0
35	24.5	0.2	17.8	2.0	33.1	1.9	23.2	1.0
40	33.3	1.3	26.6	0.1	41.8	1.3	30.4	0.7
50	46.6	1.0	41.3	1.5	51.5	1.2	46.1	1.7
60	52.5	0.3	49.6	1.5	56.3	1.2	52.0	0.6

* Standard deviations from five measurements shown in parentheses

Table C.4 On-line WAXD Hermans orientation factor values for different spinning conditions

Distance from the spinneret (cm)	400 m/min, 0.67 g/min/hole	400 m/min, 0.89 g/min/hole	800 m/min, 0.67 g/min/hole	800 m/min, 0.89 g/min/hole
	f	f	f	f
25	0	0	0	0
20	0.21	0	0.25	0
35	0.3	0.24	0.38	0.33
40	0.36	0.32	0.46	0.43
50	0.43	0.39	0.51	0.49
60	0.5	0.46	0.55	0.54

Table C.5 On-line polarized Raman peak ratio values for different spinning conditions

Distance from the spinneret (cm)	400 m/min, 0.67 g/min/hole		400 m/min, 0.89 g/min/hole		800 m/min, 0.67 g/min/hole		800 m/min, 0.89 g/min/hole	
	Peak ratio (%)	SD	Peak ratio (%)	SD	Peak ratio (%)	SD	Peak ratio (%)	SD
25	0	0	0	0	0	0	0	0
30	0	0	0	0	0.22	0.07	0	0
35	0.12	0.01	0.11	0.01	0.27	0.08	0.12	0.03
40	0.26	0.02	0.22	0.03	0.43	0.03	0.3	0.07
50	0.52	0.01	0.47	0.04	0.68	0.07	0.57	0.03
60	0.84	0.02	0.76	0.01	0.92	0.05	0.86	0.1

* Standard deviations from five measurements shown in parentheses

REFERENCES

1. R. Lewis and G. M. Edwards, "*Handbook of Raman Spectroscopy"*, Marcel Dekker, Inc., New York, (2001).

2. E. Bolton, *Ind Eng Chem.*, 34, 53 (1942).

3. I. Karacan, "Structure-Property Relationships in Polypropylene Fibers", J. Karger-Kocsis, Ed., *Polypropylene: An A-Z Reference*, Kluwer Publishers, Dordrecht., (1999).

4. N. Pasquini, "*Polypropylene Handbook*", Hanser, Munich, 2nd Edition, (2005).

5. M. Ahmed, "*Polypropylene Fibers – Science and Technology*", Elsevier, Amsterdam, (1982).

6. http://www.hmi.de/bereiche/SE/SE1/projekte/a_methoden/atomar/raman/ (Accessed on Mar 18, 2005).

7. http://www.kosi.com/raman/resources/tutorial/ (Accessed on May 23, 2006).

8. http://www.analchem.ugent.be/Raman/Html/Theory.php/ (Accessed on Mar 18, 2005).

9. A. S. Nielsen, D. N. Batchelder, and R. Pyrz, *Polym.*, 43, 2671 (2002).

10. G. Fraser, P. Hendra, D. Watson, M. Gall, H. Willis, and M. Cudby, *Spectrochimica Acta A*, 51, 2117 (1995).

11. H. Tadokaro, M. Kobayashi, M. Ukita, K. Yasufuku, and S. Murahashi, *J. Chem. Phys.*, 42, 1432 (1965).

12. G. Zerbi and L. Piseri, *J. Chem. Phys.*, 49, 3840 (1968).

13. C. Minogianni, K. G. Gatos, and C. Galiotis*, J. Appl. Spec.*, 59, 1141 (2005).

14. R. P. Paradkar, S. S. Sakhalkar, X. He, and M. S. Ellison, *J. Appl. Spec.*, 55, 534 (2001).

15. S. Ran, D. Fang, I. Sics, S. Toki, B. S. Hsiao, and B. Chu, *Review of Scientific Instruments*, 74, 3087 (2003).

16. S. V. Meille and S. Bruckner, "X-ray Scattering", J. Karger-Kocsis, Ed., *Polypropylene: An A-Z Reference*, Kluwer Publishers, Dordrecht., (1999).

17. L. E. Alexander, "*X-ray Diffraction Methods in Polymer Science*", Robert E. Krieger Publishing Co., New York, (1979).

18. W. H. Carothers and J. W. Hill, *J. Amer. Chem. Soc.*, 54, 1579 (1932).

19. A. Keller and M. J. Machin, *J. Macromol. Sci.-Phys.*, B1 (1), 41 (1967).

20. W. C. Sheehan and T. B. Cole, *J. Appl. Polym. Sci.*, 8, 2339 (1964).

21. K. Katayama, T. Amano, and K. Nakamura, *Kolloid Z. Z. Polym.*, 226, 125 (1968).

22. F. P. Chappel, M. F. Culpin, R. G. Gosden, and T. C. Tranter, *J. Appl. Chem.*, 14, 12 (1964).

23. J.E. Spruiell and J. L. White, Fiber and Yarn Processing, J.L. White, Ed., *Appl. Polym. Symp.*, 27, 121 (1975).

24. H. P. Nadella, H. M. Henson, J. E. Spruiell, and J. L. White, *J. Appl. Polym. Sci.*, 21, 3003 (1977).

25. R. Kolb, S. Seifert, N. Stribeck, and H. G. Zachmann, *Polym. J.*, 41, 1497 (2000).

26. P. E. Lopes, Ph. D. Dissertation, CAEFF, Clemson University, Clemson (2005).

27. A. Ziabicki and K. Kedzierska, *J. Appl. Polym. Sci.*, 2, 14 (1959).

28. A. Ziabicki and K. Kedzierska, *Kolloid Z.*, 171, 52 (1960).

29. A. Ziabicki and K. Kedzierska, *Kolloid Z.*, 175, 14 (1961)

30. A. Ziabicki and K. Kedzierska, *J. Appl. Polym. Sci.*, 6, 111 (1962).

31. A. Ziabicki and K. Kedzierska, *J. Appl. Polym. Sci.*, 6, 361 (1962).

32. M. C. Tobin, *J. Phys. Chem.*, 64, 216 (1960).

33. R. G. Snyder and J. H. Schachtschneider, *Specrochimica Acta, Part A*, 23, 301 (1967).

34. T. Miyazawa, *J. Chem. Phys.*, 38, 2709 (1963).

35. K. Tashiro, M. Kobayashi, and H. Tadokoro, *Polym. J.*, 24, 899 (1992).

36. http://www.basell.com/portal/site/basell/ (Accessed on May 23, 2006).

37. http://www.renishaw.com/client/product/UKEnglish/PGP-37.shtml (Accessed on June 10, 2006)

38. Z. W. Wilchinsky, *J. Appl. Phys.*, 31, 1969 (1960).

39. Y. Koike, M. Cakmak, *Polym. J.*, 44, 4249 (2003).

40. http://www.photonics.com/directory/dictionary/ (Accessed on June 10, 2006).

41. http://omm.hut.fi/opetus/pofy/luento3.pdf./ (Accessed on May 23, 2006).

42. F. P. T. J. van der Burgt, M. S. Thesis, Technische Universiteit Eindhoven, the Netherlands (2002).

43. J. Broda, *J. Appl. Polym. Sci.*, 89, 3364 (2003).

44. E. Andreassen, "Infrared and Raman spectroscopy of polypropylene", J. Karger-Kocsis, Ed., *Polypropylene: An A-Z Reference*, Kluwer Publishers, Dordrecht., (1999).

45. http://www.chem.neu.edu/Courses/U331/CHM1222DSC.ppt#260 (Accessed on November 10, 2006).

46. S. Varkol, M. S. Thesis, CAEFF, Clemson University, Clemson (2005).

47. S. S. Cherukupalli, Ph. D. Dissertation, CAEFF, Clemson University, Clemson (2004).

48. X. Wang, S. Michielsen, *J. Appl. Polym. Sci.*, 82, 1330 (2001).

49. O. Pajgrt, B. Reichstadter, and F. Sevcik, "*Textile Science and Technology 6, Production and Applications of Polypropylene Textiles*", Elsevier, Amsterdam, (1983).

50. J. L. Koenig, "*Spectroscopy of Polymers*", Elsevier, Amsterdam, (1999).

51. http://www.olympusmicro.com/primer/lightandcolor/birefringenceintro.html (Accessed on November 29, 2006).

52. L. H. Sperling, "*Introduction to Physical Polymer Science*", Third Edition, Wiley Interscience (2001).

53. S. Ran, X. Zong, D. Fang, B. S. Hsiao, B. Chu, and R. Ross, *J. Appl. Crystallogr.*, 33, 1031 (2000).